UNIVERSITY OF CRETE
SCHOOL OF SCIENCES AND ENGINEERING
MATERIALS SCIENCE AND TECHNOLOGY

Mesoporous Assemblies from Metal and Metal Oxide Nanoparticles for Environmental Applications

Ph.D. Thesis

GEORGIA VELEGRAKI

Supervisor: **Gerasimos S. Armatas**

Heraklion 2018

ΠΑΝΕΠΙΣΤΗΜΙΟ ΚΡΗΤΗΣ
ΣΧΟΛΗ ΘΕΤΙΚΩΝ ΚΑΙ ΤΕΧΝΟΛΟΓΙΚΩΝ ΕΠΙΣΤΗΜΩΝ
ΤΜΗΜΑ ΕΠΙΣΤΗΜΗΣ ΚΑΙ ΤΕΧΝΟΛΟΓΙΑΣ ΥΛΙΚΩΝ

Μεσοπορώδη Συσσωματώματα από Νανοσωματίδια Μετάλλου και Οξειδίου Μετάλλου για Περιβαλλοντικές Εφαρμογές

Διδακτορική Διατριβή

ΓΕΩΡΓΙΑ ΒΕΛΕΓΡΑΚΗ

Επιβλέπων καθηγητής: **Γεράσιμος Αρματάς**

Ηράκλειο 2018

Doctoral Committee

Gerasimos S. Armatas (Supervisor)

Associate Professor, Dept. of Materials Science and Technology, University of Crete

Pantelis N. Trikalitis

Professor, Dept. of Chemistry, University of Crete

Ioannis N. Lykakis

Associate Professor, Dept. of Chemistry, Aristotle University of Thessaloniki

George Kopidakis

Associate Professor, Dept. of Materials Science and Technology, University of Crete

George Kioseoglou

Associate Professor, Dept. of Materials Science and Technology, University of Crete

Maria Vamvakaki

Associate Professor, Dept. of Materials Science and Technology, University of Crete

Constantinos J. Milios

Associate Professor, Dept. of Chemistry, University of Crete

To Aris, for his endless support

ACKNOWLEDGMENTS

I want to thank many people who in one way or another have contributed to this work. Without their help, this thesis simply would never have finished.

I am deeply grateful to my supervisor Prof. Gerasimos Armatas for his continuous encouragement, valuable advice, guidance and above all, trust and patience despite many unsuccessful experiments.

I would also like to thank Prof. Pantelis Trikalitis, Prof. Ioannis Lykakis, Prof. George Kopidakis, Prof. George Kioseoglou, Prof. Maria Vamvakaki and Prof. Constantinos Milios for accepting to be the members of my dissertation committee.

Many thanks to Dr. Ioannis Papadas and Prof. Bin Liu for the electrochemical measurements, Prof. Stella Kennou for X-ray photoelectron spectroscopy (XPS) measurements, Prof. George Kopidakis for theoretical (DFT) calculations, Prof. Emmanouil Manos for anodic stripping voltammetry and Prof. Qichun Zhang for elemental C, H and N analysis.

Furthermore, I would like to thank the department of Materials Science and Technology, University of Crete for providing me with the necessary infrastructure to accomplish the present dissertation.

Moreover, I would like to thank all former and present members of ChemMater Lab that contributed for a pleasant environment throughout these years. In particular, M.Sc. Ioannis Vamvasakis for his valuable advice and insight, M.Sc. Evangelia Skliri, M.Sc. Eirini Koutsouroubi, M.Sc. Ioannis Tamiolakis, Stelios Papadogiorgakis, Ioannis Daskalakis and Esmeralda Gotsi. Additionaly, many thanks to Dr. Alexia Agiomyrgianaki and Dr. Alexandra Xylouri.

A sincere thank you to my longtime friends Eirini Stavroulaki (my “koumpara”), Marianthi Kafentzi, Manolina Kontaxaki, Theano Mavrikou, Marianna Panteli, Vasso Kotzampasaki, Katerina Bosioli, Kallia Kalogiannaki, Eva Kalaitzaki, Eirini Karkanaki for their longtime friendship and support.

Finally, I would never made it through without the encouragement of my family. I would especially thank my parents Manolis and Eirini for the greatest of love, caring and encouragement, my sisters Maria and Fotini, who always insisted that I should keep going on and never give up, my brother-in-law Christos and of course my sweet niece Eirini-Elpida, who really fills me hope for the future. Last but not least, I deeply thank my spouse Aris. He has always been there for me, and this thesis is as much his success as it is mine.

The present reasearch work has been co-financed by the Greek Ministry of Education (Greek Secretariat of Research and Technology – GSRT) and the European Union (European Social Fund – ESF) under the ERC grant shemes (ERC-09) and the Special Account for Research Funds of University of Crete (SARF UoC).

FUNDING


SUMMARY

During the last decades, the environment is ever-charged by toxic chemicals which usually are by-product of various industrial activities such as electroplating, leather tanning, paint and pigments, and are disposed uncontrollably to the environment. These by-products not only consist a threat to the environment lifecycle but also could have devastating effects to the human being. One of the prominent pollutants of groundwater is hexavalent chromium (Cr(VI)) that is a non-biodegradable contaminant of groundwater and shallow water wells and it is responsible for human carcinogen and mutagen according to the International Agency for Research on Cancer (IARC); thus, classifying it as a Group 1 carcinogen. Therefore, the effective and sustainable neutralization of Cr(VI)-bearing aqueous solutions is one of the utmost importance in terms of protecting the environment and human health. Apart from detoxification solutions, trace analysis such as part per million (ppm) level detection of toxic molecules, such as organic dyes, that may contaminate water is also of great concern. Detecting pollutants in low concentrations, however, pose a significant challenge. Surface-enhanced Raman scattering, commonly known as SERS, has become a powerful analytical technique that extends the range of Raman applications for detecting trace amounts of analytes through their vibrational signals. Assembling 3D nanoscale structures of plasmonic nanoparticles, such as copper (Cu), holds great promise for achieving enhanced optical and electronic properties. Additionally, graphite decorated Cu (Cu/G) nanoparticle assemblies can exhibit a large number of surface hot spots, while offering the possibility for synergetic effects to be achieved.

This dissertation focuses on synthesis, structural characterization and environmental applications of ordered mesoporous networks of metal and metal-oxide nanoparticles. Specifically, it is studied the synthesis of high-surface-area mesoporous assemblies of CoO nanoparticles (CoO MNAs) and their potential application in the reductive detoxification of aqueous hexavalent chromium solutions, under UV and visible light irradiation. These materials indicate excellent photocatalytic performance, which is presumably a result of the combined effect of accessible pore volume, appropriate band edge positions and specific reactivity of the crystal phase. Moreover, in an effort to further improve the photocatalytic

activity and chemical stability of CoO assemblies, we suggest the synthesis of high-surface-area mesoporous networks consisting of Ni and Cu-implanted cubic CoO ($Co_{1-x}Ni_xO$ and $Co_{1-x}Cu_xO$ MNAs) nanoparticles as promising catalysts for detoxification of Cr(VI) aqueous solutions. Mechanistic studies with X-ray photoelectron, UV–vis/near-IR optical absorption, fluorescence and electrochemical impedance spectroscopy and theoretical (DFT) calculations indicate that the performance enhancement of these catalysts arises from the high charge transfer kinetics and oxidation efficiency of surface-reaching holes. By tuning electronic structure and chemical composition, the $Co_{1-x}Ni_xO$ mesoporous catalyst at 2 wt% Ni content impart outstanding photocatalytic Cr(VI) reduction and water oxidation activity, corresponding to an apparent quantum yield (QY) of 1.5% at λ = 375 nm irradiation light. The remarkable activity and durability of the CoO-based MNAs implies the great possibility of implementing these new catalysts into a realistic Cr(VI) detoxification of contaminated water.

Additional subject of the present research is the fabrication of highly porous Cu nanoparticle assemblies decorated with graphite layers (denoted as Cu/G NPAs), as well as their use in SERS detection. The large surface area of the porous framework of assembled Cu/G NPAs exposes essentially a number of plasmonic sites to incoming molecules, resulting in a significant SERS enhancement for chemical analyte detection. Moreover, the network structure of these materials shows a similar SERS activity across different spot areas with high reproducibility. These findings are very promising and suggest that Cu/G nanoparticle assemblies are highly efficient, cost-effective, and stable substrates for SERS detection.

ΠΕΡΙΛΗΨΗ

Τις τελευταίες δεκαετίες, το περιβάλλον επιβαρύνεται με ποικίλες τοξικές ουσίες οι οποίες απορρέουν ως παραπροϊόντα από διάφορες βιομηχανικές δραστηριότητες, όπως είναι η επιμετάλλωση, η κατεργασία δερμάτων, η βαφή μετάλλων κ.α. Αυτό έχει σαν αποτέλεσμα να απειλείται με καταστροφικές συνέπειες όχι μόνο ο περιβαλλοντικός κύκλος ζωής αλλά και η ανθρώπινη υγεία. Ένας από τους σημαντικότερους ρύπους των υπόγειων υδάτων είναι το εξασθενές χρώμιο (Cr(VI)), το οποίο λόγω του μη βιοδιασπώμενου χαρακτήρα του μπορεί εύκολα να μολύνει τα υπόγεια ύδατα και τα ρηχά πηγάδια. Σύμφωνα με τον Διεθνή Οργανισμό Έρευνας του Καρκίνου (IARC) ταξινομείται ως καρκινογόνο Ομάδας 1 και είναι υπεύθυνο για καρκινογενέσεις και μεταλλάξεις του ανθρώπινου γενετικού κώδικα. Κατά συνέπεια, η αποτελεσματική και βιώσιμη απορρύπανση των υδάτων που περιέχουν Cr(VI) είναι εξαιρετικής σημασίας. Εκτός από τις μεθόδους απορρύπανσης, η ανίχνευση των επιπέδων μόλυνσης των υδάτων από τοξικές οργανικές ενώσεις, όπως οργανικές χρωστικές ουσίες, όταν αυτές βρίσκονται σε πολύ χαμηλές συγκεντρώσεις προκαλεί επίσης μεγάλη ανησυχία. Μια πολλά υποσχόμενη μέθοδος ανίχνευσης είναι η τεχνική της επιφανειακά ενισχυμένης φασματοσκοπίας Raman (Surface Enhanced Raman Spectroscopy, SERS), η οποία βασίζεται στην καταγραφή του χαρακτηριστικού φάσματος Raman μιας ένωσης και έχει δυνατότητα ανίχνευσης οργανικών ενώσεων σε πολύ μικρές συγκεντρώσεις. Οι τρισδιάστατες μεσοπορώδεις νανοδομές από πλασμονικά νανοσωματίδια, όπως ο χαλκός (Cu), αποτελούν πολλά υποσχόμενα υλικά για την επίτευξη βελτιωμένων οπτικών και ηλεκτρονικών ιδιοτήτων. Επιπροσθέτως, σύνθετα υλικά από νανοσωματίδια Cu σταθεροποιημένα σε στρώματα γραφίτη (Cu/G) εμφανίζουν σημαντικό αριθμό επιφανειακών θερμών κηλίδων και έχουν αποτελέσει αντικείμενο έντονης έρευνας σε εφαρμογές γύρω από το πεδίο SERS.

Αντικείμενο της παρούσας διδακτορικής διατριβής είναι η σύνθεση, ο χαρακτηρισμός και οι περιβαλλοντικές εφαρμογές τρισδιάστατων μεσοπορώδων δομών αποτελούμενων από νανοσωματίδα μετάλλου και μετάλλου-οξυγόνου. Ειδικότερα, αποσκοπείται η ανάπτυξη καινοτόμων μεσοπορώδων δομών αποτελούμενων από νανοσωματίδια οξειδίου του κοβαλτίου (CoO MNAs) και η μελέτη της φωτοκαταλυτικής δράσης τους στην απορρύπανση υδατικών

διαλυμάτων Cr(VI), κάτω από ακτινοβολία UV και ορατού φωτός. Τα υλικά αυτά εμφανίζουν εξαιρετική φωτοκαταλυτική δραστικότητα, η οποία φαίνεται να είναι αποτέλεσμα της συνδιαστικής δράσης του μεγάλου όγκου πόρων, της καλά οργανωμένης κρυσταλλικής δομής και της κατάλληλης θέσης των ζωνών σθένους και αγωγιμότητας του υλικού. Επιπλέον, με σκοπό την περαιτέρω βελτίωση της δραστικότητας και χημικής σταθερότητας των CoO MNAs, πραγματοποιήθηκε η ανάπτυξη νέων μεσοπορώδων δομών που αποτελούνται από κυβικά νανοσωματίδια CoO ντοπαρισμένα με ιόντα νικελίου (Ni) και χαλκού (Cu) ($Co_{1-x}Ni_xO$ και $Co_{1-x}Cu_xO$ MNAs). Μηχανιστικές μελέτες με φασματοσκοπία φωτοηλεκτρονίων ακτίνων-Χ, οπτικής απορρόφησης UV–vis/near-IR, φθορισμού και ηλεκτροχημική εμπέδησης σε συνδυασμό με θεωρητικούς υπολογισμούς (DFT) υποδεικνύουν ότι η βελτιωμένη απόδοση των καταλυτών $Co_{1-x}Ni_xO$ και $Co_{1-x}Cu_xO$ MNAs οφείλεται κυρίως στη γρήγορη κινητική μεταφοράς φορτίου και στην υψηλή οξειδωτική ισχύ των φωτοπαραγόμενων οπών. Λόγω της κατάλληλης ηλεκτρονιακής διαμόρφωσης και χημικής σύστασης, ο καταλύτης $Co_{1-x}Ni_xO$ MNAs με 2 wt% Ni επιδεικνύει εξαιρετική δραστικότητα στην ταυτόχρονη αναγωγή του Cr(VI) και οξείδωση του νερού, εμφανίζοντας μια κβαντική απόδοση (QY) περίπου 1.5% σε ακτινοβολία με μήκος κύματος $\lambda = 375$ nm. Η εξαιρετική δραστικότητα και ανθεκτικότητα των μεσοπορώδων δομών με βάση τα νανοσωματίδια CoO, υποδηλώνει την δυνατότητα εφαρμογής του νέου αυτού καταλύτη σε ρεαλιστική απορρύπανση υδάτων που περιέχουν εξασθενές χρώμιο.

Επιπλέον αντικείμενο μελέτης της παρούσας διατριβής αποτελεί η ανάπτυξη υλικών από νανοσωματίδια χαλκού σταθεροποιημένα σε φύλλα γραφίτη (Cu/G NPAs) με μεγάλη εσωτερική επιφάνεια και ομοιόμορφους πόρους. Τα αποτελέσματα δείχνουν ότι τα υλικά Cu/G NPAs παρουσιάζουν ένα μεγάλο αριθμό θερμών κηλίδων στην επιφάνειά τους, δίνοντας τη δυνατότητα να χρησιμοποιηθούν ως αισθητήρες με υψηλή απόδοση στην τεχνική SERS για την ανίχνευση οργανικών ενώσεων. Επιπλέον οι δομές αυτές παρουσιάζουν υψηλή επαναληψιμότητα στην ενίσχυση του σήματος Raman σε διαφορετικές περιοχές του πλέγματος, επιδεικνύοντας έτσι τον αποδοτικό και σταθερό τους χαρακτήρα σε πειράματα ανίχνευσης SERS.

TABLE OF CONTENTS

1

Introduction

1.1 Porous Materials

Porous materials are of vital importance due to their wide use in technological applications such as catalysis, adsorption, ion exchange, energy storage and conversion [1,2,3,4]. Just as their name implies, porous materials contain a plethora of pores, i.e. cavities and channels, which are distributed either uniformly or randomly throughout the solid matrix, forming a continuous network of interconnected vacancies which allow flow of fluids into the structure. The chemical behavior and reactivity of porous solids are mainly affected by morphological features such as specific surface area, specific pore volume and pore size distribution. According to the classification of the International Union of Pure and Applied Chemistry (IUPAC) [5], pores are divided into three categories based on their width, that is, *micropores* of size below 2 nm, *mesopores* of size between 2 and 50 nm, and *macropores* of size above 50 nm (Figure 1).

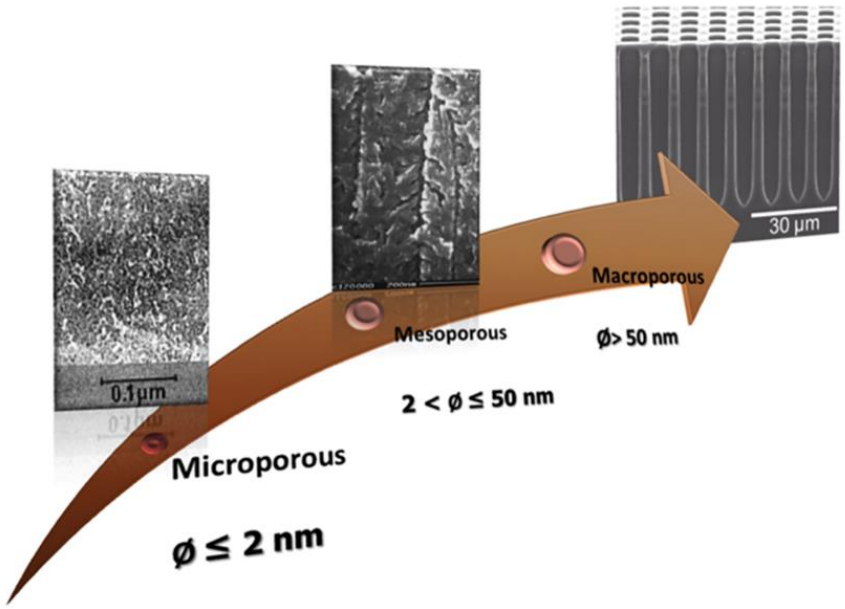

Figure 1. Classification of porous materials according to pore size.

Mesoporous materials are gaining increasing research interest due to their useful properties such as high internal surface area, large pore volume, tunable mesoporous channels with well-defined pore-size distribution, controllable wall composition and modifiable surface characteristics [6]. Additionally, they may exhibit highly ordered and size-controlled porous structure, which is useful for size selective adsorption and separation of small molecules, providing a molecular weight cut-off enrichment. In 1992 researchers of Mobil company first introduced a new family of mesoporous silicate materials named M41S [7], which were dominated by the name MCM (Mobil Composition of Matter). These materials have narrow pore size distribution with a pore diameter ranging from 1.5 to 30 nm, periodically arranged pores (in hexagonal, cubic or leaf-shaped symmetry) and large surface area (> 1000 m^2 g^{-1}). The innovation of Mobil's researchers is based on the use of organic amphiphilic surfactants (soft templates) during the synthesis, which under appropriate conditions (e.g. solvent, reagent concentration, temperature, pH) have the ability to self-organize into micelles acting as templates for the growth of the inorganic structure. This synthetic process has led to the development of many different mesoporous silicate solids, such as MCM-41 which has a two-dimensional (2D) hexagonal pore structure (space group *p*6*mm*), MCM-48 and KIT-6 (Korean Institute of Technology) that possess three-dimensional (3D) cubic organized pore structure (space group *Ia*-*3*d), SBA-type solids (Santa Barbara Amorphous) with 3D organized cubic (SBA-1, space group *Pm*-3*n*) and hexagonal (SBA-15, space group *P*6*mm*) structure, as well as MCM-50 with leaf-shaped pore structure (*La*) (Figure 2).

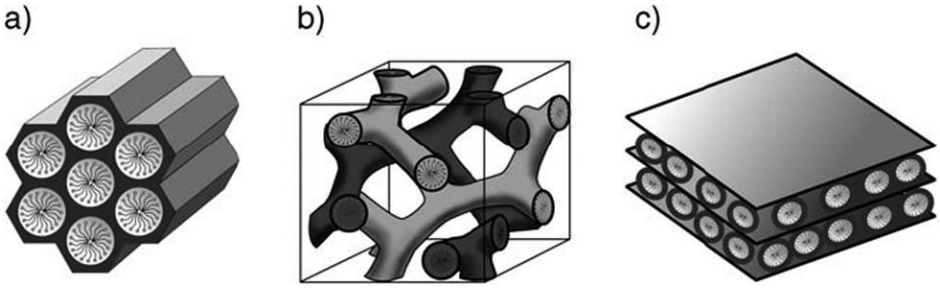

Figure 2. Typical structures of M41S mesoporous materials: (a) hexagonal, (b) cubic and (c) leaf-shaped (lamellar) pore structure.

As it has already been mentioned, Mobil researchers were based on the ability of amphiphilic organic molecules, containing both a hydrophilic and a hydrophobic moiety, to form micelles and as a consequence extensive mesostructures in polar solvents such as water and ethanol. The length of the carbon chain and the size of the hydrophilic part affect significantly the size and geometry of the organic mesostructures. Surfactants typically form cylindrical structures and in a polar solvent are arranged in a way that the hydrophobic part is directed towards the center of the micelle and the hydrophilic part is exposed to the solvent. The synthesis of mesoporous silicate solids initially involves the interaction of the surfactants with hydrolyzed monomer or oligomer metal oxides/hydroxides, which are adsorbed on the outer surface of the forming cylindrical micelles. The inorganic components are condensed usually in the presence of a catalyst, typically acid (e.g. HCl) or base (e.g. NaOH), or get polymerized by the presence of an organic or inorganic compound. The resulting inorganic-organic hybrid mesostructure is bonded by electrostatic interactions between the positively charged surfactant groups and the negatively charged oxo-hydroxyl-metal ($MO_x(OH)_y^{n-}$) species. Then, the solution is placed in an oven, usually at 35 – 150 $^{\circ}$C, for a few hours or days and the resulting solid product is isolated by filtration or centrifugation and dried. Finally, the porous solid obtained after careful removal of the organic molecules between the framework by heating at elevated temperature (usually 500 – 600 °C) in air or nitrogen atmosphere. By calcination, the organic part is finally removed leaving behind a structure of pore channels similar to the micelles mesostructure.

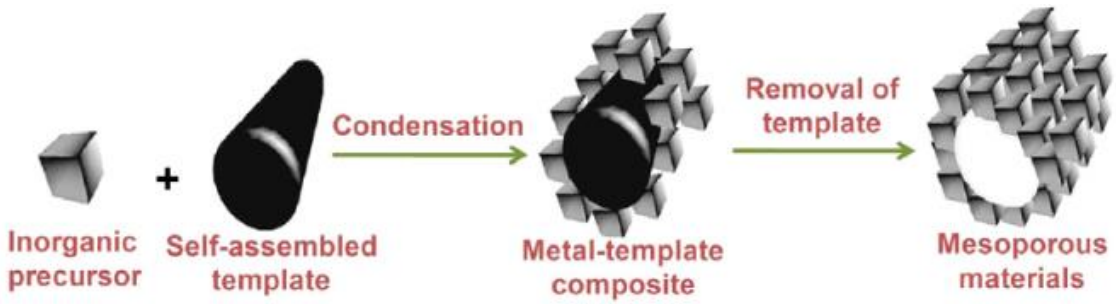

Figure 3. Typical pathway for the formation of mesoporous solids [8].

Many studies have been conducted in order to investigate the formation of the mesostructures based on self-assembly of surfactants. The two most predominant mechanisms that best describe the development of mesoporous materials are the *liquid-crystal templating* and the *cooperative assembly* pathways, proposed by Beck and collaborators immediately after the discovery of MCM-41 [9]. In Figure 4, route (b) is represented the true *liquid-crystal templating* procedure. Due to the fact that hydrophobic tails of templating surfactants are insoluble in polar solvents (e.g. water), while hydrophilic heads would tend to contact with polar solvents, the surfactants can thus self-assembled into micellar liquid crystals at concentrations lower than the "critical micelle concentrations" (CMCs) under certain temperatures. The formed surfactant micelle crystals then act as template for the subsequent formation of inorganic–organic composites around these crystals, afterward the addition and condensation of inorganic precursors from the solution. The route (a) represents *cooperative self-assembly* process. According to that mechanism, the surfactants interact electrostatically with the inorganic species, resulting in simultaneous formation of the micelles. After polymerization and condensation of inorganic components, the ordered mesostructured inorganic–organic composites are eventually formed. Finally, in both (a) and (b) pathways, after removal of templates by solvent extraction or calcination, the mesoporous solids with ordered mesochannels can be obtained.

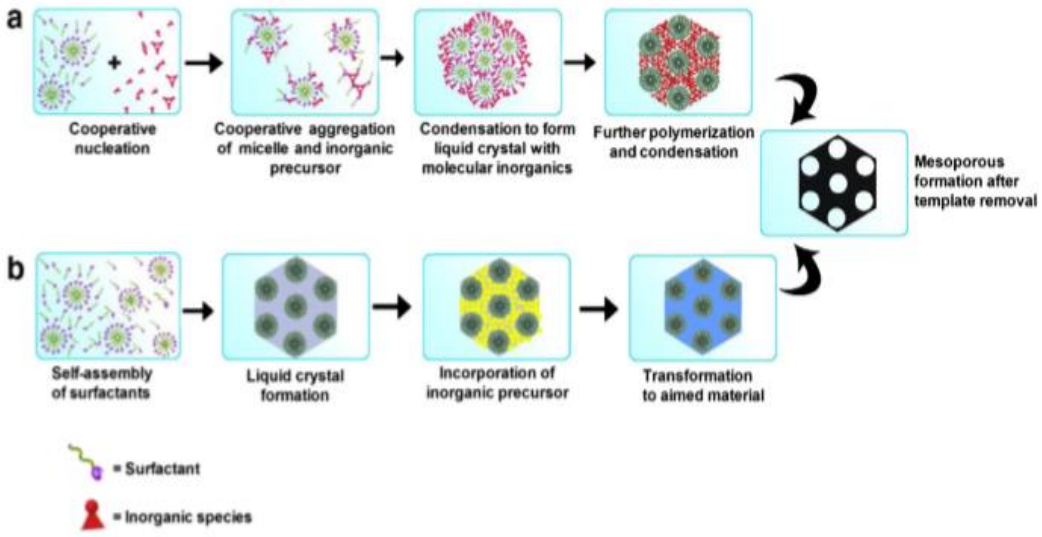

Figure 4. Formation of mesoporous structures: (a) via co-operative self-assembly, (b) via true liquid–crystal templating process [8].

Despite the attractive morphological properties of the mesoporous silicate materials, these materials are poor catalysts because of their chemically inert silicate skeleton. They do not exhibit, for example, interesting acid-base or redox properties. In order for some of the physical properties of these solids to be improved, such as total acidity (Lewis and Brønsted), hydrophobic or hydrophilic function, catalytic activity and thermal stability, modified MCM silicate materials were prepared containing metals and especially oxides of transition metals into the inorganic matrix. The most commonly modified MCM materials are these that contain ions of aluminum [10], vanadium [11], titanium [12], copper [13], cobalt [14], chromium and molybdenum [15] into the framework.

During the last two decades, synthetic chemists and material scientists have made extensive efforts in developing mesoporous structures by transition metal oxides. Thus, organized mesoporous solids have been synthesized and their structure, among others, consists solely of vanadium oxide (V_2O_5), titanium oxide (TiO_2), cerium oxide (CeO_2), iron oxide (Fe_2O_3), cobalt oxide (Co_2O_4) and chromium oxide (Cr_2O_3). Metal oxide mesoporous structures with large internal surface area and uniform pores constitute an interesting class of materials with a significant impact on various technological applications, including catalysis, adsorption and energy conversion [16,17,18,19,20]. Such materials combine complementary features into the inorganic structure such as mesoporosity and high catalytic activity.

1.2 Semiconductors and photocatalysis

Photocatalysis has become a field of great research interest and exhibits a variety of practical applications in industrial activities. These applications include, but are not limited to, organic pollutants mineralization (such as dyes and pesticides) [21], decontamination of water and wastewater effluents [22], production of renewable fuels (e.g. hydrogen and methane) [23], and organic synthesis (e.g. hydroamination of alkynes) [24]. In case of semiconductor photocatalysis, processes are occurred on a semiconductor/fluid interface irradiated with photons of appropriate energy. Semiconductors combine a variety of properties such as light absorption, electronic structure, charge transport and

excited-state lifetimes, thus they can be leveraged as photocatalysts [25]. A semiconductor is nonconductive in ground state because an energy gap (E_g), the bandgap, exists between the top of the filled valence band (VB) and the bottom of the vacant conduction band (CB). Consequently, electron transport between valence and conduction band must occur only with appropriate energy absorption. As depicted in Figure 5, in semiconductor photocatalysis, electrons get excited from the valence band to the conduction band when a photon with energy equal to or higher than the semiconductor bandgap is absorbed. This process creates an electronic vacancy or hole (h^+) at the valence band and a photogenerated electron (e^-) in the conduction band edge of the semiconductor. The light-induced generation of an electron-hole pair (exciton) is a required step in all semiconductor photocatalytic processes. These photogenerated species, when transferred to the solid/liquid interface, are capable of reducing and oxidizing a surface-absorbed substrate, whereas in the absence of suitable scavengers, electron-hole pair may undergo recombination on the surface within a few nanoseconds [26].

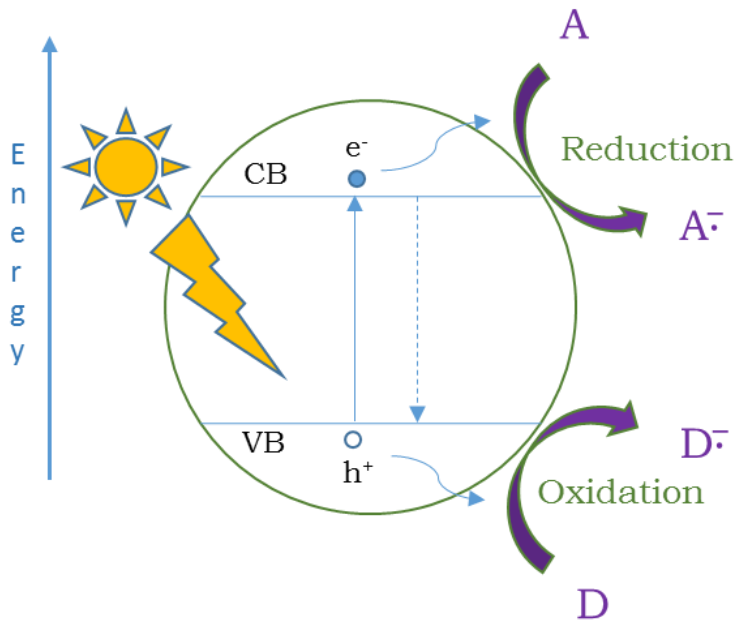

Figure 5. Schematic diagram of semiconductor photocatalysis.

The photocatalysis is chemically productive when the electron-hole pair recombination is suppressed. Conduction band electrons and valence band holes

can be separated efficiently in the presence of an intrinsic electric field, such as the one formed spontaneously in the space-charge region at the semiconductor/liquid or semiconductor/metal (Schottky) interface [27]. In this case the lifetime of photogenerated carriers increases, enhancing the possibility for electrons and holes to be involved in redox reactions on the photocatalyst surface. Interfacial electron transfer, that is transfer of an electron to or from a substrate adsorbed on the semiconductor surface, is a crucial step towards photocatalytic process. Notably, the efficiency of this step determines to a large extent the ability of the semiconductor to serve as a catalyst for a given redox transformation. In fact, the position of semiconductor's conduction and valence band edges relative to the redox potentials of the adsorbed substrates (reactants) determines the efficiency of the aforementioned electron transfer reaction. In order for an electron transfer reaction to occur, the potential of the electron acceptor should be located below (to a more positive direction) the conduction band of the semiconductor, whereas the potential of the electron donor should be located above (to a more negative direction) the valence band of the semiconductor [28,29]. (Figure 6).

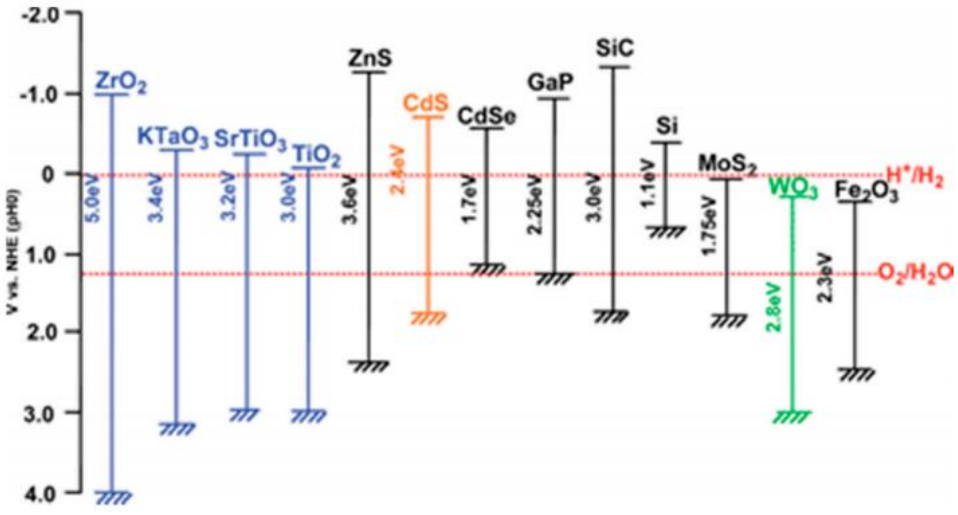

Figure 6. Bandgaps and band edge positions of representative semiconductors in relation to the redox potentials for water splitting at pH = 0 [30].

The electronic characteristics of conductors, semiconductors, and insulators can be understood by examining the electronic structure of these materials [31]. Due to the large number of atoms that interact in a solid material, the corresponding energy levels are tightly spaced, therefore a continuum of energy states (bands) is formed. The filling of bands as well as the size of the band gap in solid materials, segregate them in conductors, semiconductors and insulators (Figure 7). In general, electrons flow in a solid material when an electric field is applied under the following circumstances; Electrons should be in a partially filled band (valence band) or have access to the closest empty band (conduction band). In insulators, the bandgap is too large (more than 4 eV) as well as the valence band is completely filled with electrons, posing the flow of electrons impossible. On the contrary, in conductors like metals the bandgap is non-existent as there is an overlap between the valence and the conduction bands. Hence, the electrons can access empty levels within the conduction band and move freely across all atoms of the solid. A semiconductor is a special case between metals and insulators where the band gap is small enough (generally less than 4 eV) that can be bridged by electrons with sufficient energy. Usually, electrons get excited from valence band to conduction band by heating or light irradiation.

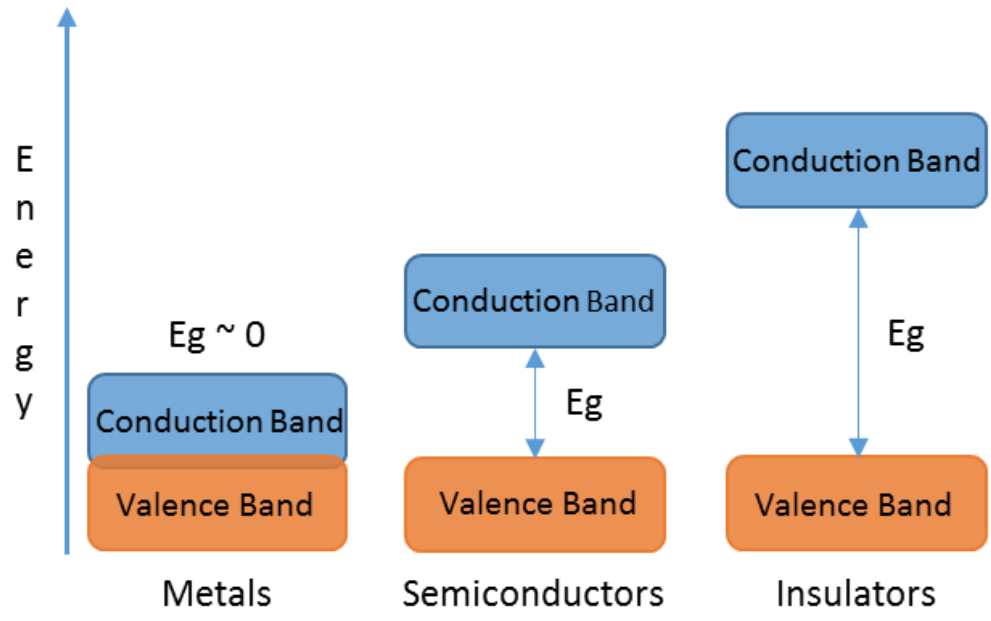

Figure 7. Energy bands in metals, semiconductors and insulators.

1.3 Environmental remediation and analyte detection

The rapid development of industrial activities has led to a series of environmental problems. For decades, large amounts of pollutants, such as hexavalent chromium (Cr(VI)) compounds, have been discharged and accumulated into the environment either intentionally or accidentally, releasing toxic metals in the water with great health and ecology concerns. Aquatic solutions of toxic metal ions (e.g. $HCrO_4^-$ anions) cause noxious properties and devastating effects on the groundwater and other sources of drinking water [32]. Therefore, an effective environmental remediation technique would be beneficial for our ecosystem.

In an effort to provide a complete solution, detoxification methods should be coupled with an efficient mechanism of detecting pollutants. In particular, chemical sensors in recent decades consist vital areas of instrumentation in modern analytical chemistry. Based on different mechanisms of molecular recognition [33], they are widely employed in clinical and environmental analysis. Powerful detection methods are crucial for an in-depth analysis of pollutants, therefore provide us with valuable insight which would be then incorporated in the next step of decontamination.

1.3.1 Hexavalent chromium: a serious environmental threat

The oxidation states of chromium range from +2 to +6, but only the hexavalent chromium (Cr(VI)) and trivalent chromium (Cr(III)) species are environmentally stable [34,35]. Hexavalent chromium represents a serious environmental pollution problem that is arising from various industrial activities such as electroplating, leather tanning, paint and pigments among others [36]. It is very soluble in water forming the most probable species of monovalent ($HCrO_4^-$) and divalent (CrO_4^{2-}) oxyanions, which have high mobility. Cr(VI) compounds are highly toxic and are responsible for carcinogens and mutagens in humans. According to the International Agency for Research on Cancer (IARC), Cr(VI) is classified as Group 1 carcinogen [37]. Most notably, the LD50 (Lethal Dose, 50%) value for Cr(VI) is between 50 and 150 mg Kg^{-1} in humans [38,39]. Because of its non-biodegradable nature, Cr(VI) can contaminate groundwater and shallow water wells with detrimental effects to the environment [40]. Hence, many countries regulate its

allowable limit concentration in drinking water. For example, US Environmental Protection Agency (EPA) has set the maximum contaminant level for total chromium in drinking water to be 0.1 mg L^{-1} [41]. Consequently, an effective and sustainable detoxification of Cr(VI)-bearing aqueous solutions is one of the high-priority research directions for environment and human health.

To date, a variety of techniques such as adsorption, ion-exchange, chemical precipitation, and biological, chemical and electrochemical reduction have been proposed for detoxification of aqueous Cr(VI) solutions [42,43,44]. Although successful, these techniques are costly, complicated, and require lengthy processing times. For instance, during chemical precipitation large amounts of residual sludge are generated. This sludge is difficult to manage, transport, and dispose, and there are associated high costs with each step [45]. Thus, development of new technologies is needed to address these problems. In the last years, light-induced photocatalytic reactions have gained a lot of attention for the purification of wastewater. Photocatalysis provides a compelling alternative to the energy-intensive conventional treatment methods as it uses renewable and pollution-free solar energy. Additionally, photocatalytic reaction conditions are mild and a lesser chemical input is required, as well as the secondary waste generation is minimal. Particularly, the photocatalytic reduction of Cr(VI) to Cr(III) over a semiconductor photocatalyst has been considered as a promising means for effective and sustainable detoxification of Cr(VI)-bearing solutions. The Cr(III) product is approximately 100 times less toxic than Cr(VI), is mostly immobile, environmentally friendly and can be easily removed from the solution as Cr_2O_3 or $Cr(OH)_3$ precipitates in alkaline environments [46]. Therefore, in recent years, researchers strive to neutralize the deteriorating effects of Cr(VI) to less nocuous Cr(III) form by photocatalytic reduction [47]. Apart from chromium, groundwater is contaminated by other pollutant factors such as colorless organic molecules and recalcitrant dyes. These compounds enhance the environmental threatening and increase the human contact with toxic organic chemicals [48], making their decontamination of outmost importance. As these organic compounds act as hole scavengers leading to a better photo-carrier separation at the solid/liquid interface, they can accelerate the overall catalytic process. This procedure is important since

not only results in the acceleration of Cr(VI) reduction processes but also in simultaneous decomposition of organic pollutants present in water.

So far, although many semiconductor materials have been investigated as potential photocatalysts for Cr(VI) reduction, such as TiO_2 [49,50], $Bi_{24}O_{31}Br_{10}$ [51], $NaTaO_3$ [52], SnS_2 [53], Ag_2S/Ag [54], CdS [55], $(AgIn)_xZn_{2(1-x)}S_2$ [56], g-C_3N_4 [57], their efficiency and cyclic stability are still not suitable for commercial applications. These materials generally suffer from a variety of drawbacks such as poor utilization of solar energy due to their large band gap (> 2.8 eV), short lifetime of photogenerated electron-hole pairs, low electrical conductivity, which adversely impact their viability for photocatalytic reactions. Furthermore, most of these catalysts, even though they have good water oxidation potential, operate in the presence of hole sacrificial reagents such as ascorbic acid, ethylenediaminetetraacetic acid (EDTA), formic acid and ammonium ions, which are essential to trigger Cr(VI) photocatalytic reduction [58]. This limits their utilization in detoxification of Cr(VI)-rich wastewaters. Therefore, the development of a stable and efficient photocatalyst for the simultaneous Cr(VI) reduction and water oxidation in aqueous solutions is of particular interest because of the simplicity and low cost of operation. However, the photooxidation of water to dioxygen ($2H_2O_{(l)} \rightarrow O_{2(g)} + 4H^+_{(aq)} + e^-$) is a sluggish reaction that involves several uphill reaction steps such as dissociation of OH^- species and formation of O–O bonds [59].

First row transition metal monoxides constitute an important group of materials due to their interesting physicochemical properties and numerous potential applications [60]. Cobalt monoxide (CoO) is an interesting semiconductor material with an energy band gap of 2.4–2.7 eV [61]. It typically crystalizes in two structures, the cubic rocksalt phase (space group *Fm*3*m*) where cations occupy the octahedral sites of the cubic close-packed (ccp) array of anions and the hexagonal wurtzite phase (space group *P*6*mc*) where cations are located at tetrahedral sites of the hexagonal close-packed (hcp) structure. These two distinct phases of hexagonal CoO (denoted as h-CoO) and cubic CoO (denoted as c-CoO) are formed by thermal decomposition of a cobalt precursor (e.g. $Co(acac)_3$, acac = acetylacetonate) under an inert atmosphere via kinetic and thermodynamic control experiments, respectively, as shown in Figure 8. In general, when two pathways are possible

from a common starting material, one route having a lower activation barrier rapidly affords a product, although this product is energetically less stable than that formed via the other route. In other words, the kinetic control of a reaction generates a thermodynamically less stable product, while the thermodynamic reaction control naturally yields a thermodynamically more stable product.

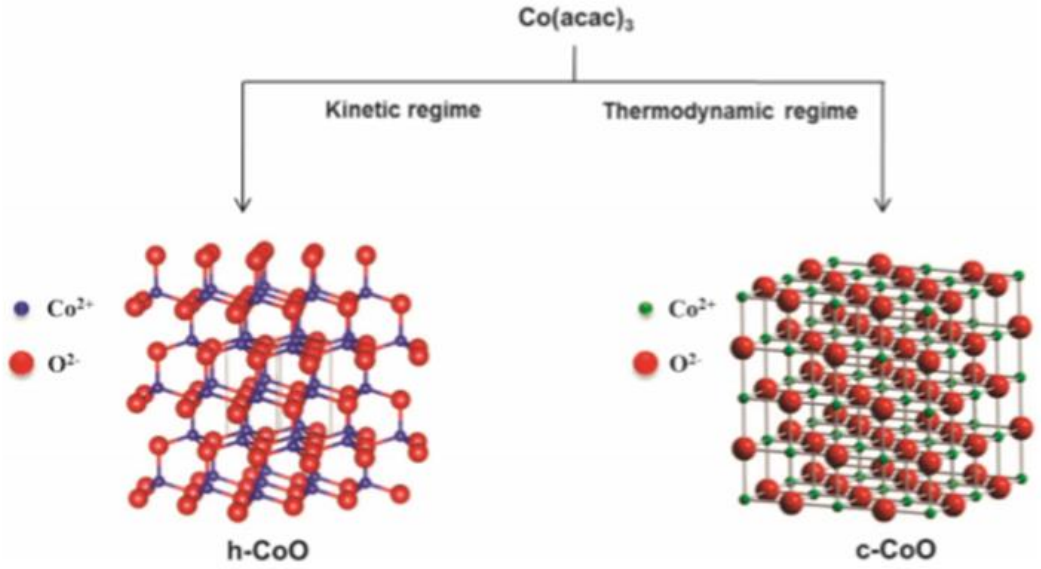

Figure 8. Selective formation of h-CoO and c-CoO structure [70].

Although cubic (ccp) structure of CoO is thermodynamically more stable, the relatively unstable hexagonal form of CoO shows interesting electrical, optical, magnetic, and electrochemical properties [62,63] that are useful for a variety of potential applications such as catalysis, gas sensors, magnetic data storage devices and lithium-ion batteries [64,65]. A phase that is thermodynamically less stable is hardly observed in bulk forms. However, in the nanoscale range, the surface energy exceeds the crystal formation energy of the particles, stabilizing an unstable phase of the nanostructured material and dominating all of its physicochemical properties [66,67,68,69]. Importantly, a thermodynamically unstable phase can be stabilized by coupling the excess surface energy of nanomaterials with careful control of kinetic parameters in synthetic reactions [70]. Currently the fabrication of CoO materials at the nanoscale has been the subject of extensive research in photoelectrochemical cells and magnetic nanodevices [71]. For instance, recently Liao et al. designed CoO nanoparticles with tunable band-edge positions and demonstrated their high activity for photocatalytic water splitting [72].

1.3.2 Surface-enhanced Raman scattering (SERS) in trace analysis detection of analytes

Surface-enhanced Raman scattering (SERS) is a powerful analytical technique that extends the range of Raman applications and allows highly sensitive structural detection of organic analytes at very low concentrations [73,74,75,76]. In this way, trace analysis such as part per million (ppm) level detection of toxic molecules (e.g. organic dyes) that may contaminate water has become possible, opening new chances in the environmental world.

Mesoscopic architectures made of abundant and inexpensive metal nanoparticles are highly desirable for sustainable and cost-effective catalysis, energy conversion, light-emitting nanodevices and optical sensing [77]. In principle, small-sized nanoparticles have the ability to provide high surface-to-volume ratio, while exhibit distinct physical characteristics that are completely different from those of the bulk phases. In this context, copper (Cu) nanoparticles have emerged as exceptionally promising materials for redox catalysis, nanophotonic devices and biological sensors because of their low cost, high electrical conductivity and large plasmonic tunability [78,79,80,81]. Studies of this system have been facilitated by rapid progress in the synthetic methods and, so far, a variety of Cu nanoparticles with desired shape, size and crystal structure have been prepared. Nonetheless, the great instability in air and the readily oxidization to copper oxides (Cu_xO), even after a few minutes of air exposure [82,83], the limited interparticle electron transfer and high propensity to agglomeration of isolated Cu nanoparticles pose serious problems for practical applications [84]. This means that only a small fraction of the total nanoparticle's surface being accessed to the target molecules. In fact, this point can be further extended to other systems, which has already become a fundamental issue to many colloidal nanoparticle solutions.

To overcome these limitations, different chemical methods have been employed to enhance the electrochemical performance and chemical stability of Cu nanoparticles. One of the most attractive methods is to stabilize copper nanoparticles on various high-surface-area host materials, especially 2D graphene and multilayer graphite nanosheets [85,86,87]. As a consequence, various nanostructures have been prepared by either supporting Cu nanoparticles on the

graphene sheets [88,89] or encapsulating Cu nanoparticles within the graphene layers [90]. The graphene matrix not only endows the nanoparticles with improved chemical stability, but also impart them with new functionalities. Such hybrid materials have been demonstrated, for example, to be efficient catalysts for a diverse set of catalytic organic reactions, including coupling of terminal alkynes [91], Suzuki-Miyaura cross-coupling reaction of aryl halides [92], C–H arylation of arenes [93] and phenols [94], addition of anilines [95] and reduction of olefins [96]. More recently, graphite decorated Cu (Cu/G) nanoparticles have been the subject of intense research for their use in SERS applications. However, the integration of nanoscale building blocks, like metal nanoparticles, into high surface-to-volume ratio porous architectures is not trivial because of the high surface reactivity of nanoparticles which causes serious problems for most chemical methods, such as agglomeration of nanoparticles into large particles. Currently, the synthesis of these nanostructures is restricted to the use of precise nanofabrication techniques such as nanolithography, electron- or ion-beam pattering and atomic layer deposition (ALD) which, however, are time-consuming, costly and complicated [97].

Intrinsically, metallic nanoparticles with strong surface plasmon resonance (SPR) effect in the visible and near-IR region of the electromagnetic spectrum, such as the copper nanoparticles, are effective for SERS applications. A rough metal substrate based on plasmonic nanoparticles is required since at the interparticle cavities and gaps (hot spots) of the plasmonic nanoparticles (Figure 9) an intense electromagnetic field can be generated under excitation of an incident laser beam, resulting in enhanced Raman signals of the absorbed analytes. This mechanism is referred as *electromagnetic enhancement* (EM), which can reach up to 10^8 or more times of the original (without support) signal [98]. Additionally, there is another mechanism which results in the amplification of the signal, called *chemical enhancement* (CM), but with a lower enhancement factor. Chemical enhancement involves charge transfer mechanisms where the excitation wavelength is resonant with the metal-molecule charge transfer electronic states [99]. The total SERS enhancement factor usually is the result of the combined effect of the electromagnetic and chemical mechanisms.

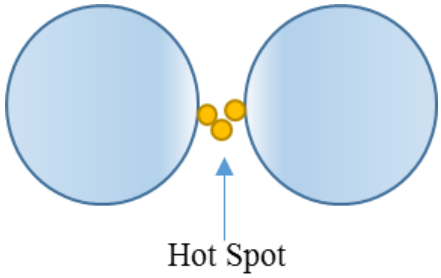

Figure 9. Organic molecules (dyes) trapped in a hot spot generating intense electromagnetic field between the nanoparticles.

Graphene has the ability to generate strong chemical enhancement by offering a large surface for molecules to be adsorbed through π-π interactions and an effective charge transfer efficiency, thus attracting the attention for SERS applications [100]. On the other hand, graphene alone exhibits a minor enhancement factor. Thus, combining graphene with metallic nanoparticles interesting synergetic effects can be observed. Due to the efficient adsorption of analyte molecules thought dipole-dipole interactions with the graphite matrix and the strong electromagnetic-field enhancement at the graphite/Cu interface, Cu/G hybrid materials have exhibited extraordinary SERS activity and selectivity [101,102]. Notably, materials of this type demonstrate similar or even higher levels of SERS sensitivity than periodic arrays of 100 times more expensive Au and Ag nanoparticles [103,104]. Unfortunately, although promising, inherent problems such as poor dispersibility of metal nanoparticles within graphite layers and fusion of nanoparticles in close-packed microstructures with limited porosity still remain serious challenges. Therefore, from a sustainable development perspective, it is highly desirable to develop novel strategies to assemble functional mesostructures from discrete nanoparticles that exhibit adaptive properties and morphologies.

1.4 Thesis statement and Contributions

The ever-increasing industrial activities have led to the disposal of byproducts containing toxic metals, organic dyes, among others that pose a significant environmental and health issue. Highly toxic metals, like Cr(VI), can easily contaminate groundwater, constituting its detoxification from aqueous solutions an important yet challenging topic to the research community. Although several

methods of Cr(VI) decontamination exist, they exhibit considerable drawbacks (cost, complexity etc.), so that their use is a double-edged sword to some extent. Apart from detoxification, an effective detection of pollutants in trace concentrations is also mandated. In the scope of SERS detection, the synthesis of appropriate sensor materials in a cost-effective and non-complicated way is also obligatory.

In this dissertation, the scope of my work is to produce new mesoporous networks of connected metal and metal-oxide nanoparticle for environmental applications such as detection of pollutants and photocatalytic reduction of aqueous Cr(VI). In particular, it is presented the fabrication of highly porous Cu nanoparticle assemblies decorated with graphite layers (denoted as Cu/G NPAs) from the *in-situ* reduction and self-assembly of colloidal CuO nanoparticles, as well as their use in SERS detection. The materials that are reported here represent the first example of graphite-decorated Cu nanoparticle assemblies that exhibit a multitude of hot spots across a 3D nanoscale porous structure with large internal surface area and uniform pores. All these characteristics make the Cu/G NPAs a suitable plasmonic platform for chemical sensing. In more detail, we found that Cu/G assemblies attain a significant improvement in SERS performance by detecting trace amounts of rhodamine 6G (R6G) and aniline molecules. Moreover, the as-prepared Cu/G hybrid materials can conduct SERS analysis with a satisfactory level of sensitivity and reproducibility.

Furthermore, it is reported the synthesis of new mesoporous CoO materials (both in hexagonal and in cubic structure) from the polymer-assisted cross-linking of colloidal CoO nanoparticles. This is the first time that it is demonstrated the application of CoO single-component assemblies in photocatalytic reduction of Cr(VI) to Cr(III). The construction of a continuous network of connected nanoparticles with open-pore structure and high internal surface area constitutes a challenging issue for synthetic chemists mainly because of the aggregation tendency of the nanoparticles into large microstructures with limited porosity. The resulting assembled frameworks possess an inherently large pore surface, which provides a large number of exposed active sites for reactions. It is shown that hexagonal CoO nanoparticle-linked networks can serve as an efficient photocatalyst to drive Cr(VI) reduction and water oxidation with high efficiency

and stability under UV and visible light irradiation. Also, by using a combination of control catalytic experiments and spectroscopic studies, we provide insights into the reaction mechanism of these systems. Similar studies to the hexagonal CoO have been conducted with mesoporous assemblies consisting of cubic-phased CoO nanoparticles. Even though cubic CoO nanoparticles do not exhibit comparable performance like their hexagonal counterparts, they are inherently more stable. To this end, we seek ways to improve the photocatalytic performance of cubic CoO nanoparticles by doping the crystal structure with nickel (Ni) and copper (Cu) impurities. The activity of the resulting Ni- and Cu-doped cubic CoO nanoparticle assemblies is evaluated in the photocatalytic reduction of Cr(VI).

2

Experimental Section

2.1 Synthesis of CuO nanoparticles

CuO nanoparticles with an average diameter of 5–6 nm were prepared according to literature procedure [105]. In a typical reaction, 3 mmol of copper(II) acetate (98%, Sigma-Aldrich) and 8.7 mmol of glacial acetic acid (99.7%, Sigma-Aldrich) were added in 150 mL of water. After slowly heating to reflux, a total amount of 10 mL NaOH (> 98%, Sigma-Aldrich) aqueous solution (0.04 g mL^{-1}) was added under vigorous stirring to precipitate the nanoparticles. The nanoparticles were isolated by centrifugation, washed with ethanol (Sigma-Aldrich) and dispersed in water to form a stable colloidal solution (130 mg mL^{-1}).

2.2 Synthesis of mesoporous Cu/G NPAs

In a typical synthesis of graphite-decorated Cu nanoparticle assemblies (Cu/G NPAs), 0.3 g of poly(ethylene glycol)$_{20}$-*block*-poly(propylene glycol)$_{70}$-*block*-poly(ethylene glycol)$_{20}$ (PEG-*b*-PPG-*b*-PEG, $M_n \approx 5800$ g mol^{-1}) block copolymer (BCP, Sigma-Aldrich) were dissolved in 1.5 mL of water. To this solution, 1.5 mL of colloidal CuO nanoparticle solution in water (130 mg mL^{-1}) was added dropwise and the mixture was stirred at room temperature for 2 h. Then, the resulting mixture was placed in an oven at 60 °C and left under static conditions within 3–4 days until complete evaporation of the solvent. This procedure yields a brown-red that was subsequently heated to 350 °C for 4 h under N_2 flow (~50 cm^3 min^{-1}), using a heating rate of 1 °C min^{-1}, to yield the mesoporous product with simultaneous removal of the template and reduction of Cu(II) to Cu(0).

2.3 Fabrication of Cu/G NPAs films

For a typical procedure for fabricating the Cu/G NPAs thin film, 5 mg of Cu/G NPAs, 15 mg of α-terpineol (>96%, Alfa Aesar) and 6 mg of ethyl cellulose (44-51% ethoxy groups, Alfa Aesar) were dispersed in 1 mL ethanol by sonication to form a homogeneous solution. After evaporation of ethanol under reduce pressure, the colloidal ink was drop-casted on a clean glass slide. The casted film was drying for about 10 min at 120 ^{o}C to remove α-terpineol and then heated for 1 h at 300 ^{o}C under vacuum to remove ethyl cellulose, forming a homogeneous 3 μm-thick layer (Figure 10). The apparent area on the glass slide coated with the Cu/G NPAs powder was 1 cm^2.

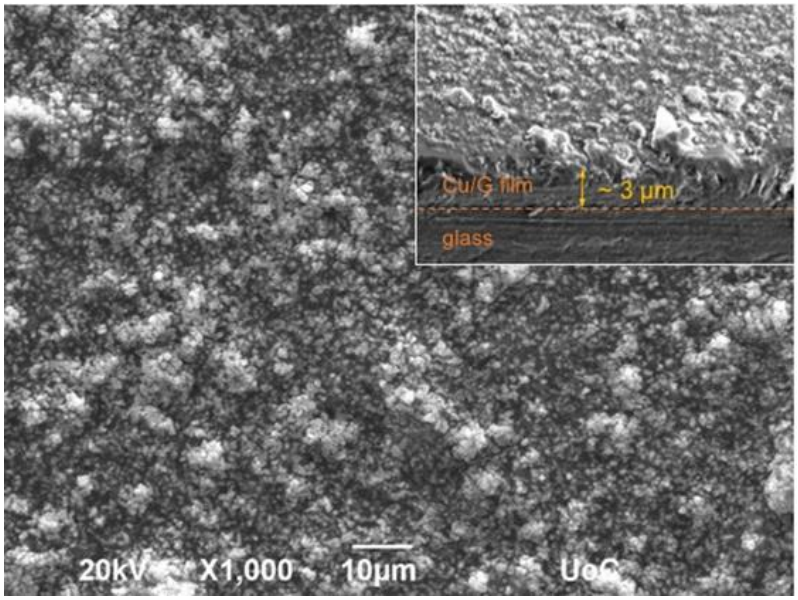

Figure 10. Typical top view and cross-sectional (inset) SEM images of Cu/G NPAs film deposited on glass substrate.

2.4 Synthesis of Cu nanoparticles

Cu nanoparticles with an average diameter of 100 nm were prepared according to the reported procedure [106]. In a typical reaction, copper (II) nitrate trihydrate (Alfa Aesar) was dissolved in the solution of sodium hydroxide and glycerol (99%, Sigma-Aldrich) with molar ratio of $Cu(NO_3)_2 \cdot 3H_2O$:NaOH:glycerol 0.02:0.1:1. This mixture was then slowly heated to 140°C for 20 min until the reduction

reaction became completed. The copper particles were then separated by centrifugation and washed with absolute ethanol for several times. Significant effort was made to minimize the air exposure of the copper samples.

2.5 Fabrication of Graphene layers

Graphene layers were prepared by pyrolysis of alginate at 1000 ^{o}C under Ar atmosphere.

2.6 SERS Measurements

In a typical experiment, 1 mL of ethanol containing 0.1 to 10 μmol of R6G (Sigma-Aldrich) or 0.1 μmol aniline (Sigma-Aldrich) was deposited on the as-synthesized Cu/G NPAs films (Figure 11). Prior to the measurement, all substrates were dried at 60 ^{o}C under vacuum for 2 h to remove ethanol. All the SERS spectra were acquired under identical conditions, i.e. using a 473-nm excitation laser wavelength with a 5-mW laser power and a 20-s acquisition time, on a Nicolet Almega micro-Raman spectrometer.

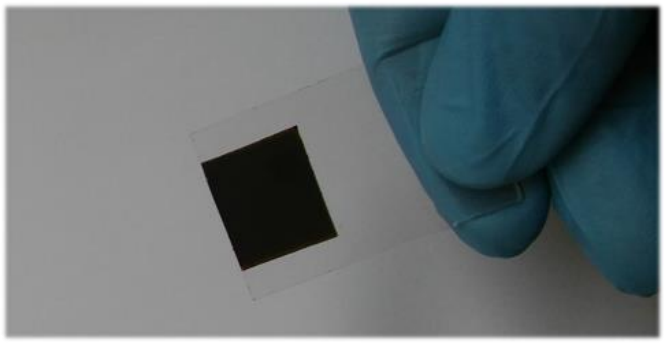

Figure 11. Photograph of the Cu/G NPAs film on glass substrate.

2.7 Synthesis of h-CoO nanoparticles

h-CoO nanoparticles were prepared according to literature procedure [107]. Briefly, 1.5 mmol of $Co(acac)_3$ (98%, Sigma-Aldrich) and 300 mmol of oleylamine

(70%, Sigma-Aldrich) were heated at 135 °C under inert atmosphere for 5 h. The resulting brown solution was then flash-heated to 200 °C and annealed for 3 h, giving a green suspension. Next, the supernatant was removed by centrifugation retrieving the CoO nanoparticles in a powdery form. The h-CoO nanoparticles were then dispersed in hexane (95%, Sigma-Aldrich) to form a stable colloidal solution (10 mg mL^{-1}).

2.8 Synthesis of Ni and Cu-doped c-CoO nanoparticles

c-$Co_{1-x}Ni_xO$ and c-$Co_{1-x}Cu_xO$ (x = 0, 0.01, 0.02 and 0.05) nanoparticles were prepared according to a modified literature procedure [108]. For a typical synthesis of $Co_{0.98}Ni_{0.02}O$ or $Co_{0.98}Cu_{0.02}O$ nanoparticles, 1.47 mmol of $Co(acac)_3$ (98%, Sigma-Aldrich), 0.03 mmol of $Ni(NO_3)_2 \cdot 6H_2O$ or $Cu(NO_3)_2 \cdot 2.5H_2O$ (98%, Sigma-Aldrich) and 300 mmol of oleylamine (70%, Sigma-Aldrich) were heated at 135 °C under inert atmosphere (N_2 flow) for 5 h. The resulting brown solution was then slowly heated to 200 °C and annealed for 3 h, giving a brown suspension. Next, the supernatant was removed by centrifugation, retrieving the $Co_{0.98}Ni_{0.02}O$ or $Co_{0.98}Cu_{0.02}O$ nanoparticles in a powdery form. The $Co_{0.98}Ni_{0.02}O$ or $Co_{0.98}Cu_{0.02}O$ nanoparticles were then dispersed in hexane (95%, Sigma-Aldrich) to form a stable colloidal solution (10 mg mL^{-1}). Similar procedure was followed for the synthesis of 1% and 5% Ni-doped or Cu-doped CoO nanoparticles, utilizing 1.485 mmol and 0.015 mmol or 1.425 mmol and 0.075 mmol of $Co(acac)_3$ and $Ni(NO_3)_2 \cdot 6H_2O$ or $Cu(NO_3)_2 \cdot 2.5H_2O$, respectively. Pure c-CoO nanoparticles were also prepared using 1.5 mmol of $Co(acac)_3$.

2.9 Ligand exchange of h-CoO, c-$Co_{1-x}Ni_xO$ and c-$Co_{1-x}Cu_xO$ nanoparticles

The surface of CoO/c-$Co_{1-x}Ni_xO$/c-$Co_{1-x}Cu_xO$ nanoparticles was modified with $NOBF_4$ by a ligand-exchange process according to a previously reported method [109]. In detail, a dispersion of CoO/c-$Co_{1-x}Ni_xO$/c-$Co_{1-x}Cu_xO$ nanoparticles in hexane (6 mL) was added to a solution of $NOBF_4$ (60 mg, 97%, Acros Organics) in DMF (6 mL, 99.9%, Sigma-Aldrich) and the mixture was stirred at room

temperature until the nanoparticles were transferred to the DMF phase. The BF_4^--capped CoO/c-$Co_{1-x}Ni_xO$/c-$Co_{1-x}Cu_xO$ nanoparticles were then collected by precipitation with toluene (99.7%, Sigma-Aldrich), followed by centrifugation. The BF_4^--capped CoO nanoparticles were dispersed in DMF to form a stable colloidal solution of 120 mg mL^{-1}.

2.10 Synthesis of h-CoO, c-$Co_{1-x}Ni_xO$ and c-$Co_{1-x}Cu_xO$ MNAs

For a typical synthesis of mesoporous hexagonal-phased CoO nanoparticle assemblies (h-CoO MNAs), 0.2 g of block copolymer Pluronic F127 ($OH(CH_2CH_2O)_{100}(CH(CH_3)CH_2O)_{64}$ $(CH_2CH_2O)_{100}H$, M_n ~ 12000, Sigma-Aldrich) were dissolved in 1.5 mL of tetrahydrofuran (THF, >99%, Sigma-Aldrich) with continuous stirring. To this solution, 0.5 mL of colloidal h-CoO nanoparticle solution in DMF was added dropwise and the mixture was stirred at room temperature for 2 h. Then, the resulting mixture was placed in an oven at 40 °C and left under static conditions for about 5–6 days to gives a mesostructured h-CoO/polymer composite. The resulting dry powder was subsequently heated to 350 °C for 4 h under N_2 flow (~50 cm^3 min^{-1}), using a heating rate of 1 °C min^{-1}, to yield the mesoporous product. Similar procedure was followed for the synthesis of 1%, 2%, 5% Ni-doped and Cu-doped c-CoO MNAs. For comparison, random aggregates of h-CoO nanoparticles (h-CoO RNAs) were also prepared, following a similar procedure to that of h-CoO MNAs, but in absence of template. Porous assemblies of Co_3O_4 nanoparticles (Co_3O_4 MNAs) were also obtained by heating the CoO/polymer composite at 350 ºC for 4 h in air.

2.11 Photocatalytic reactions

In a typical procedure, a quantity of catalyst (10–20 mg) was dispersed in 50 mL of 50 mg L^{-1} Cr(VI) aqueous solution, which were prepared by dissolving $K_2Cr_2O_7$ into deionized (DI) water. The pH of the solution was adjusted to the desired values with dilute sulfuric acid. Prior to irradiation, the suspension was magnetically stirred in the dark for 30 min to ensure equilibrium. The photocatalytic reaction was performed by irradiating the solution with UV–visible or visible light, using a

300 W Xe lamp (Variac Cermax) with cut-off filters allowing $\lambda > 360$ nm or $\lambda \geq 420$ nm, respectively. All the experiments were carried out at 20 ± 2 ^{o}C using a water bath cooling system. During reaction, the concentration of Cr(VI) in the solution was monitored via 1,5-diphenylcarbazide (DPC) colorimetric method, using a Perkin Elmer Lambda 25 UV–vis spectrometer. The normalized concentration (C/C_o) of Cr(VI) solution at different illumination times was calculated as proportional to the absorbance of the DPC–Cr(VI) complex at 540 nm (normalized to the initial absorption). Control experiments were carried out with the addition of citric acid, EDTA (1 equiv.) and phenol (1 equiv., 10 equiv.) in the reaction mixture. Analysis of the reaction products was performed by extracting the organic compounds with ethyl acetate and then analyzing the extract by GC-MS (Shimadzu GCMS-QP2010 Ultra).

Figure 12. Layout of photocatalytic Cr(VI) reduction experiments with a 300-W Xe lamp.

For the photooxidation of water to oxygen, 15 mg of h-CoO or c-$Co_{0.98}Ni_{0.02}O$ MNAs catalyst and 50 mL of 50 ppm Cr(VI) aqueous solution (pH = 2) were placed into a 100-mL airtight quartz tube. The temperature of the suspension was maintained at 20 ± 2 ^{o}C by using an external water cooling system. Prior irradiation, the mixture was purged with argon for at least 30 min under atmospheric pressure to remove any dissolved air. The photocatalytic reaction took place under

irradiation of a 300 W Xe lamp ($\lambda > 360$ nm). The oxygen generated from the reaction was analyzed with a gas chromatograph (Shimadzu GC-2014) equipped with a thermal conductivity detector, using Ar as a carrier gas.

The apparent quantum yield (AQY) of each catalyst was calculated by analyzing the amount of reduced Cr(VI) at a given monochromatic irradiation, using LED light with wavelengths of 375, 410 and 440 nm, respectively:

$$\text{AQY} = \frac{3 \times \text{number of reduced Cr(VI)}}{\text{number of incident photons}} \quad (1)$$

The intensity of the incident light was measured using a StarLite energy meter equipped with a FL400A-BB-50 fan-cooled thermal sensor (Ophir Optronics Ltd, Jerusalem).

2.12 Physical characterization

Thermogravimetric analyses were performed using a Perkin Elmer Diamond analyzer. Thermal analysis was conducted from 40 to 600 ^{o}C in air or nitrogen atmosphere (~200 mL min^{-1} flow rate) with a heating rate of 5 ^{o}C min^{-1}.

Powder X-ray diffraction (XRD) patterns were obtained with a PANalytical X´Pert Pro MPD X-ray diffractometer (45 kV and 40 mA) using Cu Kα radiation (λ = 1.5406 Å) in the Bragg–Brentano geometry.

Scanning electron microscope (SEM) images were obtained using a JEOL Model JSM-6390LV electron microscope operated at 20 kV.

Transmission electron microscopy (TEM) images were taken with a JEOL JEM-2100 electron microscope, equipment with a LaB_6 filament, operating at 200 kV accelerating voltage. Samples were prepared by suspending fine powders in ethanol and then drop casting on a holey carbon-coated Cu grid.

Elemental microprobe analyses were performed by a JEOL JSM-6390LV scanning electron microscope (SEM) equipped with an Oxford INCA PentaFETx3 energy-dispersive X-ray spectroscopy (EDS) detector (Oxfordshire, UK). Data acquisition

was performed at least five times for each sample using an accelerating voltage of 20 kV and a 100-s accumulation time.

Elemental C, H and N analysis was performed on a PerkinElmer 2400 Series II CHNS/O instrument.

XPS measurements were carried out using a mon-monochromatic Mg K_α line at 1253.6 eV (12 kV with 20 mA anode current) and a Leybold LH EA11 electron energy analyzer operated at a constant pass energy of 100 eV. The analyzed area was a 1.5×5 mm^2 rectangle, placed near the center of the powder-covered area on each specimen surface. In all XPS spectra, the binding energy of the predominant aliphatic contribution to the C 1s peak at 284.8 eV was used as a reference.

Nitrogen adsorption and desorption isotherms were measured at –196 ^oC on a Quantachrome NOVA 3200*e* sorption analyzer. Prior to measurement, samples were degassed at 100 ^oC under vacuum ($<10^{-5}$ Torr) for 12 h. The specific surface areas were calculated using the Brumauer-Emmett-Teller (BET) method [110] on the adsorption data in the relative pressure range of 0.05–0.22. The total pore volumes were estimated from the adsorbed amount at the relative pressure (P/P_o) of 0.98, and the pore size distributions were obtained from the adsorption branch of the isotherms, using the non-local density functional theory (NLDFT) method [111].

Diffuse reflectance UV–vis/near-IR spectra were collected using on a Perkin Elmer Lambda 950 optical spectrophotometer. $BaSO_4$ powder was used as a 100% reflectance standard and base material on which the powder sample was coated. Diffuse reflectance data were converted to absorption using the Kubelka-Munk function $\alpha/S = (1–R)^2/(2R)$, where R is the measured reflectance and α, S are the absorption and scattering coefficients, respectively [112]. The energy bandgap (E_g) of the samples were estimated from Tauc plots of $(\alpha h\nu)^2$ *versus* photon energy.

Fluorescence spectra were obtained at room temperature on a Lumina Fluorescence spectrometer (Thermo scientific) equipped with a 150 W Xe lamp.

Infrared (FT-IR) spectra were recorded on a Perkin Elmer Model Frontier FT-IR spectrometer with 2 cm^{-1} resolution. Samples were prepared as KBr pellets.

The Raman spectra of the Cu/G NPAs were collected on a Nicolet Almega XR micro-Raman spectrometer using a laser line at 473 nm wavelength.

2.13 Electrochemical measurements

Mott-Schottky measurements were performed in a 0.5 M Na_2SO_4 aqueous electrolyte (pH = 7) using a Metrohm Autolab PGSTAT 302N potentiostat. A three-electrode set-up, with a platinum plate (1.0 × 2.0 cm^2) and a silver-silver chloride (Ag/AgCl, 3M KCl) as the counter and reference electrodes, respectively, was adopted to study the samples. The capacitance of the semiconductor/electrolyte interface was obtained at 1 kHz, with 10 mV AC voltage amplitude.

For Nyquist plots a small AC perturbation of 20 mV was applied to the electrodes, and the different current output was measured throughout a frequency range of 1 to 10^6 Hz. The steady state DC bias was kept at 0 V (open-circuit potential) throughout the electrochemical impedance spectroscopy (EIS) experiments. All these experiments were conducted under dark conditions. The measured potential *vs* the Ag/AgCl reference electrode was converted to the normal hydrogen electrode (NHE) scale using the formula: $E_{NHE} = E_{Ag/AgCl} + 0.210$ V.

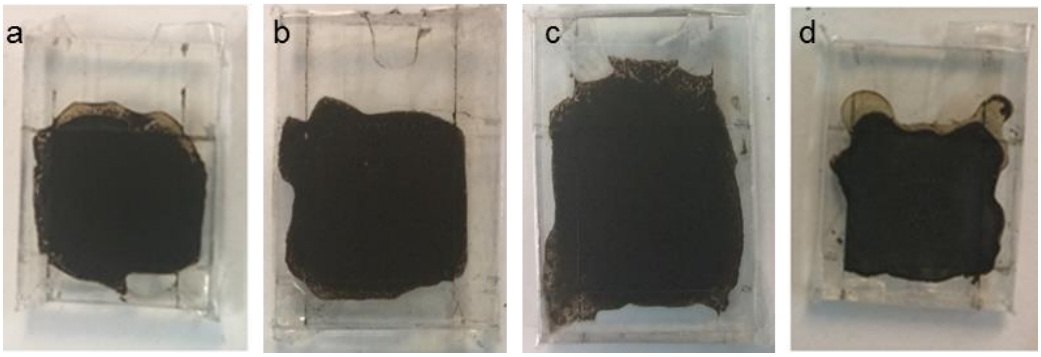

Figure 13. Typical photographs of (a) CoO, (b) $Co_{0.99}Ni_{0.01}O$, (c) $Co_{0.98}Ni_{0.02}O$ and (d) $Co_{0.95}Ni_{0.05}O$ MNAs thin films deposited on FTO-coated glass for EIS characterization.

The working electrodes for impedance-potential measurements were fabricated as follows: 10 mg of each sample was dispersed in 1 mL DI water and the mixture

was subjected to sonication in a water bath until a uniform suspension was formed. After that, 40 μL of the suspension was drop-casted onto the surface of fluorine-doped tin oxide (FTO, 9 Ω/sq) substrate, which was masked with an epoxy resin to expose an effective area of 1.0 × 1.0 cm^2 (Figure 13). The sample was dried in a 60 ^oC oven for 30 minutes.

2.14 Photoelectrochemical measurements

Photoelectrochemical measurements were carried out in an air-tight three-electrode cell with the samples as the working electrode (1 cm^2 illumination area), an Ag/AgCl (3 M KCl) as the reference electrode, and a platinum wire as the counter electrode. Photocurrent data were collected at a potential of 1 V (*vs* Ag/AgCl) in 0.5 M KOH aqueous electrolyte. Before analysis, the electrolyte was purged with N_2 for 30 min to remove the oxygen. The photocurrent densities of the samples were measured using a Metrohm Autolab PGSTAT 302N potentiostat coupled with a neutral white light-emitting diode (WLED, λ = 420 – 760 nm).

2.15 Calculation of R_{ct} from EIS data

The equivalent circuit model $R_s(Q_f/(R_{ct}L_{ad})Q_2)$ (see inset of Figure 91) was used to simulate the EIS data of the fabricated $Co_{1-x}Ni_xO$ (x = 0–0.05) MNAs electrodes. R_s represents the electrolyte resistance, R_{ct} is the charge-transfer resistance, and Q_f and Q_2 elements account for the defect resistance (pores, cracks and grain boundaries) of the solid film and the double layer capacitance, respectively. In addition, an inductor (L_{ad}) to the proposed circuit model, which account for the pseudo-inductive behaviour in the high frequency domain (often causing by disordered charge-carrier relaxation and disordered movement of redox species at the surface of electrode) [113,114] was also necessary for fitting the experimental results.

2.16 Theoretical calculations

Density functional theory (DFT) calculations were performed using the Vienna *ab initio* Simulation Package (VASP) [115]. The projector augmented wave method (PAW) for the core electrons and the nuclei was used [116]. For the exchange-correlation functional, we tested both the generalized gradient approximation (GGA) of Perdew–Burke–Ernzerhof (PBE) [117] and the local density approximation (LDA) [118]. It was found that LDA describes the electronic structure of c-CoO as a semiconductor better than GGA-PBE, in agreement with previous works [119]. Thus, results reported here are from LDA calculations only. In order to account for the on-site repulsion between d electrons, DFT+U within Dudarev's approach was adopted with U-J parameter values of 4 and 7 for Co and Ni, respectively [120]. Wave functions were expanded on a plane wave basis set with a 512-eV kinetic energy cutoff. Ground state was in the antiferromagnetic (AFM) configuration. Simulation cells of several sizes were used in order to examine doping in bulk c-CoO with different Ni concentrations.

3

Results and Discussion

Part I: SERS detection of analytes

3.1 Synthesis and structural properties of Cu/G NPAs

A schematic overview of the mesoporous Cu/G nanoparticle assemblies (NPAs) synthesis by the polymer-templated aggregating self-assembly process is illustrated in Figure 14 [121]. In particular, first a CuO nanoparticle colloidal solution was slowly added to a clear aqueous solution of poly(ethylene glycol)$_{20}$-*block*-poly(propylene glycol)$_{70}$-*block*-poly(ethylene glycol)$_{20}$ (PEG-*b*-PPG-*b*-PEG, $M_n \approx 5800$ g mol^{-1}) block copolymer (BCP). The reaction mixture was kept under vigorous stirring for about 2 h and then placed in an oven at 60 ^{o}C until complete evaporation of the solvent yielding a brown-red gel. To facilitate self-assembly at the polymer interface, precursor CuO nanoparticles were coated with acetate (CH_3COO^-) ligands. In this case, the polyvalent ligand-BCP interactions (e.g. ionic and hydrogen bonding interactions) can favor the absorption of nanoparticles within the polymer aggregates instead of self-aggregation of nanoparticles in solution [122].

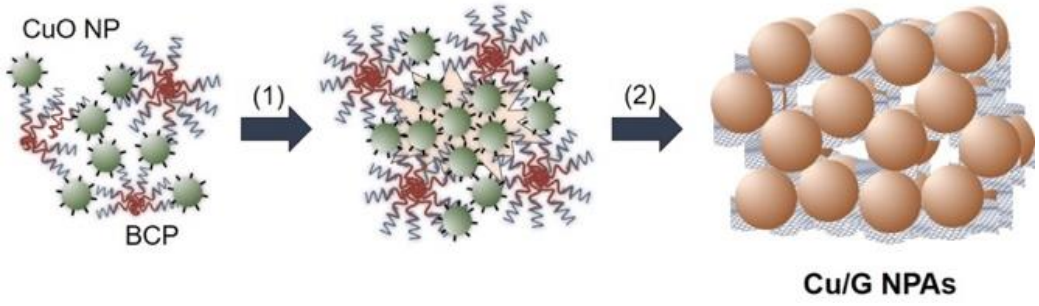

Figure 14. Schematic representation of the synthesis of Cu/G NPAs: (1) BCP/CuO nanoparticles self-assembly and (2) mesoporous Cu/G nanoparticle replica of the polymer aggregates after heating process (NP: nanoparticle, BCP: block copolymer).

In addition, the solvent used for the synthesis was chosen to provide good solubility of both colloidal CuO nanoparticles and polymer template. Under these reaction conditions, the CuO nanoparticles preferentially segregate to the BCP interface, allowing the formation of mesostructured BCP/nanoparticle composites. Finally, removal of the template and reduction of Cu(II) to Cu(0) were achieved simultaneously through a one-step annealing process in which the gel product was gently pyrolysed at 350 ^{o}C (using a 1 ^{o}C min^{-1} heating rate) under nitrogen flow for 4 h. The as-obtained material was foam-like and brown.

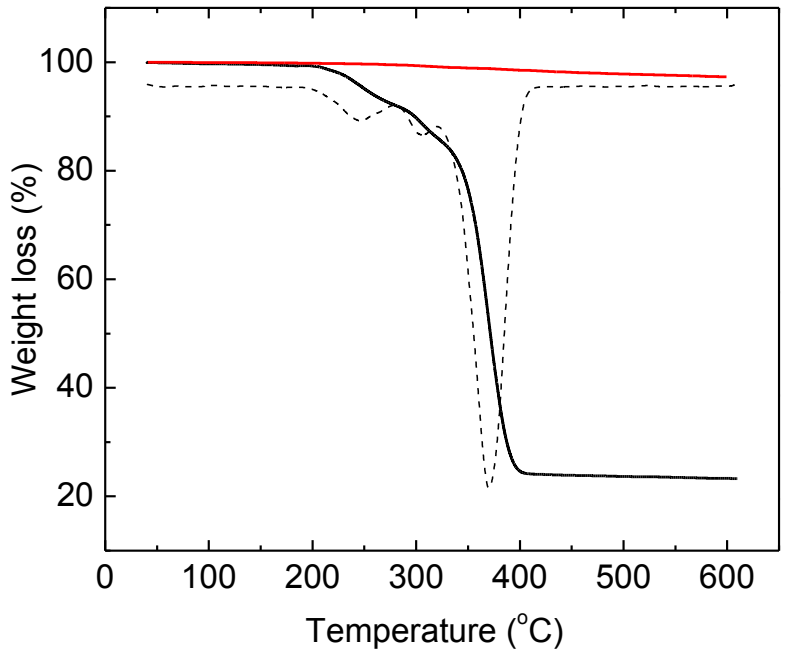

Figure 15. TGA profile for (a): as-prepared containing surfactant (black line) and mesoporous (red line) Cu/G NPAs recorded under N_2 flow (~200 mL min^{-1}). The differential thermogravimetric (DTG) curve (dashed line) for as-prepared materials is also given.

Characterization of the as-prepared Cu/G NPAs by thermogravimetric analysis (TGA) under nitrogen showed no appreciable weight loss up to 600 ^{o}C, consisting with the elimination of the polymer template (Figure 15). In contrast, the uncalcinated sample revealed a weight loss of ~80% in the temperature range 250–440 ^{o}C, which is attributed to the decomposition of surfactant. In order to find the carbon content remaining in the porous material, it was performed TGA by heating

the Cu/G NPAs sample to 900 ^{o}C under an air atmosphere (Figure 16). After completion of analysis, the inorganic residue was found to be crystalline CuO with a monoclinic structure (JCPDS No. 48-1548) (Figure 17), while any remnant carbon species would be fully oxidized to CO_2. From the difference of mass before and after calcination, it was derived a weight fraction of carbon ~12.5 wt.%. A similar carbon content (ca. 11.2 wt%) was obtained by elemental C, H, N analysis.

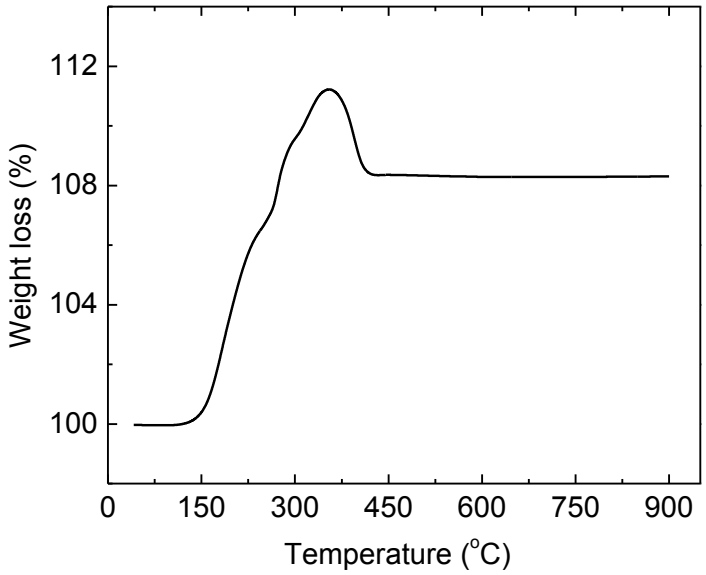

Figure 16. TGA profile for mesoporous Cu/G NPAs recorded under air flow (~200 mL min^{-1}).

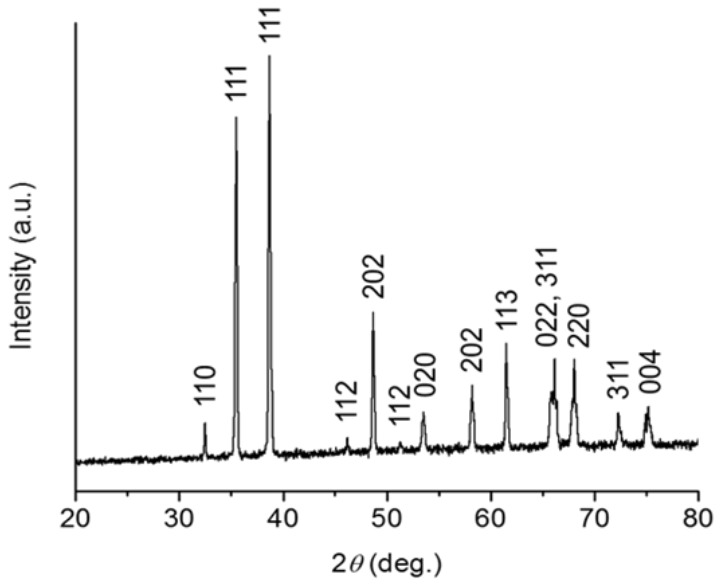

Figure 17. XRD pattern of the inorganic residue obtained after TGA analysis (up to 900 ^{o}C, in air).

The presence of acetate (CH_3COO^-) ligands in the surface of CuO nanoparticles was confirmed by Fourier transform Infrared (FT-IR) spectroscopy (Figure 18). The IR spectrum shows intense absorption peaks at 1108, 1632 and 2850–2980 cm^{-1}, which can be attributed to the stretching vibration bands of C–O, C=O and C–H bonds of the acetate ligand, respectively [123]. The broad absorption band in the range 3100–3600 cm^{-1} is assigned to the stretching vibration of hydroxyl groups of acetate and possibly adsorbed water. The absorption bands at 434, 519 and 595 cm^{-1} are attributed to the 2Bu modes and Au mode of CuO, respectively.

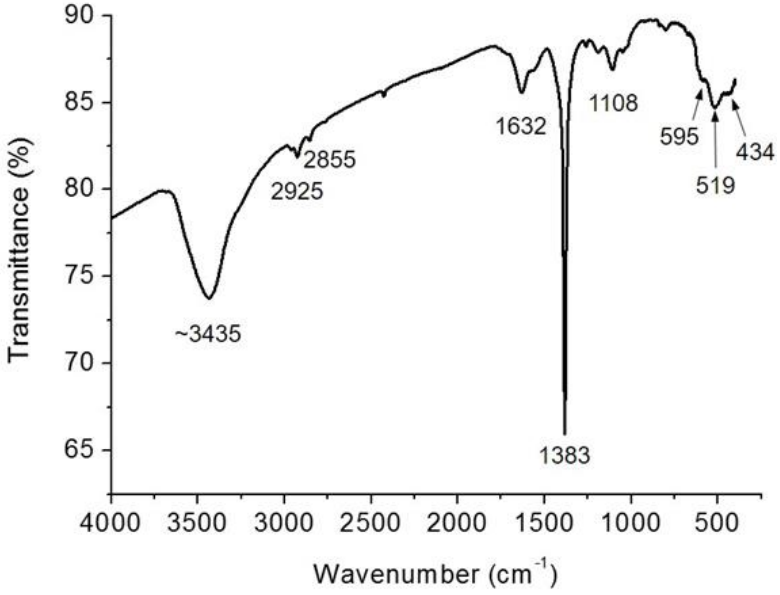

Figure 18. FT-IR spectrum of precursor CuO nanoparticles coated with the acetate ligand.

The morphology and porous structure of the Cu/G NPAs as well as CuO nanoparticles were investigated using X-ray diffraction (XRD), scanning electron microscopy (SEM), transmission electron microscopy (TEM) and N_2 physisorption. X-ray diffraction measurements indicated the phase purity and crystallinity of the as-prepared CuO nanoparticles (Figure 19a), as well as the complete conversion of CuO to Cu in Cu/G NPAs (Figure 19b). In the XRD pattern of the obtained nanoparticles all the diffraction peaks are consistent to the CuO phase with a monoclinic structure (JCPDS No. 48-1548), while in case of Cu/G NPAs it shows single-phase elemental Cu (JCPDS No. 85-1326), with no signs of

other crystalline phases. Further characterization of the CuO nanoparticles by TEM showed an average particle size of 4.9 ± 0.6 nm (Figure 20).

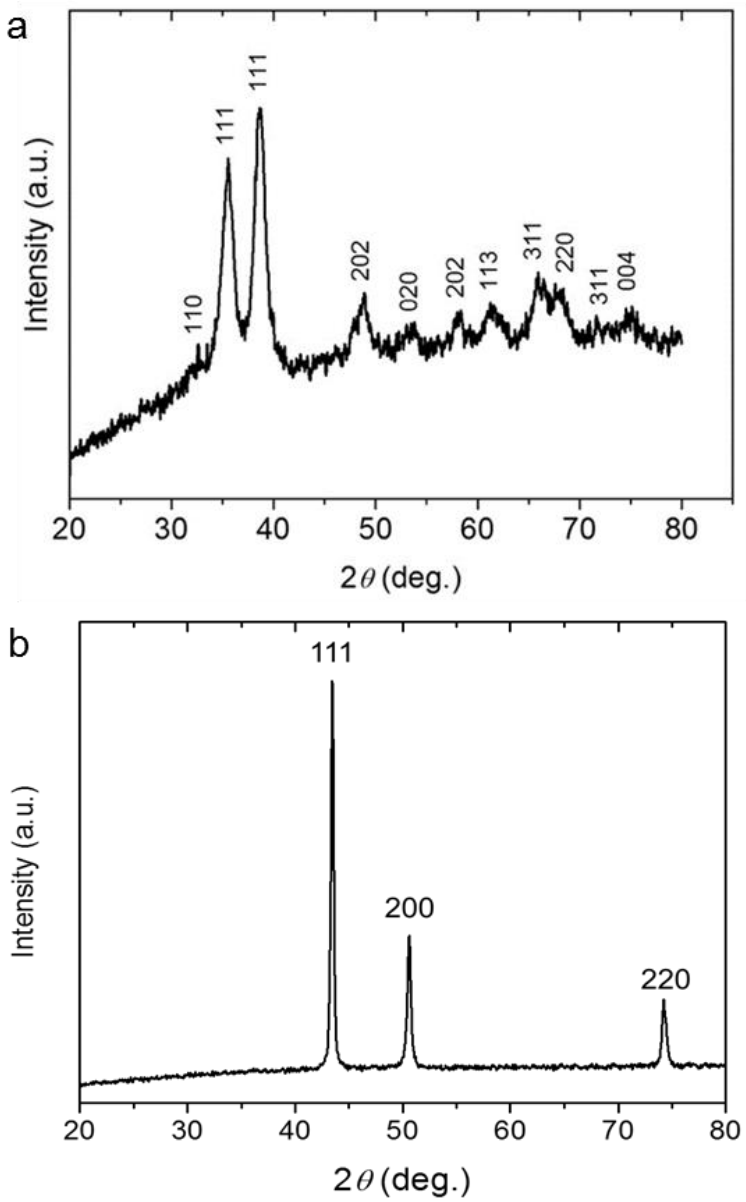

Figure 19. XRD pattern of (a) CuO nanoparticles and (b) Cu/G NPAs.

Field-emission (FE) SEM studies revealed that the resulting Cu/G NPAs material is composed of nanoparticles with roughly spherical morphology and size of about 100 nm (Figure 21). This particle size is fairly larger than the size of starting materials (Figure 20), indicating grain coarsening of CuO nanoparticles during synthesis. In particular, upon heating the CuO nanoparticles trapped by

BCPs are expected to reduce into Cu nanoparticles, which in turn can coalesce further into large particles. The growth of Cu nanoparticles is assumed to occur in the confined volume of the BCP aggregates *via* an Ostwald ripening process in which the small nanoparticles are consumed into larger nanoagglomerates in order to decrease the surface-to-volume ratio [124]. Interestingly, the as-prepared Cu/G nanoparticle assemblies form stable dispersions in nonpolar solvents, like toluene, chloroform and tetrahydrofuran, due to the large pore volume and hydrophobic nature of both copper and carbon components (inset of Figure 21).

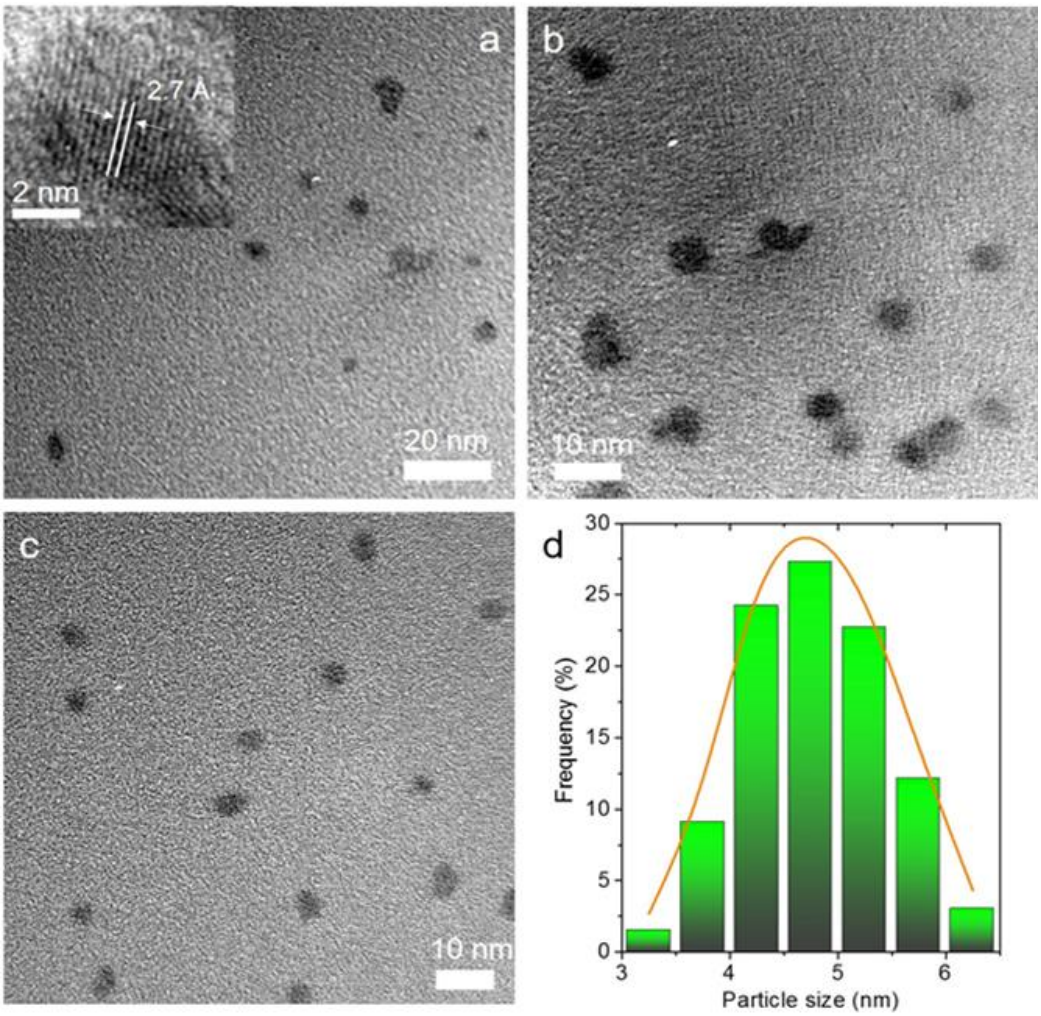

Figure 20. (a-c) Typical TEM images and (d) particle-size distribution histogram of the precursor (acetate-capped) CuO nanoparticles. The inset of pane (a) displays a high-resolution TEM image from an individual nanoparticle, showing the lattice fringes of the (110) crystal planes of monoclinic CuO (JCPDS No. 48-1548).

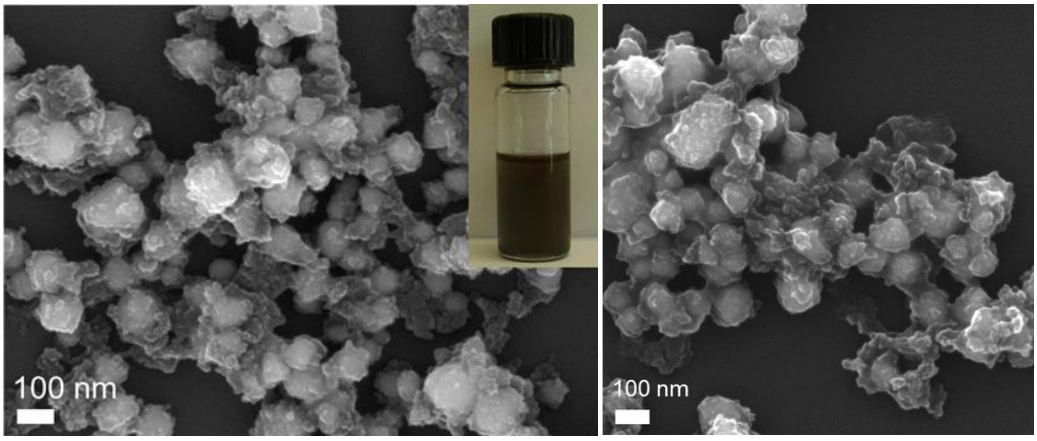

Figure 21. FE-SEM images of the Cu/G NPAs. The inset of the panel shows suspension of the Cu/G assemblies in toluene (0.5 mg/mL).

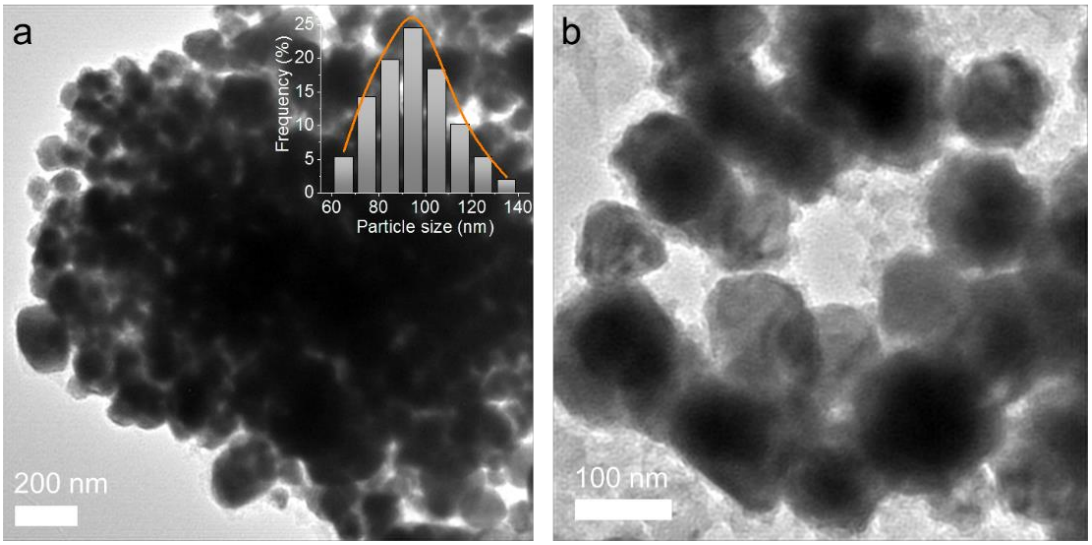

Figure 22. (a,b) Typical TEM images of the Cu/G NPAs. Inset of panel (a): particle-size distribution histogram showing an average size of 94.2 ± 14.6 nm.

TEM characterization of the Cu/G NPAs sample showed a network structure consisting of connected Cu nanoparticles with an average particle size of 94 nm (Figures 22a and b), which is in agreement with that observed from SEM. Close inspection of a constituent nanoparticles with high-resolution TEM (HRTEM) reveals distinct lattice fringes with a 2.1 Å interplanar spacing that corresponds to the (111) planes of the face-centered cubic (fcc) Cu (Figure 23), in agreement with XRD results. Besides, the HRTEM image displays a graphitic network with

replication of the morphology of nanoparticle assemblies. Figure 23 also shows layers of short-range order aligning parallel to each other with an interlayer spacing of about 3.4 Å, which is a typical distance for graphite structure.

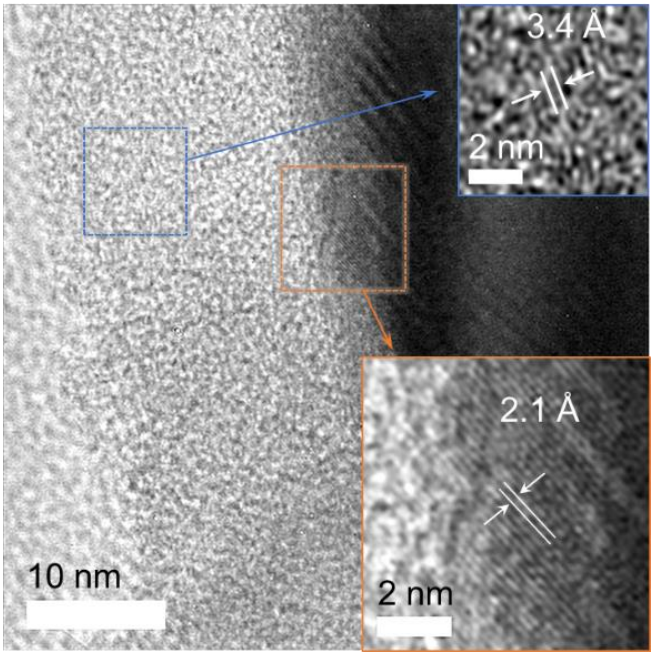

Figure 23. High-resolution TEM image of a constituent nanoparticle. Inset: High magnification HRTEM image of the areas marked by the dashed rectangles, showing flakes with a typical interlayer distance of graphite (blue boxed region) and lattice fringes of the Cu (111) planes (orange boxed region).

The graphitization degree of the Cu/G NPAs material was also characterized by Raman spectroscopy, whereas the characteristic bands at ~1362 cm^{-1} (defect-related D band) and ~1594 cm^{-1} (in-plane G band) for carbon materials can be readily seen (Figure 24). The first peak corresponds to the disordered carbon, while the latter peak is associated with the graphite-like morphology of carbon materials [125,126]. The intensity ratio of I_D to I_G in Raman spectrum is relatively low (I_D/I_G ~ 0.7) and resembles that of the less defective structures of reduced graphene oxide (rGO) and rGO/Cu composites [127,128]. The combined effect of planar graphene layers and nonplanar graphitic structure was also verified by the broad feature at ~2300–3200 cm^{-1}. Deconvolution of the Raman spectrum in this region showed three component peaks at 2756, 2962 and 3163 cm^{-1}, which can be assigned to the

two-photon Raman scattering process (2D band), and the C–H and C–OH stretching vibrations of graphite layers, respectively [129,130].

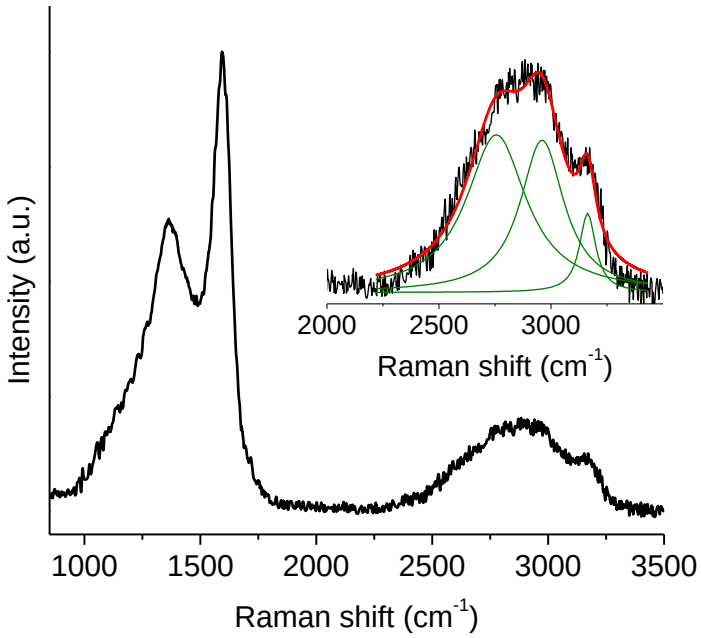

Figure 24. Raman spectrum for the Cu/G NPAs. Inset of panel: Lorentz fitting of the Raman data. The red line is fit to the data.

The conjunction of Cu nanoparticles with graphite layers leads to a significant increase in the UV–vis absorption in the visible-light region (Figure 25). The Cu/G NPAs shows a strong absorption peak at wavelength (λ) ~ 625 nm due to the localized surface plasmon resonance (LSPR) of Cu nanoparticles. The red shift in LSPR absorption of Cu/G NPAs material compared to that of isolated Cu nanoparticles with similar size (λ ~ 550–600 nm) [131] could be attributed to the strong interactions of Cu nanoparticles with the graphite layers. It was suggested that graphite structure may act as a lossy dielectric with high reflective index in the visible spectrum, which results in red-shift of the LSPR absorption [132], although the plasmon coupling between the neighboring Cu nanoparticles could be a possible explanation [133].

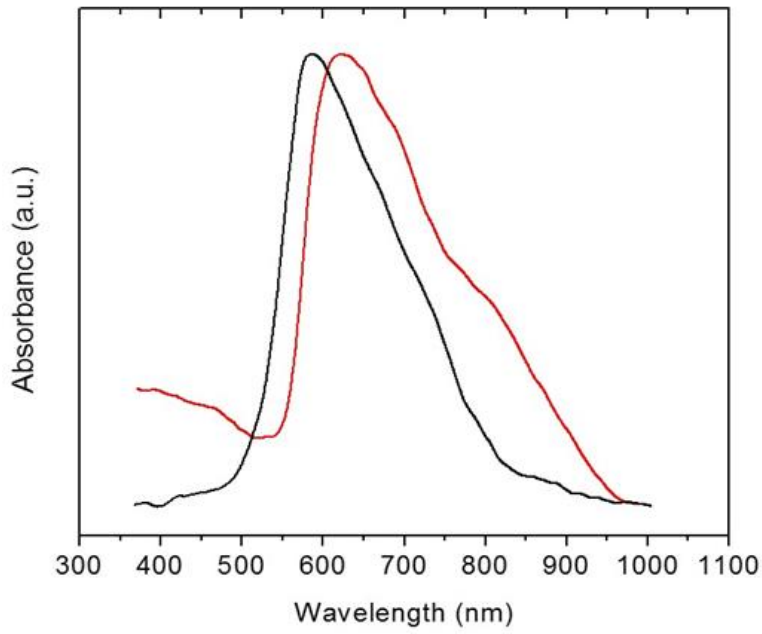

Figure 25. UV–vis absorption spectra of Cu/G NPAs (red line) and Cu nanoparticles (black line) suspensions in toluene (0.5 mg mL^{-1}).

Clear evidence for the open-pore structure of Cu/G NPAs was obtained by N_2 physisorption at –196 ºC. The sample exhibits typical type IV adsorption-desorption isotherms accompanied with a small H_3-type hysteresis loop at high relative pressures, characteristic of the mesoporous solids with interconnected slit-shaped pores (Figure 26). The specific surface area of Cu/G NPAs, which is deduced using the Brunauer–Emmett–Teller (BET) method, is 90 $m^2 g^{-1}$ and the total pore volume is 0.19 $cm^3 g^{-1}$. Notably, the surface area of Cu/G NPAs is among the highest found for carbon supported Cu nanoparticles surpassing the values of core-shell Cu@carbon nanowires (8 $m^2 g^{-1}$) [134], reduced graphene oxide (rGO) supported Cu nanoparticles (30 $m^2 g^{-1}$) [135] and graphene network supported core-shell Cu@G nanoparticles (79 $m^2 g^{-1}$) [136]. Density functional theory (DFT) analysis of the adsorption data reveals a quite narrow distribution of pore sizes with an average diameter of 4.3 nm (assuming slit-like pores), see inset of Figure 26. The N_2 physisorption isotherms together with TEM image shown on Figure 22a suggest that this pore size stems from interstitial voids formed between the assembled Cu nanoparticles. It is noteworthy that the polymer template plays a key role in the conformation growth of Cu/G assemblies – that is to direct the arrangement of CuO nanoparticles into mesoporous structures, promote the

reduction of CuO into Cu, and provide the carbon source appropriate for the formation of graphite network.

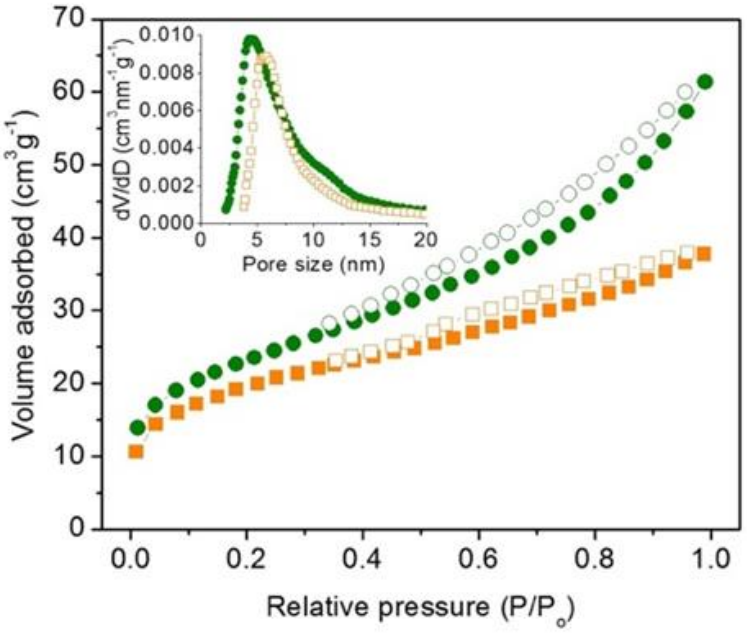

Figure 26. N_2 adsorption–desorption isotherms at –196 ºC and the corresponding DFT pore-size distribution plots (inset) of the PEG-*b*-PPG-*b*-PEG (circle symbols) and polyoxyethylene (100) stearyl ether POE-SE templated (square symbols) mesoporous Cu/G nanoparticle assemblies (Cu/G NPAs).

To evaluate the effect of organic polymer acting on the porous structure, Cu/G assemblies were successfully prepared with a different template and then were characterized by N_2 physisorption. It was found that after templating with polyoxyethylene (100) stearyl ether (POE-SE, $M_n \approx 4670$ g mol^{-1}), the size of interstitial voids between nanoparticle assemblies can be increased to 5.9 nm (Figure 26, inset). That larger mesostructure is interpreted to arise from the large POE hydrophilic block of the POE-SE polymer. Both POE-SE and PEG-*b*-PPG-*b*-PEG templates have similar total molecular weights, but feature very different hydrophilic/hydrophobic weight ratios (17.5 and 0.4, respectively). On the contrary, thermal processing of the CuO nanoparticles in absence of template gives a mixture of Cu_2O and CuO microparticles as it can be deduced from the XRD pattern in Figure 27a, where all the diffraction peaks can be assigned to the

monoclinic phase of CuO (JCPDS No. 48-1548) and cubic phase of Cu_2O (JCPDS No. 65-3288). Notably, analysis of the N_2 absorption data of this sample indicates almost negligible porosity, with a BET surface area of ~14 m^2 g^{-1} and a total pore volume of ~0.02 cm^3 g^{-1} (Figure 27b).

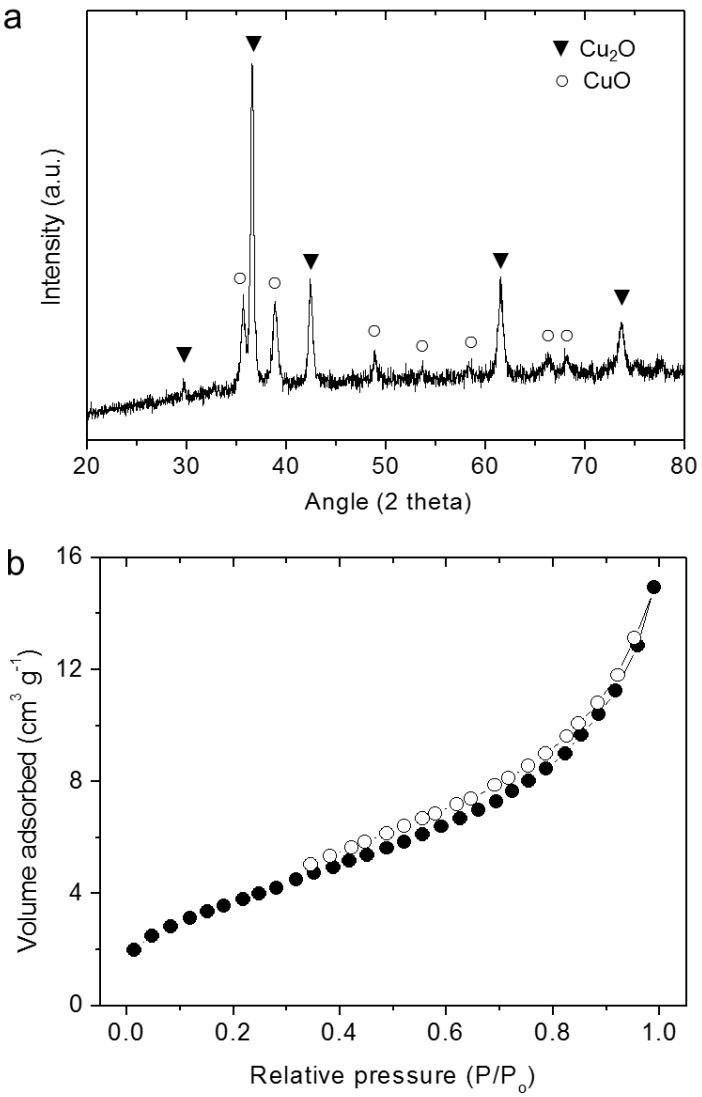

Figure 27. (a) Powder XRD pattern and (b) N_2 adsorption-desorption isotherms for the non-templated CuO_x material obtained after calcination in nitrogen at 350 ºC.

Additionally, when the gel product was thermally treated in air (350 ºC), only a black solid of CuO microparticles with almost none porosity was obtained (Figure 28). X-ray diffraction shows that all peaks can be assigned to the monoclinic structure of CuO (JCPDS No. 48-1548) and N_2 physisorption experiment indicates

a BET surface area of ~5 $m^2 g^{-1}$ and a total pore volume of ~0.01 $cm^3 g^{-1}$. All these control experiments together suggest explicitly that the pore structure in Cu/G assemblies is determined by the co-assembly of BCP and CuO nanoparticle components, while the organic polymer acts also as the reducing agent for the synthesis of Cu nanoparticles.

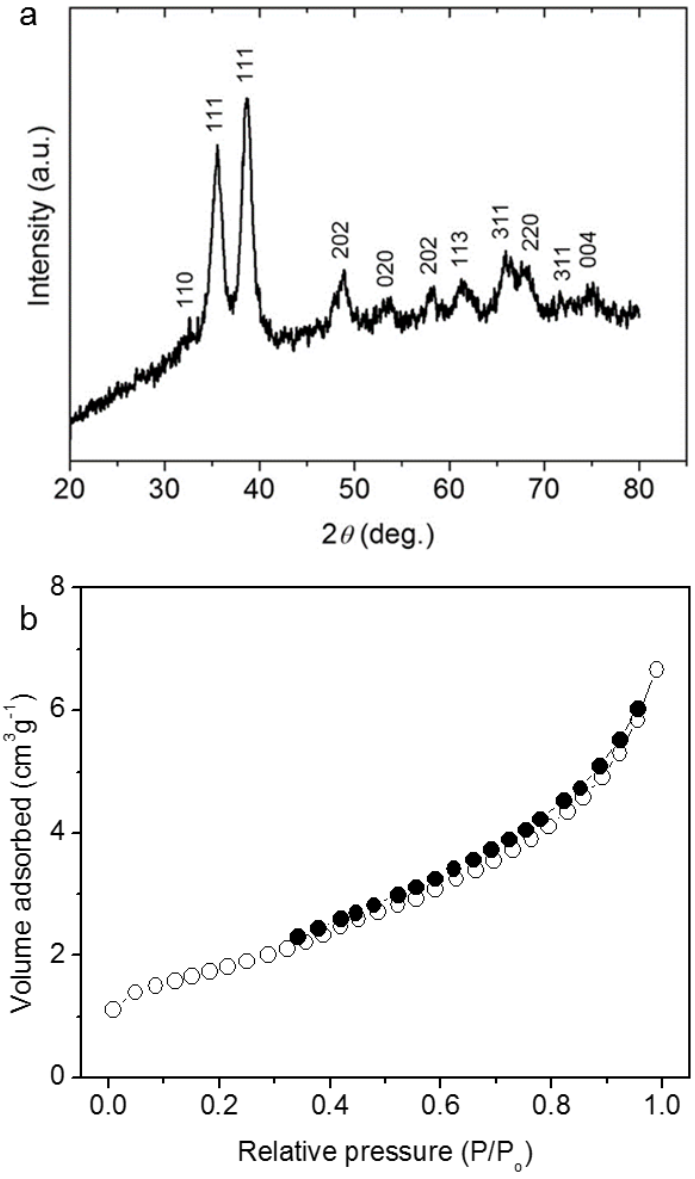

Figure 28. (a) Powder XRD pattern and (b) N_2 adsorption-desorption isotherms for the PEG-*b*-PPG-*b*-PEG-templated CuO material obtained after calcination in air at 350 °C.

3.2 SERS detection of analytes

The open pore structure and high interface area of Cu/G NPAs provide opportunities for chemical sensing. To this end, it was tested the Raman scattering capability of the Cu/G NPAs with R6G as a model analyte. Surface-enhanced Raman scattering (SERS), as stated before, is a powerful analytical technique for detecting trace amounts of analytes through their vibrational signals [137,138,139,140]. Intrinsically, metallic nanoparticles with strong surface-plasmon resonance in the visible and near-IR region of the electromagnetic spectrum, such as the Cu nanoparticles, are effective for SERS applications. As such, the materials described here are expected to function as SERS sensors because the interstitial voids between the nanoparticles can provide a large number of plasmonic hot spots, whereas the interfacial interactions between Cu nanoparticles and graphite layers can potentially result in a remarkable amplification of the electromagnetic field around the Cu nanoparticles [141,142].

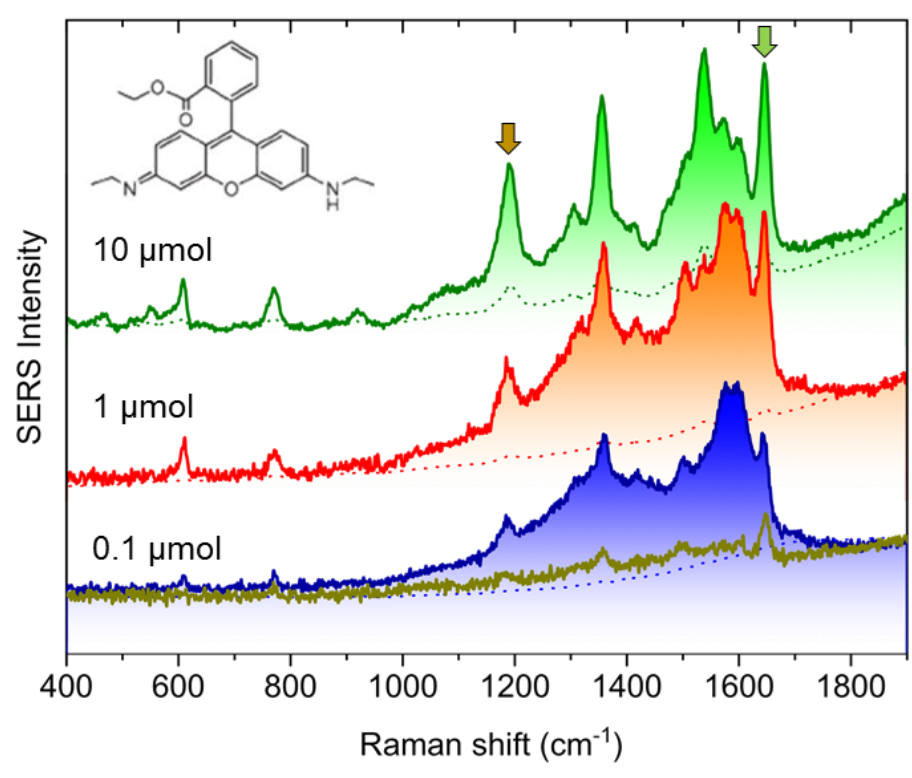

Figure 29. SERS spectra of a dilution series of R6G deposited to the Cu/G NPAs (solid lines) and aluminum (dot lines) substrates. The SERS spectrum of 0.1 µmol R6G deposited on the Cu nanoparticles substrate (dark yellow line). The arrows point to the 1186 cm^{-1} and 1644 cm^{-1} SERS peak positions of R6G.

SERS measurements clearly indicated that Cu/G NPAs are able to detect R6G in ethanol at concentrations ranging from 0.1 to 10 μmol (Figures 29 and 30). All the SERS spectra exhibited the characteristic shifts of R6G, that is, the in-plane and out-of-plane C–C–C bending (612 and 771 cm^{-1}, respectively), in-plane C–H bending (1132 cm^{-1}) and aromatic C–C stretching (1186, 1360, 1511, and 1644 cm^{-1}) modes. By comparing the SERS tests of R6G deposited on Cu/G NPAs and aluminum substrates at the same concentrations of R6G, we can see that Cu/G assemblies show a dramatic increase of the pristine Raman signals. Impressively, under identical conditions with 0.1 μmol R6G, although the R6G sample did not exhibit any observable Raman signal (Figure 29), the Cu/G NPAs substrate demonstrated strong characteristic lines, which is consistent with an enhancement factor (EF) of about 3.9×10^6, based on the intensity of the 1186 cm^{-1} Raman peak. At this concentration, an average of approximately 2 dye molecules are bound per one nm^2 of Cu nanoparticles, assuming that all R6G molecules were homogeneously absorbed on the nanoparticles surface. The enhancement factor for Cu/G NPAs substrate was calculated according to the following equation:

$$EF = \frac{I_{SERS}/N_{SERS}}{I_{RS}/N_{RS}} \quad (2)$$

where I_{SERS} and I_{RS} are the peak intensities (at 1186 cm^{-1} Raman shift) in SERS and normal Raman (on an aluminum substrate) spectra, respectively, and N_{SERS} and N_{RS} are the number of R6G analyte molecules on the Cu/G NPAs and aluminum substrates within the laser spot, respectively.

The number of R6G molecules deposited on the surface of aluminum substrate (N_{RS}) was calculated by the Eq. (3). In our calculations, we assume that R6G molecules are uniformly dispersed on the surface of the aluminum and porous Cu/G NPAs substrates.

$$N_{RS} = C_{R6G}\times N_A/SA_s \quad (3)$$

where C_{R6G} is the amount of analyte molecules (moles), N_A is the Avogadro number (6.022×10^{23}) and SA_s is the area of the support (10^{14} nm^2). N_{SERS} was calculated by dividing the number of adsorbed R6G molecules on the porous Cu/G

NPAs substrate ($C_{R6G} \times N_A$) by the surface area (SA_p) of the Cu/G NPAs material (5 mg × (90 $m^2/g \times 10^{18}$ $nm^2/m^2 \times 10^{-3}$ g/mg) = 4.5×10^{17} nm^2) or Cu nanoparticles ($N_{Cu} \times 4\pi(D_{NP}/2)^2$ nm^2, where N_{Cu} and D_{NP} are the number and diameter (100 nm) of Cu nanoparticles deposited on the substrate, respectively).

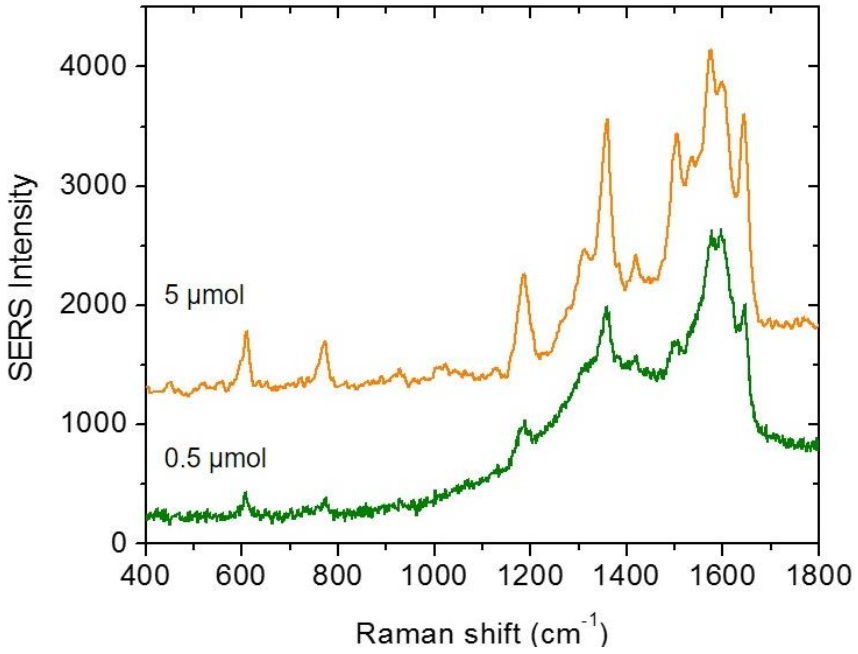

Figure 30. SERS spectra of 0.5 and 5 µmol dilutions of R6G deposited on the Cu/G NPAs substrate. For clarity, the SERS spectrum with 5 µmol concentration of R6G is offset by 1000 units.

For comparison, we also prepared thin films of Cu nanoparticles and graphite flakes and investigated their SERS activity. At a 0.1 µmol concentration of R6G, the Cu nanoparticles substrate exhibited weak but resolved Raman peaks (Figure 29), corresponding to an EF of about 9.3×10^4, which is 42 times lower than that of Cu/G NPAs substrate. The SERS spectrum of graphite substrate, on the other hand, showed only the characteristic D and G bands of graphitic sample (Figure 31). This comparative study signifies the synergistic effect of Cu nanoparticles and graphite layers in enhancing SERS efficiency. It is believed that a strong interaction between plasmonic Cu nanoparticles and the graphite layers occur, which may facilitate the binding of target molecules and charge transfer effect at the molecule-

Cu/G interfaces (chemical enhancement) [143,144], thereby increasing the SERS signal.

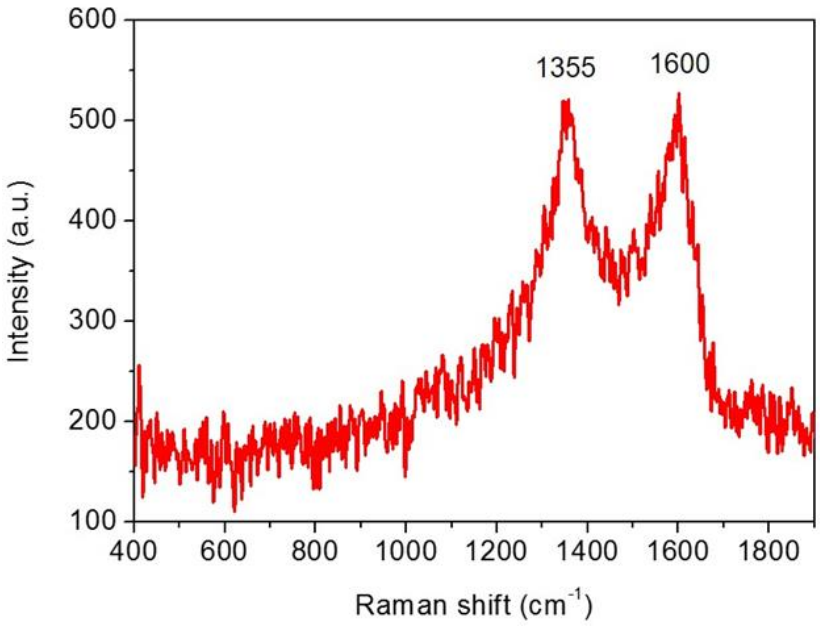

Figure 31. SERS spectrum of 0.1 μmol dilution of R6G deposited on the graphite substrate.

Furthermore, besides the enhancement in SERS signal by Cu/G NPAs substrate, the estimation of relative concentration of analytes in solution is another interesting issue. As shown in Figure 32, the intensities of the 1186 cm^{-1} and 1644 cm^{-1} vibration bands of R6G correlated very well with the logarithm of R6G amount dissolved in solution. To examine the feasibility of the Cu/G NPAs sensor for wide-range analyte detection, aniline was also tested. In Figure 33, the compared Raman spectra of 0.1 μmol aniline on Cu/G NPAs and aluminum substrates are shown. Similar to R6G, for this analyte the signal-to-noise ratio and sensitivity are also good (EF ~ 1.4×10^5), indicating the versatility of the sensor.

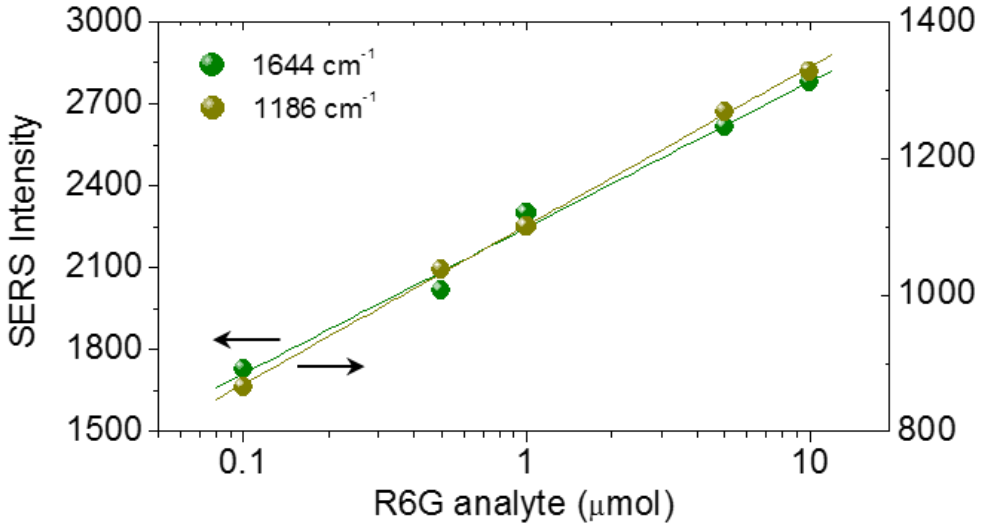

Figure 32. Plot of the intensity of the SERS peaks at 1186 and 1644 cm^{-1} as a function of R6G concentration over Cu/G NPAs substrate.

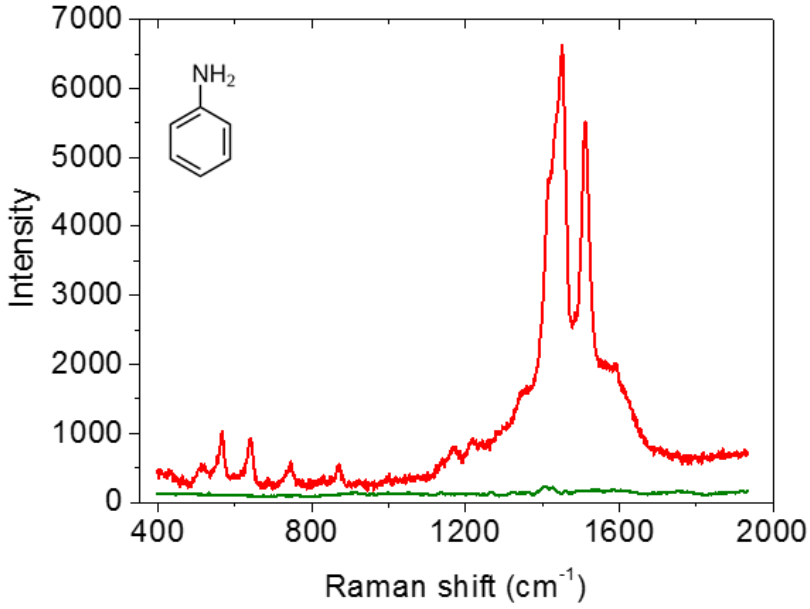

Figure 33. SERS spectrum of 0.1 μmol aniline deposited on the Cu/G NPAs (red line) and aluminum (green line) substrates.

A remarkable feature of the Cu/G NPAs substrate is the ability to detect analytes in a reliable way across the whole structure. To test this possibility, SERS analysis of R6G with a concertation of 0.1 μmol was carried out on different areas of the same substrate. The SERS signals indicated no significant fluctuations (less than ±8%) in the intensity of the Raman peaks (from 809 to 867 at 1186 cm^{-1} and from

1617 to 1743 at 1644 cm^{-1}, see Figure 34), and eventually the vibration bands of R6G analyte resulted in almost equal enhancement, i.e. 838±21 at 1186 cm^{-1} and 1688±45 at 1644 cm^{-1}, revealing high reproducibility.

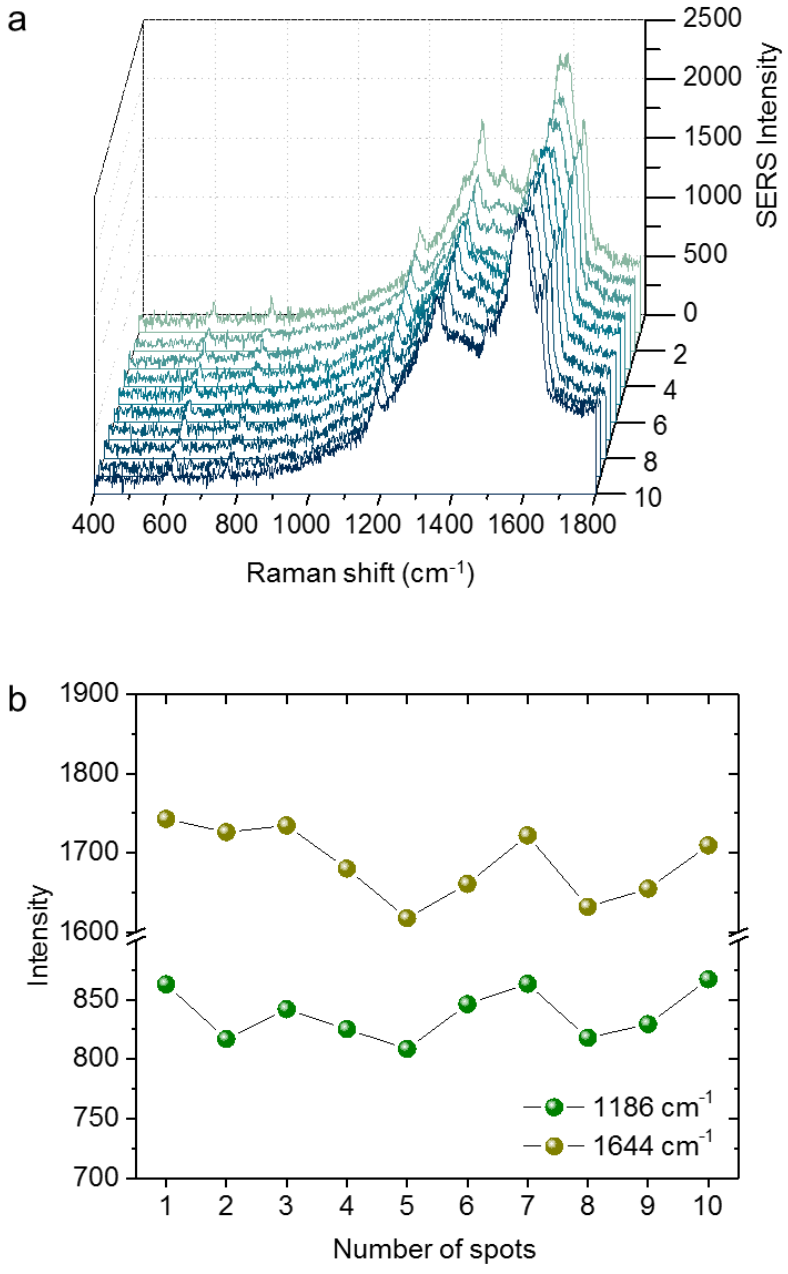

Figure 34. (a) SERS spectra of R6G with concentration of 0.1 μmol acquired on different spots of the Cu/G NPAs substrate. (b) Plot of the intensity of the 1186 and 1644 cm^{-1} peaks measured in ten (10) different areas of the R6G-loaded Cu/G NPAs substrate.

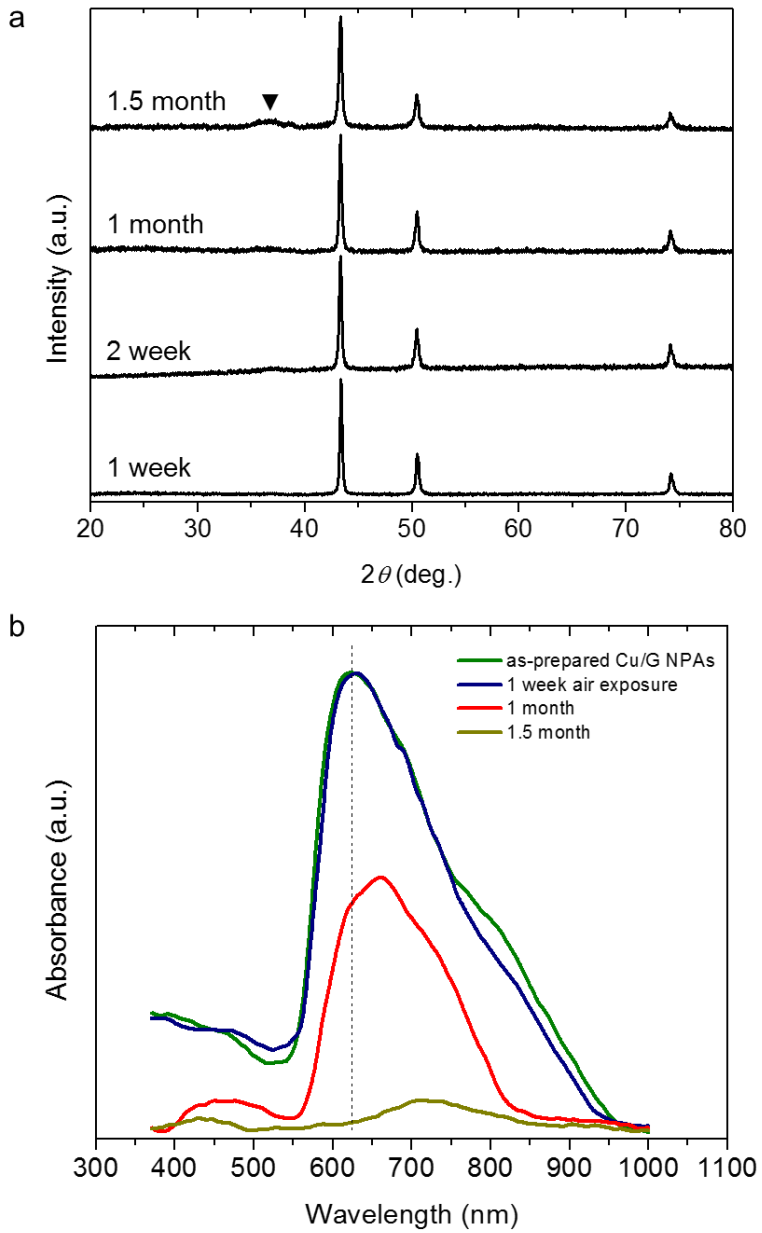

Figure 35. (a) XRD patterns and (b) UV–vis absorption spectra of partial oxidized Cu/G NPAs substrates upon exposure to air for different periods. In pane (b), the UV-vis absorption spectrum of as-prepared Cu/G NPAs is also given for comparison.

Besides the enhancement in SERS activity, Cu/G nanoparticle assemblies exhibited also sufficient resistance to oxidation, which is another important issue for their real-life application. To check the chemical reactivity of the Cu/G NPAs, the substrate was exposed to air for different times and subsequent characterized by UV–vis and X-ray diffraction measurements. UV–vis spectroscopy is a sensitive technique to detect changes of the LSPR optical absorption of Cu

nanoparticles due to the oxidation. It was suggested that upon air exposure, even after a few minutes, the LSPR peak is immediately shifted to longer wavelengths due to the modification of the dielectric constant of the material (Cu_2O) surrounding the Cu nanoparticles [145]. Therefore, UV–vis analysis on Cu/G NPAs sample can probe the chemical environment of Cu nanoparticles even a very small amount of surface oxides is present. The results indicated no signs of formation of any copper oxides on Cu/G assemblies even after exposure to ambient air for one week (Figure 35). More importantly, there was no apparent change in the SERS spectrum of 0.1 μmol R6G-loaded Cu/G NPAs after the oxidation treatment (Figure 36), which is an indication of excellent chemical stability. The stability of the Cu/G NPAs can be attributed to the graphite layers that effectively protect the Cu nanoparticles from oxidation. Nevertheless, evidence for oxide species (Cu_2O) on the nanoparticles surface began to appear in Cu/G NPAs material after extended (~1 month) exposure to air, judging from the red-shift (from 625 nm to 655 nm) and low intensity of the LSPR absorption in UV–vis spectra and the weak features at ~36–37^o in XRD patterns (due to the (111) reflection of Cu_2O) (Figure 35). Under these oxidative conditions, the SERS signal of Cu/G NPAs decreases over time owing to the formation of surface Cu_2O species.

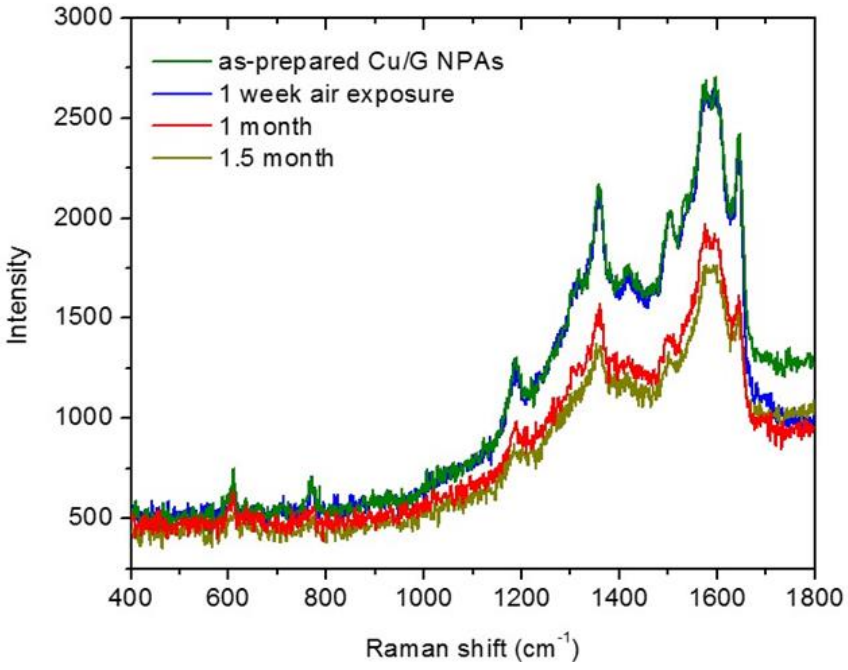

Figure 36. SERS spectra of R6G (0.1 μmol) on as-prepared and air-oxidized Cu/G NPAs samples.

Part II: Photocatalytic reduction of Cr(VI)

3.3 Morphology and structural characterization of h-CoO MNAs

Mesoporous assemblies of hexagonal CoO nanoparticles (denoted as h-CoO MNAs) were successfully prepared by a polymer-assisted aggregating self-assembly method. In a typical synthesis, a colloidal dispersion of BF_4^--stabilized h-CoO nanoparticles in *N*,*N*-dimethylformamide (DMF) was added slowly to a solution of poly(ethylene oxide)-*b*-poly(propylene oxide)-*b*-poly(ethylene oxide) (F127) block copolymer (BCP) (10 wt%) in tetrahydrofuran (THF). After a slow evaporation of the solvent (within ~5–6 days, at 40 °C) in order the CoO nanoparticles to co-assemble with the amphiphilic liquid-crystalline polymers, the mesostructured nanoparticle/BCP composites were formed. This intermediate product was then calcined at 350 °C for 4 h in nitrogen to give an extended network of interconnected h-CoO nanoparticles with accessible surface. The elimination of the polymer template was confirmed by thermogravimetric analysis (TGA) under nitrogen flow of the h-CoO/BCP sample before and after calcination (Figure 37).

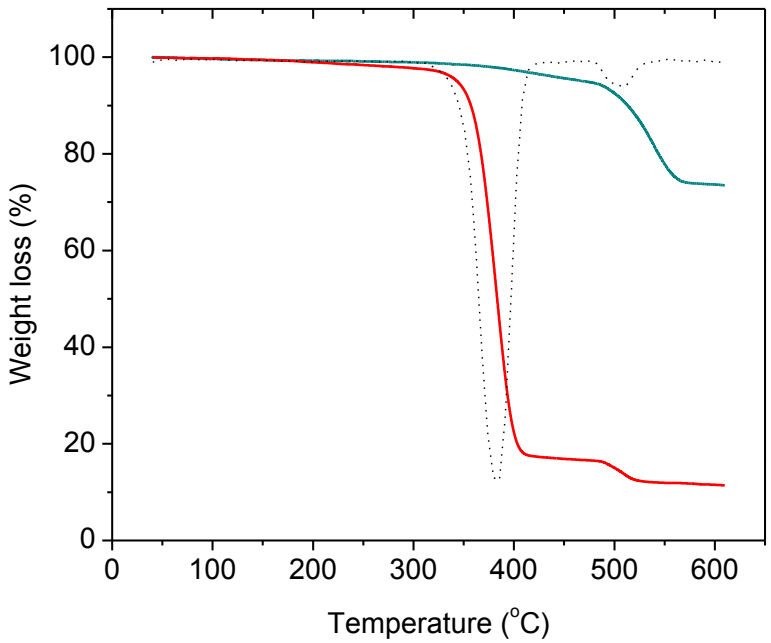

Figure 37. TGA profiles of as-prepared containing surfactant (red line) and mesoporous (green line) h-CoO MNAs recorded under N_2 flow (~200 mL min^{-1}). The differential thermogravimetric (DTG) curve (dashed line) for as-prepared materials is also given.

The TGA results of uncalcined h-CoO/BCP sample revealed a rapid weight loss of about 82% in the temperature range 280–440 °C, which is attributed to the decomposition of template. After template-removal, a weight loss less than 5% was observed at temperatures between 40 and 480 °C due to the dehydration and/or dehydroxylation of CoO surface, indicating that the polymer template is almost fully decomposed by 350 °C calcination. Also, in the range of 480–580 °C, a weight loss of about 23% was observed which is attributed to the reduction of CoO to Co under inert nitrogen atmosphere. X-ray diffraction measurement of the inorganic residue after TGA analysis indicated this conversion. As shown in Figure 38, all diffraction peaks could be indexed to the metallic Co with a face-centered cubic (fcc) (JCPDS No. 15-0806) and hexagonal close-packed (hcp) (JCPDS No. 05-0727) structure.

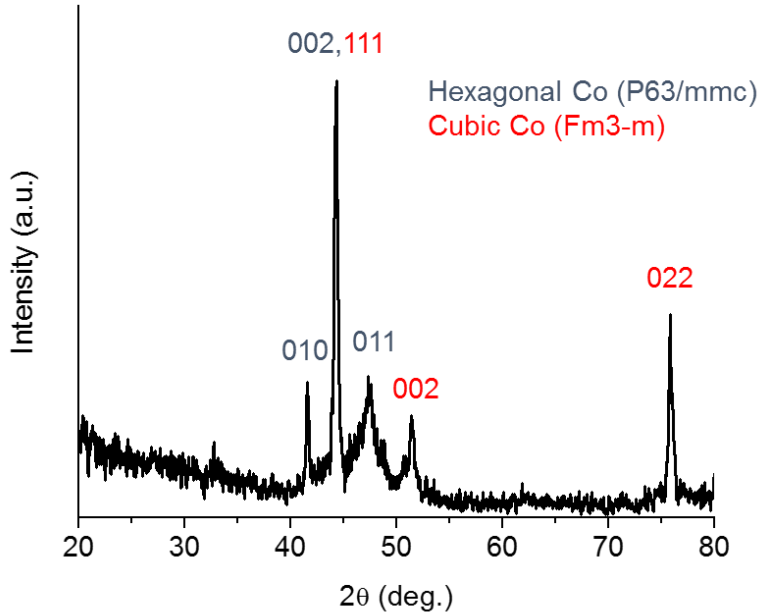

Figure 38. XRD pattern of the inorganic residue obtained from h-CoO/BCP composite after TGA analysis (up to 600 °C, in N_2).

The crystallinity and phase purity of the porous framework of h-CoO MNAs were confirmed with X-ray diffraction, and typical result is shown in Figure 39. The XRD pattern of template-free h-CoO MNAs suggests the formation of a hexagonal lattice structure with $P6_3mc$ symmetry, which is identical to that of the

precursor CoO nanoparticles (Figure 40). On the basis of the peak width of the (011) reflection and Scherrer's equation, the average domain size of the CoO crystallites in mesoporous h-CoO assemblies was estimated to be ~18 nm, which is slightly larger than that of the precursor nanoparticles (ca. 15 nm). This small increase is probably related to a low degree of interparticle fusion during the heating process.

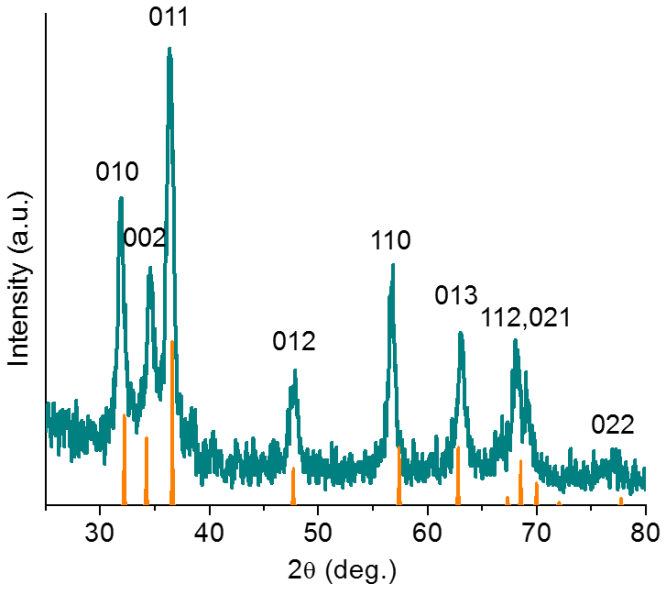

Figure 39. XRD pattern of h-CoO MNAs. The standard diffraction lines of hexagonal CoO (JCPDS No. 48-1719) are also given.

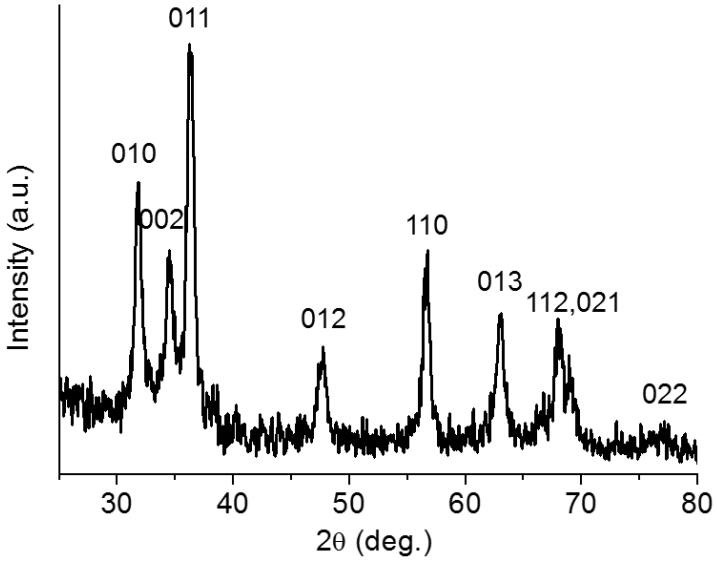

Figure 40. XRD pattern of BF_4^--capped CoO nanoparticles. All the diffraction peaks are consistent with the CoO phase with a hexagonal structure (JCPDS No. 48-1719). Scherrer analysis on the (011) peak showed an average crystallite size of 15 nm.

Typical transmission electron microscopy (TEM) images of the mesoporous h-CoO assemblies are shown in Figure 41. It appears that the structure of h-CoO MNAs is actually constructed solely by cross-linked nanoparticles with an average diameter of 18 ± 5 nm (based on a count of more than 100 individual nanoparticles, inset of Figure 41), in good agreement with XRD results. High-resolution TEM (HRTEM) characterization reveals that the constituent nanoparticles adopt a pyramid shape and exhibit single-crystal structure, displaying well-resolved lattice fringes throughout the particles, which, according to the fast Fourier transform (FFT) pattern, correspond to the (110) and (101) planes (along the [111] zone axis) of hexagonal CoO (Figure 42a). In addition, the HRTEM image in Figure 42a shows intergrowth between neighboring nanoparticles, suggesting the formation of a continuous cross-linked nanoparticle network. Creating a network structure of tightly connected nanoparticles is important for applications that require electronic connectivity and mechanical rigidity, such as catalysis, chemical sensing and energy conversion [146]. To further analyze the crystallinity of the constituent nanoparticles within the h-CoO MNAs sample, it was performed selected-area electron diffraction (SAED). In agreement with XRD and HRTEM results, the SAED pattern in Figure 42b demonstrates a random orientation of highly crystalline h-CoO nanoparticles into the pore walls, displaying a sequence of broad Debye–Scherrer diffraction rings which can be readily assigned to the hexagonal crystalline phase of CoO (JCPDS No. 48-1719).

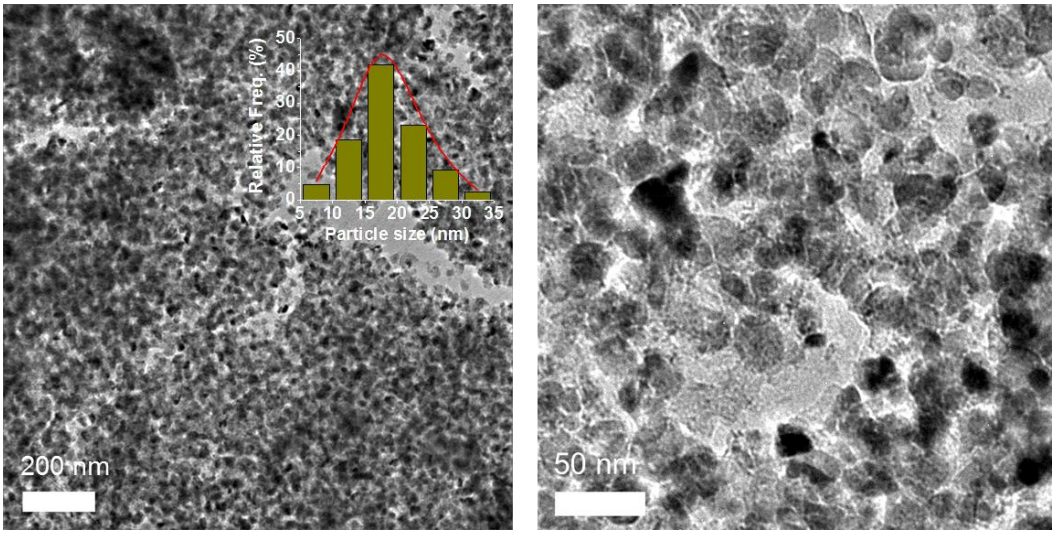

Figure 41. Typical TEM images (inset: particle size distribution plot showing an average diameter of 18 ± 5 nm) of h-CoO MNAs.

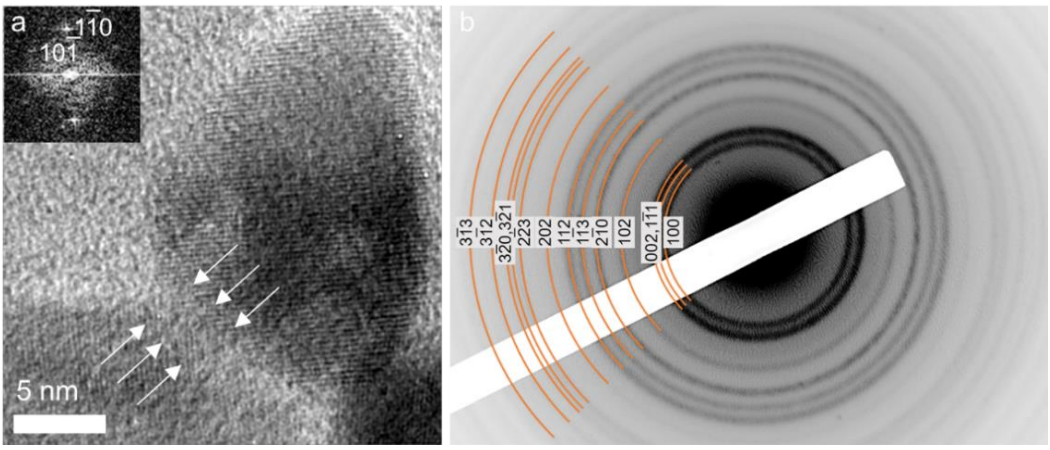

Figure 42. (a) High-Resolution TEM (inset: the corresponding FFT pattern) and (b) SEAD pattern for h-CoO MNAs. The arrows in panel (a) show linking area between adjacent nanoparticles.

Nitrogen physisorption measurements indicated the mesoporous nature of h-CoO nanoparticle assemblies. Figure 43 depicts typical adsorption-desorption isotherms and the corresponding pore size distribution plot for the h-CoO MNAs. The isotherms exhibit a type IV shape accompanied with a H_3 type hysteresis loop, suggesting mesoporous structure with slit-shaped pores. The delayed closure of the hysteresis loop could be associated with potential surface pore-blocking effects. The specific surface area and total pore volume of the h-CoO MNAs were measured to be 96 $m^2\ g^{-1}$, according to the Brunauer-Emmett-Teller (BET) method, and 0.14 $cm^3\ g^{-1}$, respectively. The pore size distribution plot, obtained from the adsorption branch of isotherms using the non-local density functional theory (NLDFT), shows a quite narrow size distribution with a pore diameter of about 4.8 nm (inset of Figure 43). Comparatively, random aggregates of h-CoO nanoparticles (h-CoO RNAs), which have been prepared by direct mixing of BF_4^--capped h-CoO nanoparticles in THF without template, possess a lower surface area of 74 $m^2\ g^{-1}$ and small interstitial voids (ca. 2.3 nm) among the h-CoO particles (Figure 43). These results clearly suggest that the F127 polymer plays an important role in synthesis of h-CoO MNAs by assisting the self-assembly of colloidal nanoparticles into open-pore structures. The X-ray diffraction measurement confirmed the hexagonal structure of h-CoO RNAs (JCPDS No. 48-1719), similar to the crystal structure of h-CoO MNAs (Figure 44).

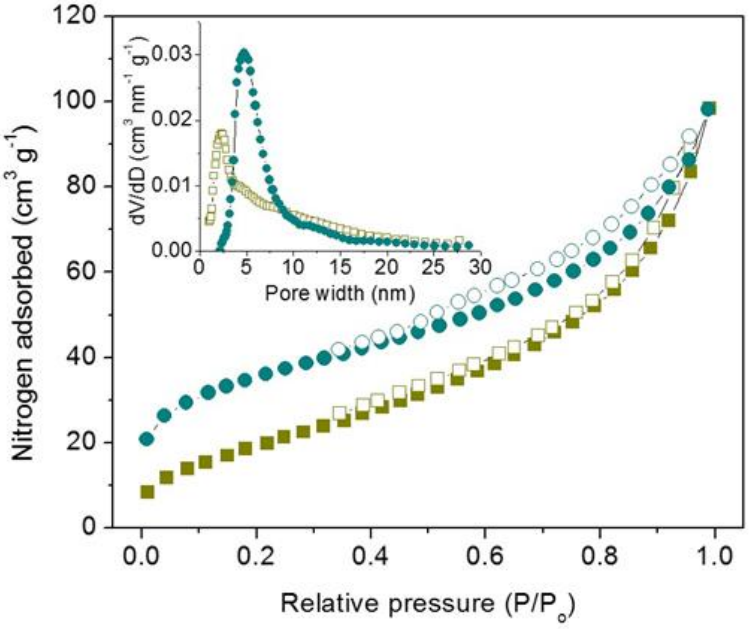

Figure 43. N_2 adsorption-desorption isotherms at –196 ºC and the corresponding NLDFT pore-size distributions of the h-CoO MNAs (circle symbols) and h-CoO RNAs (square symbols) materials. The N_2 isotherms of the h-CoO MNAs are offset by 10 cm^3 g^{-1} for clarity.

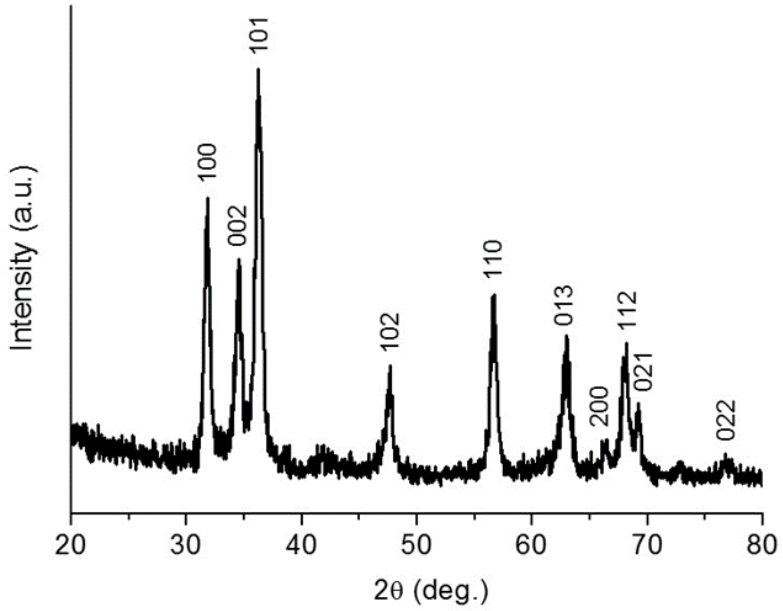

Figure 44. Powder XRD pattern of randomly aggregated h-CoO nanoparticles (h-CoO RNAs). All the diffraction peaks are consistent with the hexagonal structure of CoO (JCPDS No. 48-1719).

3.4 Photocatalytic study of h-CoO MNAs

The catalytic activity of as-prepared h-CoO mesoporous materials was initially evaluated in photocatalytic reduction of aqueous Cr(VI) under UV–visible light irradiation (λ > 360 nm). Firstly, the reaction conditions were optimized by measuring the Cr(VI) reduction rate for different loadings of the h-CoO MNAs catalyst (from 0.2 to 0.4 g L^{-1}). As it can be seen from Figure 45, with increasing catalyst addition, the reduction rate of Cr(VI) is increased until reaching a maximum at 0.3 g L^{-1}. The h-CoO MNAs concentration-dependent degradation rate of Cr(VI) can be explained by the enhancement of the light absorption by the catalyst's nanoparticles. However, as indicated in Figure 45, excess amount of catalyst (more than 0.4 g L^{-1}) may counter this effect, leading to a slight decrease in Cr(VI) reduction efficiency, presumably due to the light scattering effect from the particles surface [147]. Meanwhile, control experiments in the absence of the catalyst or light irradiation have been carried out to demonstrate the photocatalytic nature of the reactions and the results showed that the reduction of Cr(VI) does not take place under these conditions (Figure 45).

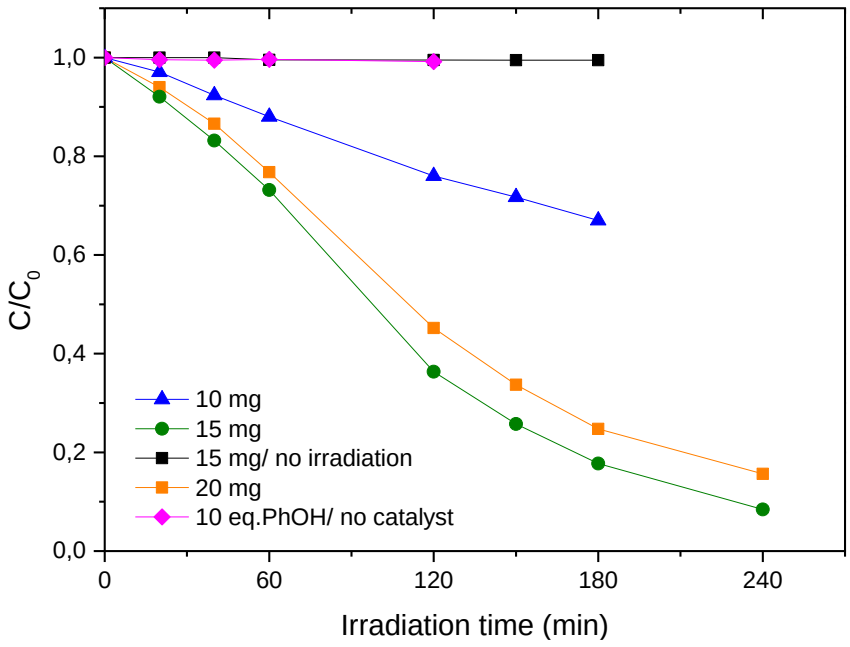

Figure 45. Time courses of photocatalytic reduction of Cr(VI) under different concentration of h-CoO MNAs catalyst. Reaction conditions: 0.2–0.4 g L^{-1} of h-CoO MNAs catalyst, 0.4 mg mL^{-1} of phenol (PhOH), 50 mg L^{-1} Cr(VI), 300-W Xe lamp (λ > 360 nm), pH = 2, 20 ºC.

The pH of the solution is another critical parameter that influences the photocatalytic reduction of Cr(VI) [148,149]. Figure 46 depicts that this process is favored for low pH values 1–2, while increasing to pH 4 no apparent Cr(VI) reduction (ca. 5% Cr(VI) reduction ratio) was observed after 3 h of irradiation. This is in line with previous studies mentioning that by raising pH of solution from 2 to 4 the conversion of Cr(VI) decreases [48]. It is well known that the predominating species of Cr(VI) at acid pH (pH = 1–2) is $HCrO_4^-$ (for Cr(VI) concentrations less than 1 g L^{-1}), which are gradually converted to CrO_4^{2-} by increasing pH [150]. Since the $HCrO_4^-$ oxyanions (E^o ($HCrO_4^-/Cr^{3+}$) = 0.86 V) are stronger oxidants than CrO_4^{2-} (E^o (CrO_4^{2-}/Cr_2O_3) = 0.56 V), the electron transfer process to these species is therefore favorable [151]. Note that all potentials reported in this work are referenced against the normal hydrogen electrode (NHE) at pH = 7. In addition, in such high acidic conditions the surface of the CoO catalyst is positively charged favoring the attraction of negatively charged $HCrO_4^-$ complexes (the point of zero charge (pzc) of CoO is reported to be ~ 9.2) [152], thus accelerating the photocatalytic reduction of Cr(VI) to Cr(III). In agreement with this assumption, at higher pH the surface is protonated in weaker range and repels chromate anions leading to a significant decrease in photocatalytic reduction rate of Cr(VI).

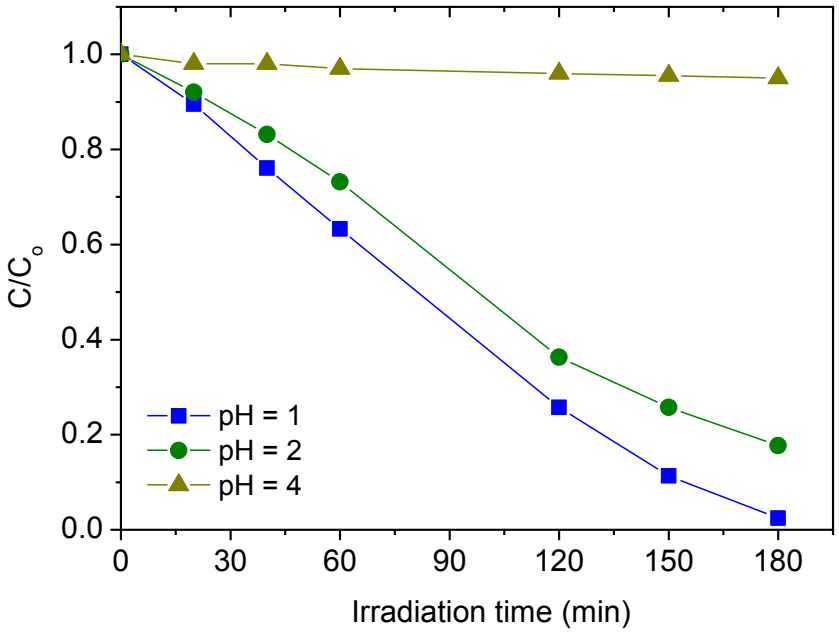

Figure 46. Time courses of photocatalytic reduction of Cr(VI) over h-CoO MNAs catalyst in pH 1–4. Reaction conditions: 0.3 g L^{-1} catalyst, 50 mg L^{-1} Cr(VI), 300-W Xe lamp (λ > 360 nm), pH = 1–4, 20 °C.

To study the visible light response of h-CoO MNAs catalyst, Cr(VI) photocatalytic reduction experiments were carried out under irradiation of $\lambda \geq 420$ nm light. As shown in Figure 47, under visible-light illumination, the photocatalytic reaction proceeds gradually and nearly 56% of the Cr(VI) is reduced in 4 h. In comparison, when UV–visible light ($\lambda > 360$ nm) was irradiated on h-CoO mesoporous, the conversion yield reaches 92% at the same period. Recent studies have shown the formation of hot (high-energy) carriers in colloidal semiconductor nanoparticles through above-gap excitation [153,154]. It was suggested that such a high photon-energy pump can facilitate the transfer process of photoinduced hot holes in semiconductors, competing interband charge-carrier transitions [155]. Similarly, the relatively higher efficiency of the h-CoO MNAs under UV–visible-light irradiation could be possibly attributed to the higher hole transfer yield as a result of the shorter wavelength excitation.

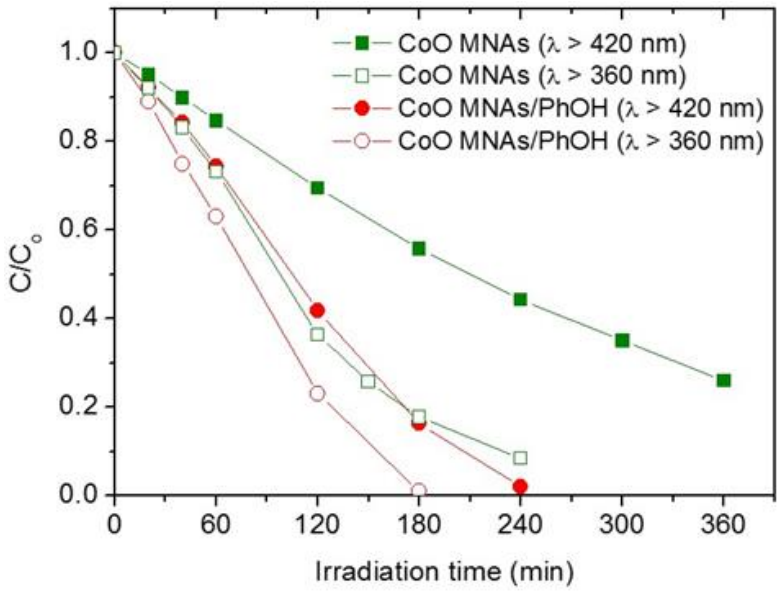

Figure 47. Photocatalytic reduction of aqueous Cr(VI) (50 mg L^{-1}) with h-CoO MNAs catalyst (0.3 g L^{-1}) in the absence and presence (0.4 mg mL^{-1}) of phenol (PhOH) under UV ($\lambda > 360$ nm) and visible ($\lambda \geq 420$ nm) light irradiation (pH = 2, 20 ^{o}C).

In line with this, the apparent quantum yield (AQY) of the Cr(VI) reduction, which is a key metric for the operational efficiency of a photocatalytic system, was estimated to be ~1.61% at λ = 375 nm and ~0.17% at λ = 440 nm, assuming all

incident photons were absorbed by the catalyst's nanoparticles. Of note, the efficiency of the h-CoO MNAs catalyst is among the highest reported values of semiconductor photocatalysts that perform Cr(VI) reduction without the combined use of sacrificial donors. For instance, Au/TiO_2-Pt nanocomposites showed a maximum AQY of 1.0% at 550 nm [156], $CuFe_2O_4$/CdS composites showed a 1.1% AQY at 430 nm [157] and Ba_2SnO_4 particles exhibited a 0.13% AQY [158] and $CuAl_2O_4$/TiO_2 heterostructure reached a AQY of 0.11% [159] under polychromatic light. It should be stressed that this photocatalytic activity was obtained by using single-component h-CoO catalyst.

To test the role of photogenerated electrons and holes in catalytic process, UV and visible light photocatalytic Cr(VI) reduction experiments were also carried out in the absence and presence of phenol as a sacrificial hole acceptor. The oxidation of phenol is thermodynamically (~0.96 V) [160] and kinetically more favourable than the oxidation of water (0.82 V), and thus often this process can accelerate the overall photocatalytic reaction [146,161]. The high concentration of phenol (10 equiv.) employed in the experiments ensures that the surface of h-CoO nanoparticles is saturated with excess of phenol. At these conditions, the reaction rate is not diffusion limited and therefore should be independent of phenol concentration, which means that the hole transfer across the solid/liquid interface is not a diffusion-controlled process of the overall photocatalytic reaction. Catalytic results shown in Figure 47 indicate that addition of 0.4 g L^{-1} of phenol into the Cr(VI) solution (50 ppm) leads to a considerable increase in the photocatalytic reduction rate under $\lambda \geq 420$ nm illumination, resulting in almost quantitatively (>99%) conversion of Cr(VI) at 4 h. It should be stressed that the detection limit of the analysis method is 5 μg L^{-1}. Comparatively, under identical conditions, when the h-CoO MNAs–Cr(VI)–phenol catalytic system was irradiated with UV–visible light, the Cr(VI) reduction reached a moderately higher rate than with visible light. For example, using $\lambda > 360$ nm light, the average reduction rate of $HCrO_4^-$ increased from 5.49 (with $\lambda \geq 420$ nm light) to 7.66 μmol h^{-1}. This different behavior could be tentatively related with the transfer rate of hot carriers generating from high photon-energy excitation. Such hot carriers may have little effect on the hole transfer process from h-CoO nanoparticles to phenol, but play a more prominent role in photooxidation of water. Unlike water, phenol seems to enable

efficient utilization of surface reaching holes (both hot and relaxed holes), leading to an improvement of the oxidation efficiency. This means that the high propensity for oxidation of phenol can diminish the differences in catalytic activity that may arise from the change in photon energy of the radiation and the overall reaction can readily proceed at a faster rate. Additionally, control experiment in the absence of the h-CoO MNAs was carried out to demonstrate the role of the catalyst in the oxidation of phenol. The results showed that when the Cr(VI)-phenol system was irradiated the reduction of Cr(VI) and oxidation of phenol does not take place (Figure 45). The conversion of phenol to diphenyl oxide, and thus its direct participation in the photocatalytic process as an electron donor, was confirmed by gas chromatography-mass spectroscopy (GC-MS, Shimadzu QP2010 Ultra) analysis of the reaction products (Figure 48).

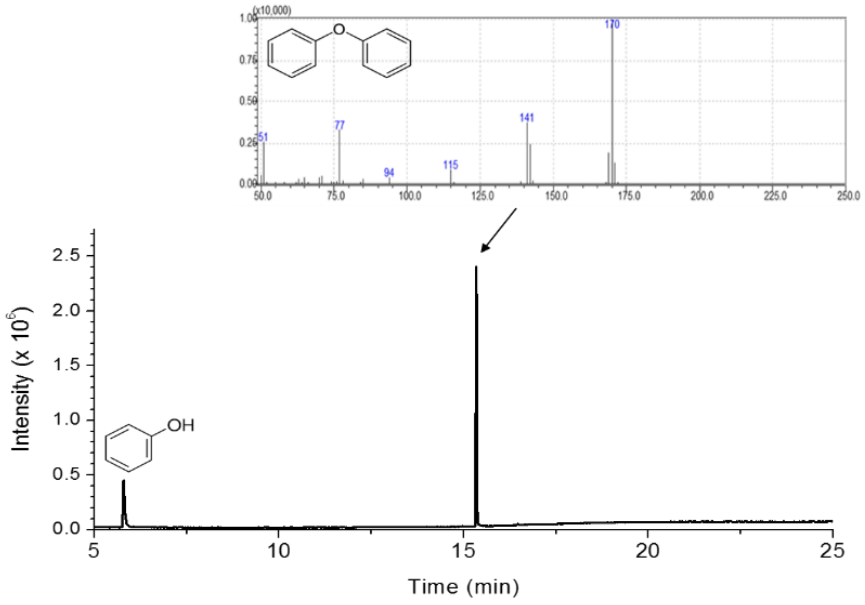

Figure 48. GC-MS profile of the ethyl acetate extract of the reaction mixture taken after 2 h of catalysis (0.3 g L^{-1} h-CoO MNAs catalyst, 50 mg L^{-1} Cr(VI), 10 equiv. phenol, 300-W Xe lamp ($\lambda > 360$ nm), pH = 2, 20 ^{o}C).

Taken together, it is obvious that photooxidation process by h-CoO surface holes is the reaction rate-controlled step in the h-CoO MNAs–Cr(VI) photocatalytic system. At this point, it should be noted that the synergistic degradation of organic pollutants such as phenol by Cr(VI) reduction is of vital importance for practical applications. Apart from chromium, groundwater contains also other pollutant

byproducts such as colorless organic chemicals and recalcitrant dyes [48], which their decontamination is a major concern [162,163]. This study clearly suggests that the photocatalytic reduction of Cr(VI) and oxidation of phenol are collaborative over mesoporous h-CoO nanoparticle assemblies and this process can enhance the photocatalytic reduction effect.

In addition to the oxidation kinetics at the h-CoO/solution interface, morphological effects may also contribute to the high photoactivity of h-CoO MNAs. This can be investigated by comparing photocatalytic data for Cr(VI) reduction by individual (BF_4^--capped) h-CoO nanoparticles and random aggregates of h-CoO nanoparticles (h-CoO RNAs). Results shown in Figure 49 indicate that these materials afforded a considerably lower catalytic performance than that obtained for Cr(VI) reduction at mesoporous h-CoO nanoparticle assemblies. Assuming that the reaction rate is proportional to the concentration of Cr(VI), the photocatalytic reaction can be investigated by the first-order kinetics of Langmuir-Hinshelwood model. Thus, the kinetic data obtained from analysis of the temporal evolution of Cr(VI) concentration using the first-order reaction rate (Eq. 4) reveal that the reaction proceeds at a lower rate over isolated h-CoO nanoparticles (k = 2.7×10^{-3} min^{-1}) and random aggregates h-CoO RNAs (k = 0.9×10^{-3} min^{-1}) than mesoporous h-CoO assemblies (k = 4.9×10^{-3} min^{-1}) under identical conditions (Figure 50).

$$\ln(C_o/C_t) = kt \quad (4)$$

where, C_o and C_t is the concentration of Cr(VI) at initial time and time t, respectively, and k is the apparent reaction rate constant.

Presumably, under the reaction conditions, the BF_4^- ligands anchored on the h-CoO nanoparticles surface are not sufficient to prevent agglomeration of the colloidal particles, and thus a deterioration of the catalytic performance was observed. On the other hand, the h-CoO RNAs although have an adequate surface area of 74 m^2 g^{-1} (Figure 43), contain a random distribution of small-sized pores between the nanoparticles that possible results in slow diffusion kinetics of Cr(VI) and/or C(III) ions. Therefore, from these results, it can be inferred that the material's surface area and pore volume play an important role in the reduction rate of Cr(VI).

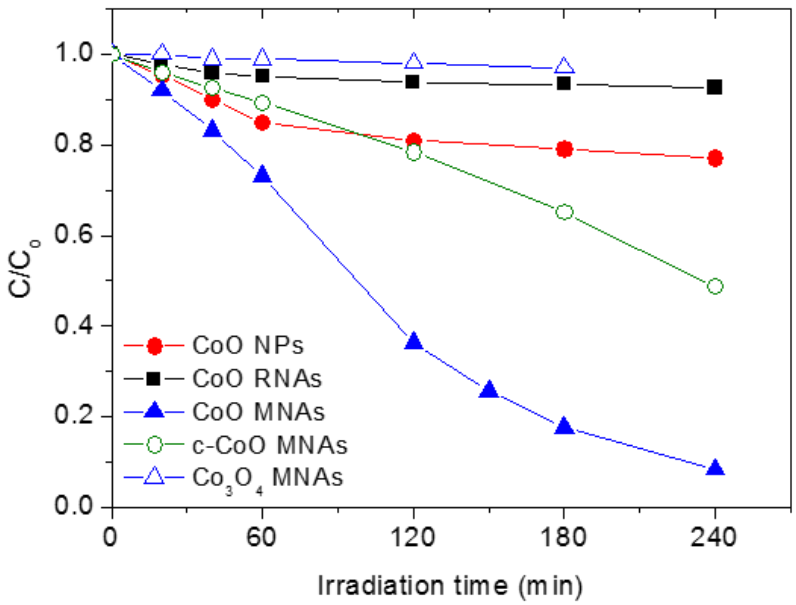

Figure 49. Photocatalytic reduction of Cr(VI) over different CoO-based photocatalysts. Reaction conditions: 0.3 g L^{-1} catalyst, 50 mg L^{-1} Cr(VI), 300-W Xe lamp ($\lambda > 360$ nm), pH = 2, 20 °C.

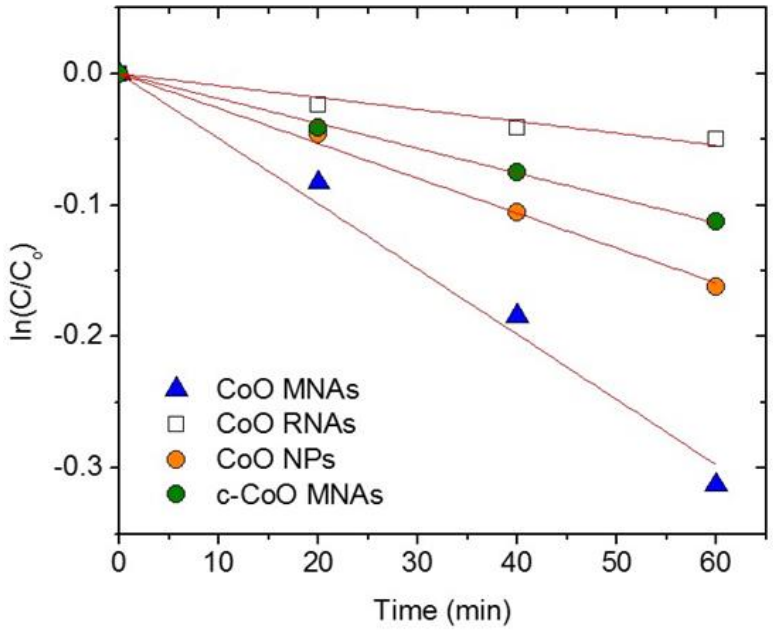

Figure 50. Kinetic profiles for UV–visible-light photocatalytic reduction of Cr(VI) over different CoO-based catalysts. The red lines are fit to the data.

Of particular note, mesoporous assemblies of cubic CoO nanoparticles (denoted as c-CoO MNAs), were also examined in Cr(VI) detoxification of water. c-CoO MNAs were obtained by polymer-templated self-assembly of cubic structured CoO

nanoparticles [107] and characterized by X-ray diffraction and nitrogen physisorption measurements (Figure 51). All the diffraction peaks in the XRD pattern can be assigned to the cubic phase of CoO (JCPDS No. 43-1004) as well as analysis of the N_2 absorption data indicates a BET surface area of ~134 $m^2 g^{-1}$, a total pore volume of ~0.15 $cm^3 g^{-1}$ and a pore diameter of 4.4 nm. Nevertheless, c-CoO MNAs showed a lower UV–visible-light Cr(VI) reduction activity (ca. 51% Cr(VI) reduction ratio at 4 h; $k = 1.9\times10^{-3}$ min^{-1}, see Figure 50) than the corresponding h-CoO MNAs catalyst with hexagonal phased CoO nanoparticles. This difference in activity may originate from the structural stability and the hole oxidation kinetics in CoO. As it has already mentioned, the crystal structure of cubic CoO (space group $Fm\bar{3}m$) is composed of CoO_6 octahedra, whereas that of hexagonal CoO (space group $P6_3mc$) contains tetrahedral CoO_4 units. The high stability and thus low reactivity of $Co^{\delta+}$–$O^{\delta-}$ bonds may be related to the higher crystal field stabilization energy (CFSE) of the high-spin d^7 Co(II) centers of cubic CoO, i.e. $-4/5\Delta_o$ *versus* $-6/5\Delta_t \approx -8/15\Delta_o$ for tetrahedral d^7 Co(II) ions. This means that although cubic CoO is a thermodynamically more stable phase than hexagonal CoO structure, it is less active for the generation of ·OH radicals by hole oxidation of surface-bound –OH groups or absorbed water molecules.

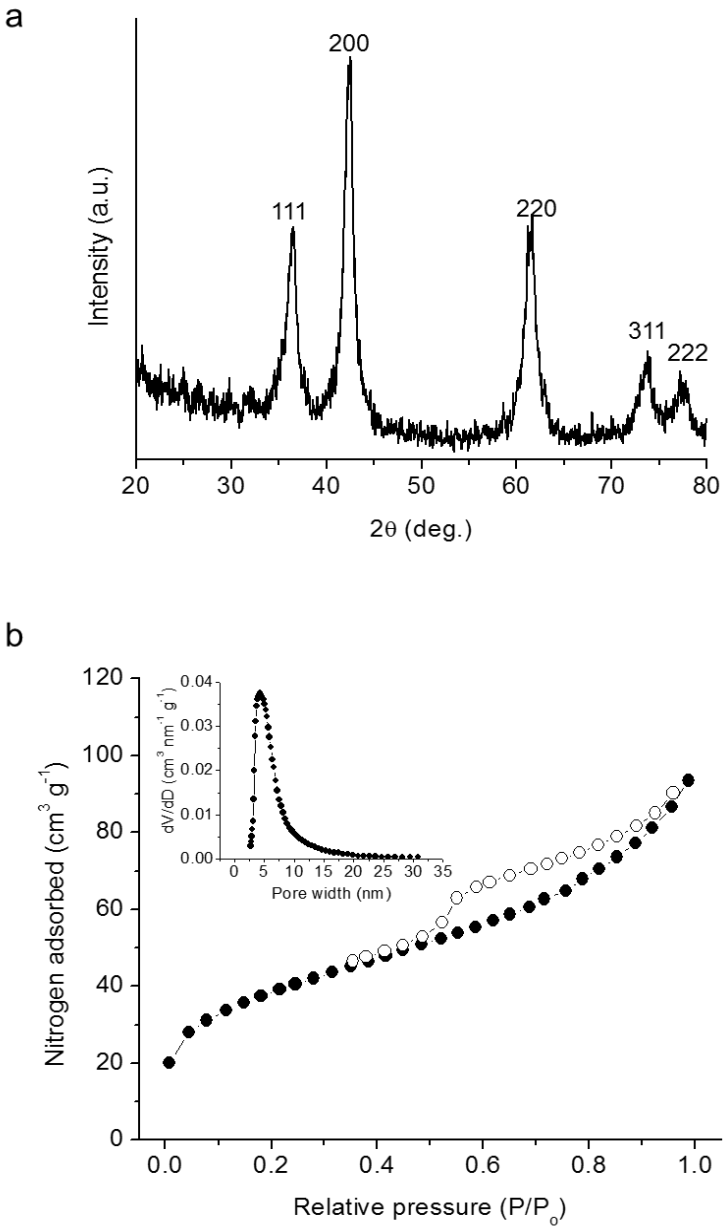

Figure 51. (a) Powder XRD pattern and (b) N_2 adsorption-desorption isotherms for the c-CoO MNAs catalyst. The diffraction peaks in the XRD pattern can be assigned to the cubic phase of CoO (JCPDS No. 43-1004).

The Cr(VI) reduction in water was also tested using mesoporous Co_3O_4 nanoparticle aggregates (Co_3O_4 MNAs), and a negligible UV–visible-light Cr(VI) reduction activity (~3% Cr(VI) reduction ratio) was detected, even after 3 h of illumination (Figure 49). This new material was obtained by annealing of the CoO nanoparticles/F127 composite in air at elevated temperature (350 ^oC). XRD pattern confirmed that the thermally converted sample is pure-phase cubic spinel structure

of Co_3O_4 (JCPDS No. 09-0418), while N_2 physisorption isotherms revealed an open porous structure with a BET surface area of 62 m^2 g^{-1} and a total pore volume of 0.15 cm^3 g^{-1} (Figure 52). These data clearly suggest that single-component Co_3O_4 is unsatisfactory catalyst for the simultaneous reduction of Cr(VI) and oxidation of water, although it has small grain size composition (ca. 12 nm based on Scherrer analysis) and large internal surface area, similar to those of h-CoO MNAs. Therefore, taken together, the catalytic results support that, apart from the surface area, the crystal phase of CoO plays a key role by promoting the oxidation half-reaction by the photoinduced holes and contributing to the high Cr(VI) reduction activity.

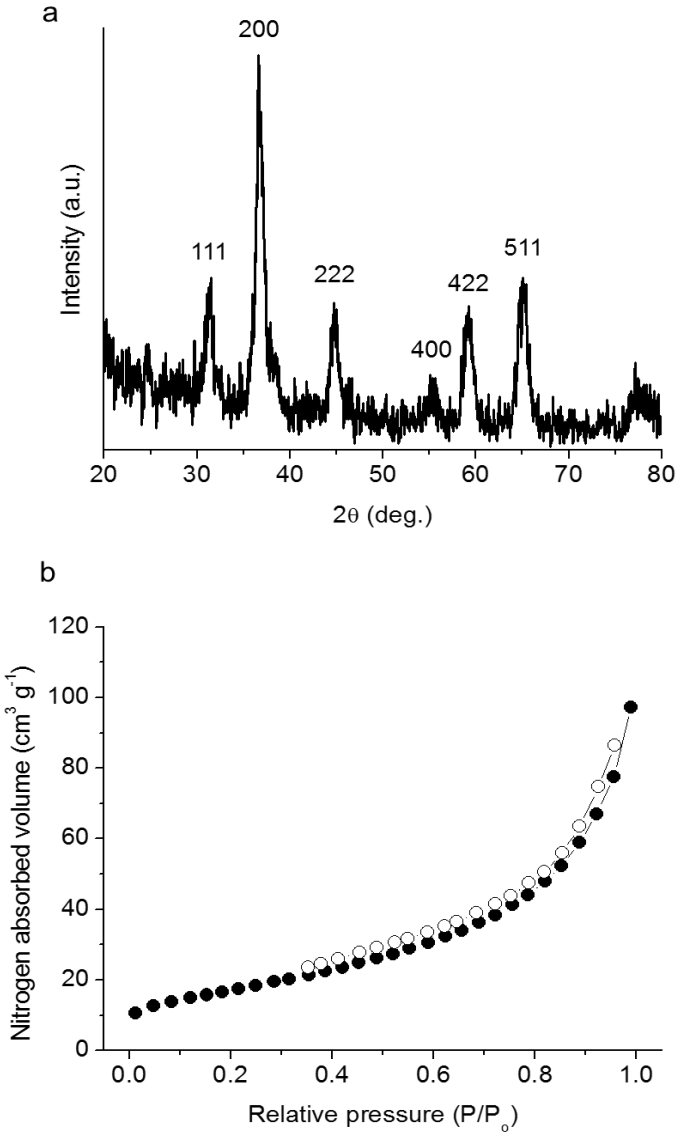

Figure 52. (a) Powder XRD pattern and (b) N_2 adsorption-desorption isotherms for the as-prepared Co_3O_4 MNAs material.

Additionally, the stability and reusability of the h-CoO MNAs catalyst was investigated by conducting a series of Cr(VI) photocatalytic experiments. The catalyst was recovered from the reaction mixture simply by filtration and re-dispersed in a fresh Cr(VI) aqueous solution. As illustrated in Figure 53, the h-CoO MNAs show an adequate cycling stability in the examined conditions, retaining about 92% of the initial activity after three consecutive 4-h photocatalytic runs; the apparent reaction rate constant of the photocatalytic reactions was estimated to be k^1=4.6×10^{-3} min^{-1}, k^2=4.0×10^{-3} min^{-1} and k^3=4.1×10^{-3} min^{-1} for first, second and third cycle, respectively. This slight loss of activity might be partly related to the mass loss of the photocatalyst during each isolation step.

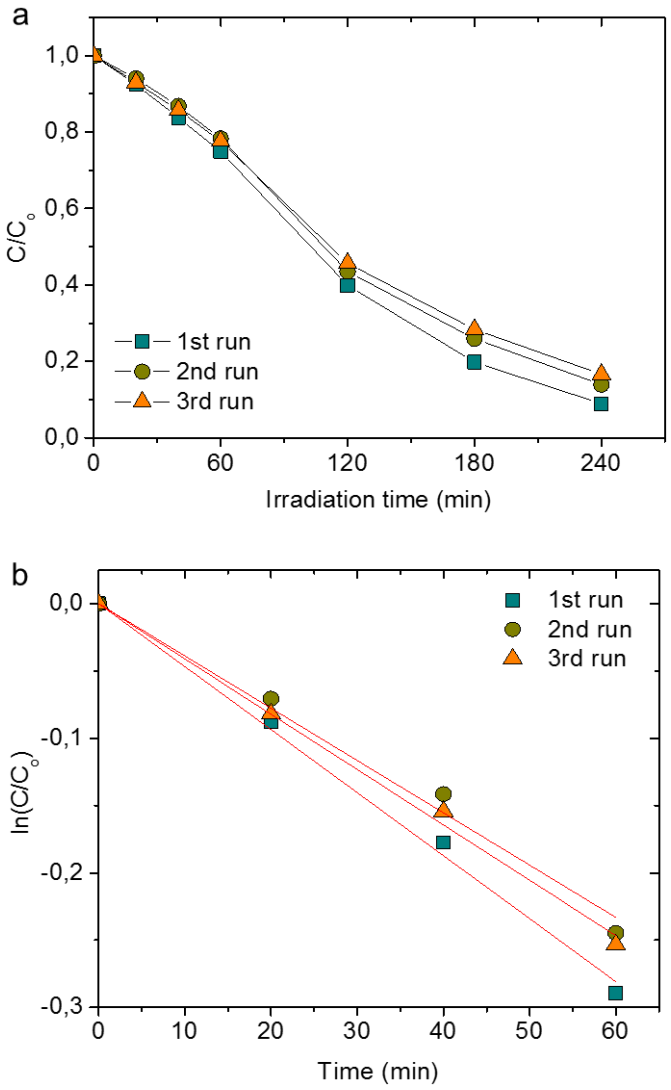

Figure 53. (a) Recycling study of the h-CoO MNAs catalyst and (b) kinetic plots of pseudo-first-order reaction rates (The red lines are fit to the data). Reaction conditions: 0.3 g L^{-1} catalyst, 50 mg L^{-1} Cr(VI), 300-W Xe lamp (λ > 360 nm), pH = 2, 20 ^{o}C.

N_2 physisorption measurements indicated no crystal decomposition and structural collapse or obvious shrinkage for the retrieved h-CoO MNAs catalyst (Figure 54). Moreover, X-ray photoelectron spectroscopy (XPS) measurements (Figure 55) further confirm the CoO chemical nature of the catalysts before and after catalytic test, showing Co $2p_{3/2}$ core-level signal with binding energy at 781.2 eV. This binding energy as well as the broad satellite feature appeared at about 5.5 eV higher binding energy from the main peak are characteristic of the Co(II) oxidation state [164].

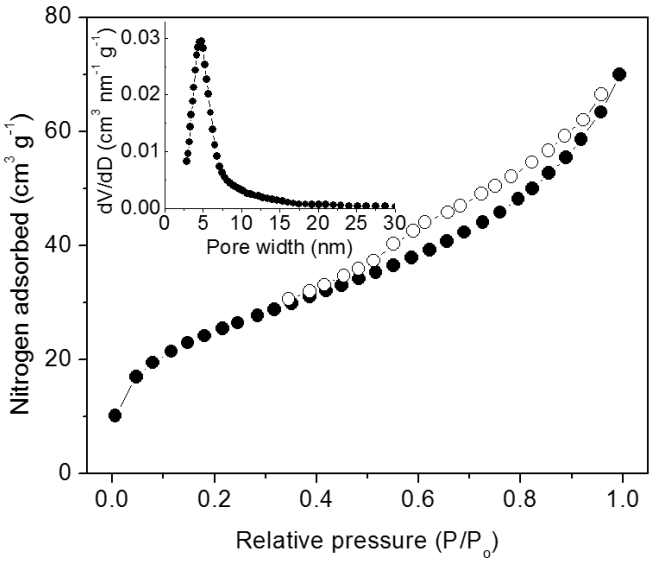

Figure 54. N_2 adsorption-desorption isotherms of the three-times reused h-CoO MNAs catalyst.

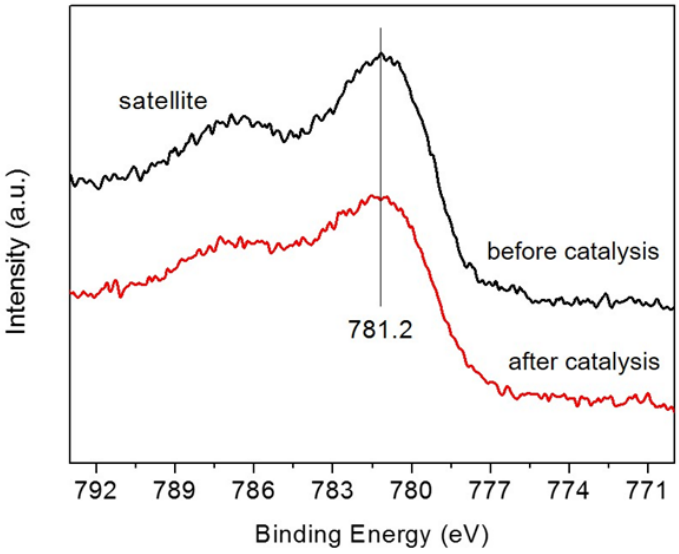

Figure 55. High-resolution Co $2p_{3/2}$ XPS spectra of the h-CoO MNAs catalyst before and after catalysis.

3.5 Reaction mechanism of photocatalytic reduction of aqueous Cr(VI) under UV–visible light

To better understand and interpret the catalytic findings, photocatalytic experiments were carried out in an air-tight cell with h-CoO MNAs catalyst suspended in a 50 ppm Cr(VI) aqueous solution, and the headspace content of the cell was analyzed by a gas chromatography (Shimadzu GC-2014) equipped with a thermal conduction detector. Before irradiation, the solution was purged with argon until oxygen was fully removed (as confirmed by GC analysis). The results directly demonstrate that h-CoO MNAs catalyst is active in O_2 evolution reaction under UV–visible light irradiation, showing an average O_2-production rate of ~1.9 μmol h^{-1} (Figure 56a). To further verify the generation of oxygen during the catalytic reaction, it was performed on-line mass spectrometry measurements of photocatalytic oxygen evolution. In particular, it was conducted the same photocatalytic test as above in a vacuum-tight cell with h-CoO MNAs catalyst and the generated oxygen gas was monitored *in situ* with a mass spectrometer (Hiden HPR-20 QIC gas analyzer). Figure 56b presences the transient photocatalytic O_2 evolution response of h-CoO MNAs under intermittent $\lambda > 360$ nm light irradiation. It can be seen that the production of oxygen increased with time under light illumination, while no oxygen evolution was observed when the reaction was conducted in the dark. This observation clearly confirms that the photocatalytic reduction of Cr(VI) occurs by the spontaneous photooxidation of water at the h-CoO/solution interface. Thus, the main processes of the photocatalytic reaction at acid pH solution can be described as follows:

$$2HCrO_4^- + 14H^+ + 6e^- \rightarrow 2Cr^{3+} + 8H_2O \quad (5)$$

$$3H_2O + 6h^+ \rightarrow \frac{3}{2}O_2 + 6H^+ \quad (6)$$

Consequently, the overall reaction can be described by the Eq. 7.

$$2HCrO_4^- + 8H^+ \rightarrow 2Cr^{3+} + \frac{3}{2}O_2 + 5H_2O \quad (7)$$

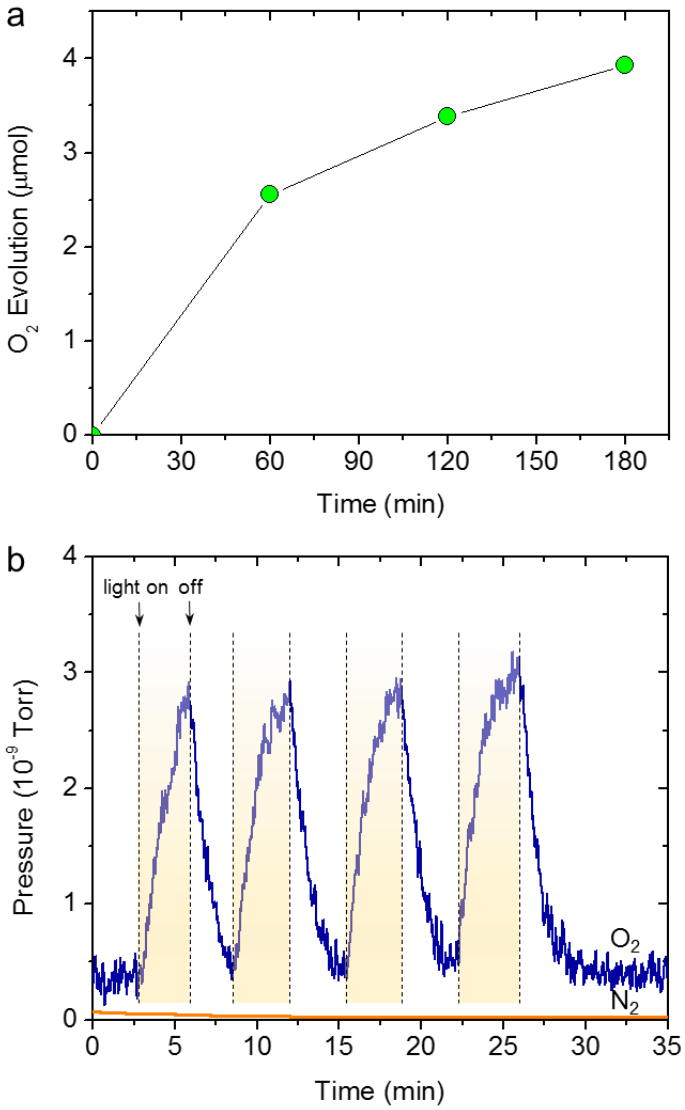

Figure 56. (a) Time course for photocatalytic O_2 evolution and (b) O_2 evolution transient with light on/off for h-CoO MNAs catalyst under UV–visible light (λ > 360 nm) irradiation. Reaction conditions: 0.3 g L^{-1} catalyst, 50 mg L^{-1} Cr(VI), 300-W Xe lamp (λ > 360 nm), pH = 2, 20 ºC.

It is noteworthy that oxygen is produced at a lower rate (~1.9 μmol h^{-1}) with the expected value according to the stoichiometry of $HCrO_4^-$ reduction. It was obtained a ~5.75 μmol h^{-1} of $HCrO_4^-$ reduction rate under UV–visible-light irradiation which, based on Eq. 7, consists in an O_2 evolution rate of about 4.3 μmol h^{-1}. This difference is ascribed to the oxidation of hydroxyl groups or absorbed water molecules at the surface into hydroxyl radicals (·OH) by photogenerated holes:

$$Co–OH_s + h^+ \rightarrow [Co^+ \cdot OH]_s \quad (8)$$

$$H_2O_{abs} + h^+ \rightarrow \cdot OH + H^+ \quad (9)$$

An incontestable qualification for the formation of ·OH radicals during the photocatalytic reduction of Cr(VI) was obtained by the fluorescence probe method, utilizing coumarin in the experiment. Coumarin is an effective probe molecule for monitoring hydroxyl radical in solutions, as it can readily react with ·OH producing umbelliferone. Umbelliferone under excitation at 332 nm, shows a characteristic fluorescence signal at 455 nm wavelength [165]. Figure 57a presents the respective fluorescence spectra obtained at certain time intervals during the course of the reaction. It shows the gradually decrease of coumarin (fluorescence signal at ~398 nm) and increase of umbelliferone (at ~455 nm) emission over 3 h irradiation, recommending the existence of hydroxyl radicals in the solution. It is suspected that an electron-transfer-type oxidation of either surface Co–OH (or Co–O–Co) groups or adsorbed water molecules by photogenerated holes in h-CoO nanoparticles could be responsible for the formation of hydroxyl radicals in the solution.

In general, the oxidation rate of hydroxyl radicals which is a one-electron-transfer process (Eq. 8 and 9) is much faster than the rate of the oxygen photoevolution reaction, i.e. $2H_2O \rightarrow O_2 + 4H^+ + 4e^-$. Comparatively, it was also conducted the same experiment using the c-CoO MNAs as a catalyst. As revealed in Figures 57b and c, the c-CoO MNAs catalyst exhibits an approximately 2.7-fold lower production rate of ·OH radicals, which is defined by the ratio of intensity between umbelliferone and coumarin, than that of h-CoO MNAs at identical conditions. The lower OH^- oxidation kinetics for c-CoO MNAs could be attributed to the most stable Co–OH bond of cubic CoO structure, which impedes the formation of hydroxyl radicals and subsequently conversion to umbelliferone. These results suggest that the favorable oxidation of surface hydroxyl groups by surface-trapped holes (instead of the sluggish water dissociation step) plays a critical role in accelerating the oxidation rate, resulting in a rapid generation of ·OH radicals.

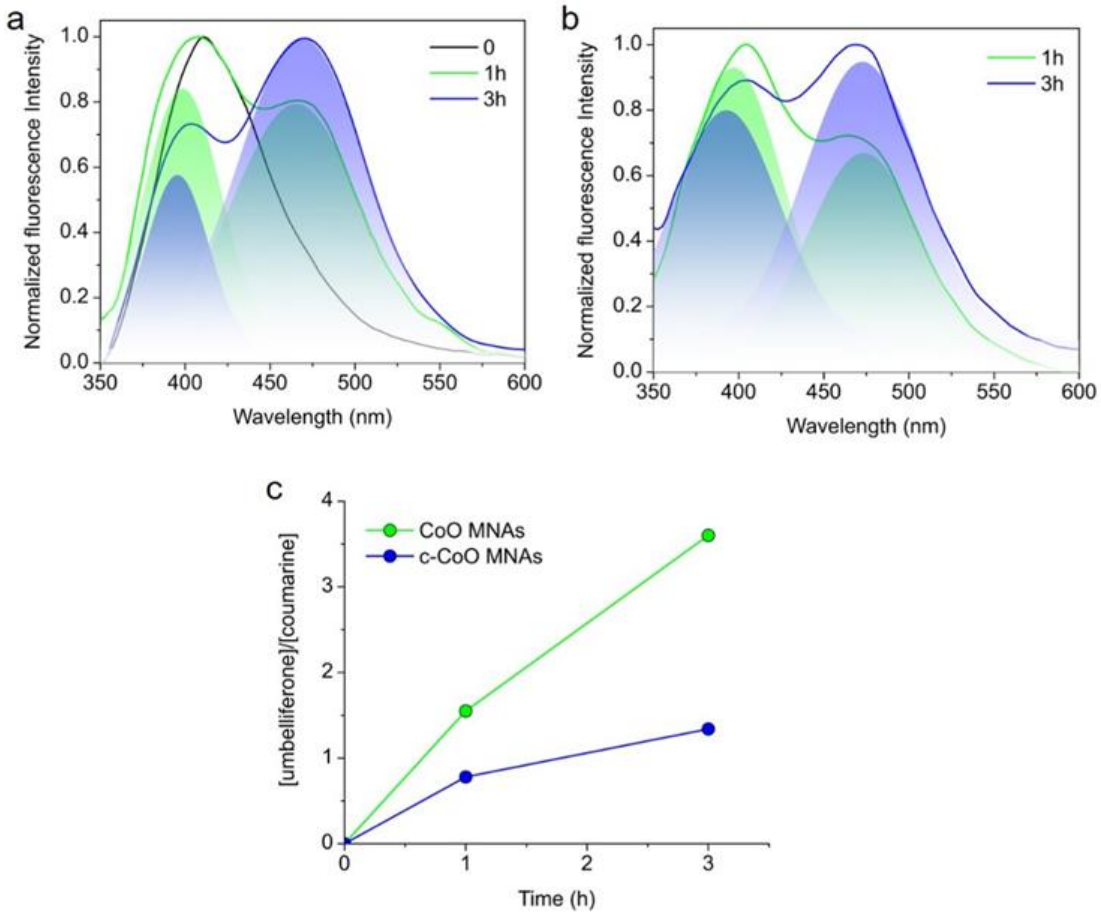

Figure 57. Time course of fluorescence spectra of the coumarin in water for (a) h-CoO MNAs and (b) c-CoO MNAs catalyst. In pane (a), the fluorescence spectrum of coumarin (t = 0) is also given. (c) The integrated fluorescence intensity ratio of the umbelliferone emission at ~455 nm to coumarin emission at ~398 nm for h-CoO MNAs and c-CoO MNAs catalysts. Reaction conditions: 0.3 g L^{-1} catalyst, 50 mg L^{-1} Cr(VI), 10 mM coumarine, 300-W Xe lamp ($\lambda > 360$ nm), pH = 2, 20 ºC. Fluorescence emission spectra were obtained with an excitation wavelength of 332 nm.

The electronic band structure and optical transitions in h-CoO nanoparticle assemblies were investigated by combining electrochemical impedance (EIS) and UV–vis spectroscopy. Figure 58 displays the Mott-Schottky plot and the corresponding fit of the linear portion of inverse square of capacitance ($1/C^2$) of the space charge region *versus* electrode potential (E) for the h-CoO MNAs catalyst. The extrapolation to $1/C^2 = 0$ was used to determine the flat-band potential (E_{FB}) of h-CoO MNAs, which was calculated to be –0.04 V *vs* NHE at pH = 7. Moreover, the electron donor density (N_D) of h-CoO is 4.02×10^{16} cm^{-3}, as

determined by the slope of the $1/C^2$ *versus* E plot. Note that the positive slope of the Mott-Schottky plot indicates that h-CoO MNAs shows n-type behavior. The VB maximum for h-CoO MNAs is thus estimated at 2.57 V *vs* NHE (pH = 7) from the difference of E_{FB} and energy band gap (E_g) of the semiconductor. The E_g value of h-CoO MNAs, which was determined from optical absorption data using the Tauc equation, was found to be ~2.61 eV (Figure 59). Comparatively, the calculated energy gap of h-CoO RNAs was estimated to be slightly lower at ~2.56 eV, as expected due to smaller pore structure.

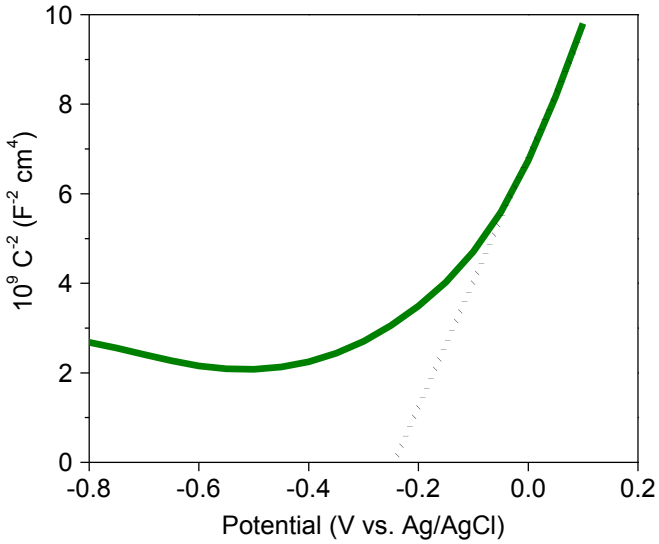

Figure 58. Mott-Schottky plot of the h-CoO MNAs catalyst.

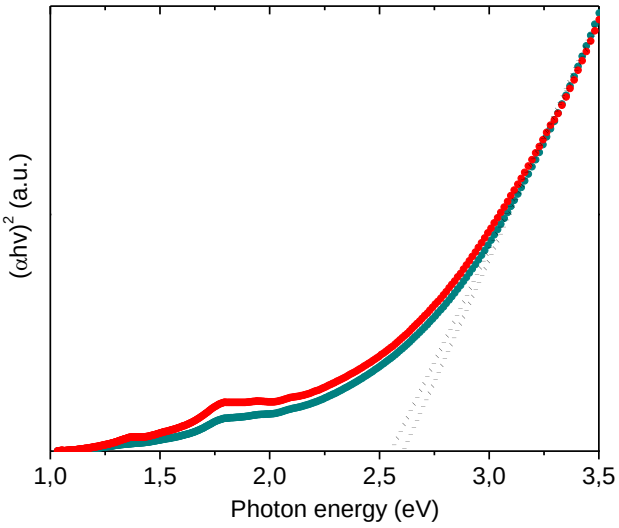

Figure 59. Tauc plots [$(\alpha hv)^2$ *versus* photon energy, where α is the absorption coefficient, h is the Planck's constant, and v is the light frequency] derived from UV–vis optical absorption data for h-CoO MNAs (green line) and h-CoO RNAs (red line) materials.

In light of these findings, a potential photocatalytic mechanism for the reduction of Cr(VI) has been proposed, as shown in Figure 60. In short, under UV ($\lambda > 360$ nm) or visible ($\lambda \geq 420$ nm) light irradiation, h-CoO nanoparticles get excited and generate electron-hole pairs. The favourable thermodynamic conditions of the band structure drives the transfer of photoexcited electrons from the CB to the Cr(VI) species; the CB edge of h-CoO nanoparticles lies above the redox potential of the $HCrO_4^-/Cr^{3+}$ couple (0.86 V) [166]. Meanwhile, since the VB level of h-CoO nanoparticles is more positive than the O_2/H_2O redox potential (0.82 V *vs* NHE, pH = 7), the photogenerated holes can oxidize water, producing oxygen. In addition, during the course of irradiation, a fraction of surface-trapped holes (Lewis acids) may be also transferred to the hydroxyl groups or adsorbed water molecules (Lewis bases), causing the formation of ·OH radicals. Indeed, the redox potentials of $\cdot OH/OH^-$ (E^o = 1.58 V) [167] and $\cdot OH/H_2O$ (E^o = 1.92 V) [168] pairs are above the VB edge of h-CoO nanoparticles (2.57 V) and their oxidation is a viable possibility. The presence of ·OH radicals in the solution was evidenced by fluorescence spectroscopy (Figure 57). This observation is in line with previous studies that report the phase transformation of hexagonal CoO to β-$Co(OH)_2$ by hydration of the CoO surface [169]. Such cobalt hydroxide species on the surface of h-CoO nanoparticles may possess advantages for the formation of hydroxyl radicals during the photocatalytic reaction.

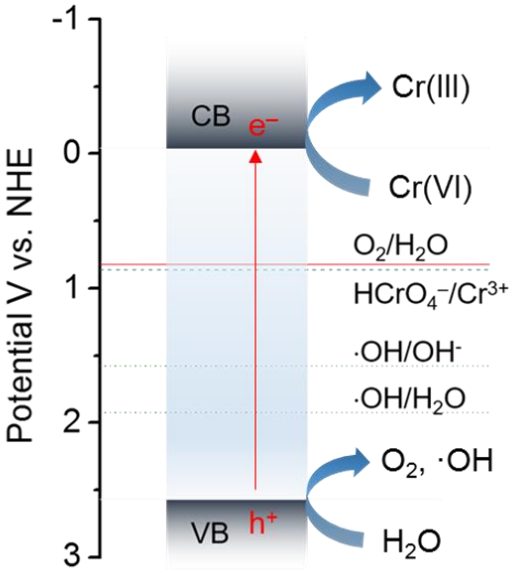

Figure 60. Energy band diagram and possible reaction mechanism for the photocatalytic reduction of Cr(VI) over h-CoO MNAs catalyst.

It must be noted that the resultant ·OH radicals also have the ability to recombine with each other, producing H_2O_2, which may further be oxidized by the holes to dioxygen [170]. Meanwhile, the *in situ* generated ·OH radicals may be also considered as a primary oxidant for the photocatalytic degradation of organic pollutants at the CoO surface, such as phenol, facilitating the charge carrier separation through the fast hole transfer kinetics and, thus, accelerating the overall Cr(VI) reduction process.

3.6 Morphology and structural characterization of Ni and Cu-doped c-CoO MNAs

The synthesis of mesoporous assemblies from colloidal cubic $Co_{1-x}Ni_xO$ (denoted as c-$Co_{1-x}Ni_xO$ MNAs) and $Co_{1-x}Cu_xO$ (denoted as c-$Co_{1-x}Cu_xO$ MNAs) nanoparticles (x = 0, 0.01, 0.02 and 0.05) was accomplished by a polymer-templated self-assembly method, in a similar way as the hexagonal CoO MNAs. Briefly, a BF_4^--stabilized c-$Co_{1-x}Ni_xO$ or c-$Co_{1-x}Cu_xO$ nanoparticles solution was slowly added to a clear solution of poly(ethylene oxide)-*b*-poly(propylene oxide)-*b*-poly(ethylene oxide) block copolymer (10 wt%) in tetrahydrofuran (THF). The mixture was reacted for 2 h, followed by a slow evaporation of the solvent (within 5 days at 40 ^oC). Then, annealing of the dry product at 350 ^oC for 4 h under nitrogen results in formation of a mesoporous network of connected nanoparticles with a large internal surface area and open pore structure. The removal of the polymer template upon heating was verified by thermogravimetric analysis (TGA). The TGA plot of mesostructured c-CoO/polymer composite in Figure 61 shows a weight loss of about 5.2% in the 40–120 ^oC temperature range due to the removal of residual solvent and a ca. 71.9% weight loss between 120 and 500 ^oC, which is attributed to the decomposition of organic polymer. Additionally, the TGA plot of mesoporous c-CoO MNAs sample shows a ~2.5% weight loss between 40 and 180 ^oC due to the removal of physisorbed solvents and a weight loss of ~10.6% in the 180–480 ^oC temperature range, which is attributed to the decomposition of residual carbon species. Both mesostructured (containing surfactant) and mesoporous c-CoO MNAs materials display a weight loss (~7.4% and ~28.7% respectively) in the temperature range 480–600 ^oC, which is attributed to the reduction of CoO to metallic Co. X-ray diffraction measurement of the inorganic residue after TGA analysis signified this conversion; a similar chemical conversion was also mentioned for h-CoO MNAs. In Figure 62, all XRD peaks can be indexed to the metallic Co with a face-centered cubic (JCPDS No. 15-0806) and hexagonal close-packed (JCPDS No. 05-0727) structure. The Ni and Cu content of modified c-CoO MNAs was determined with energy dispersive X-ray spectroscopy (EDS) and anodic stripping voltammetry (ASV) (for c-$Co_{1-x}Ni_xO$ MNAs samples), and the results are very close to the expected composition from the stoichiometry of reactions (Figure 63, Tables 1–2).

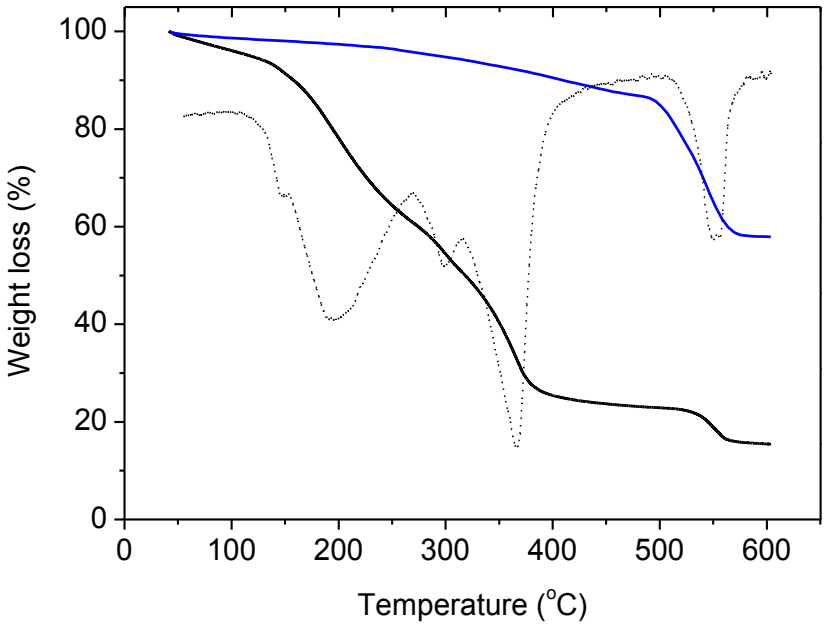

Figure 61. TGA profile of (a) as-prepared containing surfactant (black line) and (b) mesoporous c-CoO MNAs (blue line) recorded under N_2 flow (~200 mL min^{-1}). The differential thermogravimetric (DTG) curve (dotted line) for as-prepared material is also given.

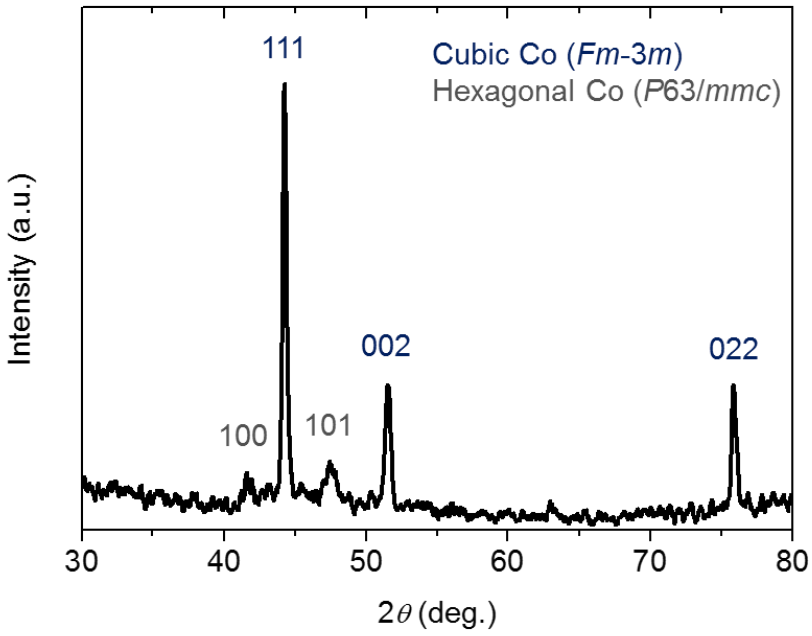

Figure 62. XRD pattern of the inorganic residue obtained from c-CoO/polymer after TGA analysis (up to 600 ºC, in N_2).

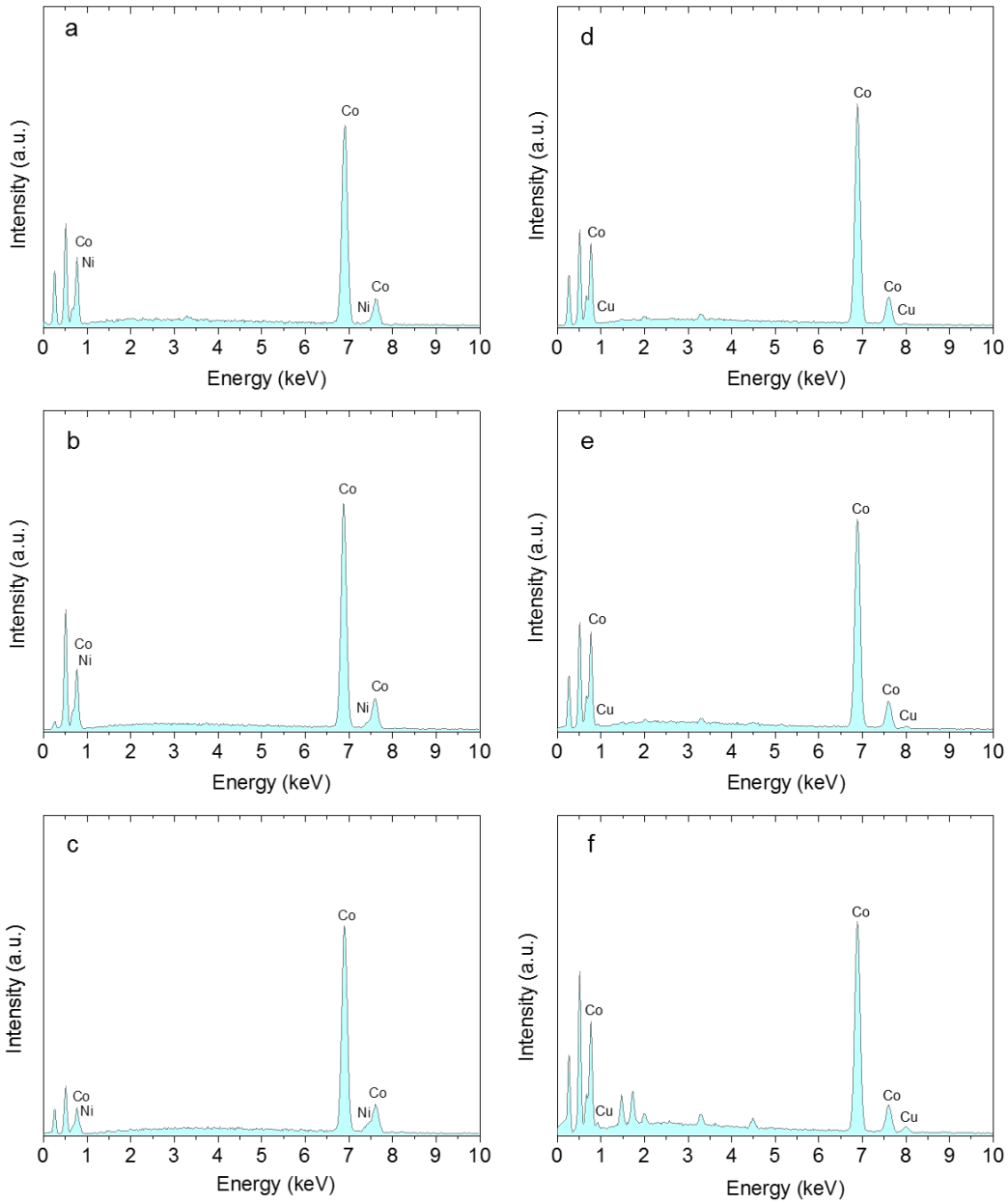

Figure 63. Typical EDS spectra of c-$Co_{1-x}Ni_xO$ MNAs for (a) x=0.01, (b) x=0.02, (c) x=0.05 and c-$Co_{1-x}Cu_xO$ MNAs for (d) x=0.01, (e) x=0.02 and (f) x=0.05.

X-ray diffraction measurements were performed to investigate the crystal structure of the as-prepared c-$Co_{1-x}Ni_xO$ and c-$Co_{1-x}Cu_xO$ MNAs materials. In Figures 64 and 65, all samples exhibit broad yet distinct XRD peaks that correspond to the cubic rock-salt structure of CoO (JCPDS no 48-1719, *Fm*3*m*). No impurity peaks corresponding to other chemical phases of cobalt like Co_3O_4 were detected, indicating the phase purity of the samples. However, due to the low concentration of both Ni and Cu in c-$Co_{1-x}Ni_xO$ and c-$Co_{1-x}Cu_xO$ MNAs,

respectively, no corresponding XRD peaks can be observed. Using the peak width of the (200) diffraction and Scherrer's equation, the grain size of the mesoporous samples was estimated to be ~6.5–7 nm, which is equal to the grain size of the precursor nanoparticles (Figure 66).

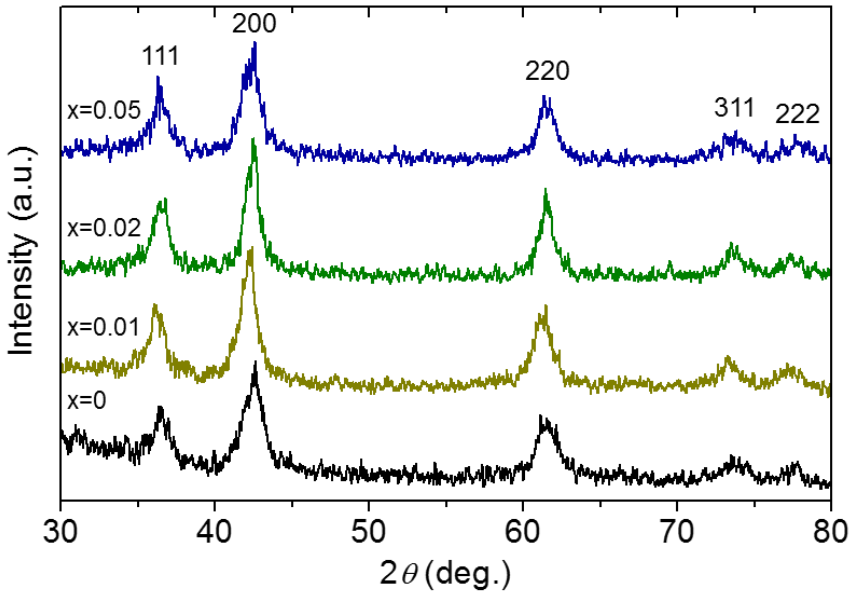

Figure 64. XRD patterns of c-$Co_{1-x}Ni_xO$ MNAs materials.

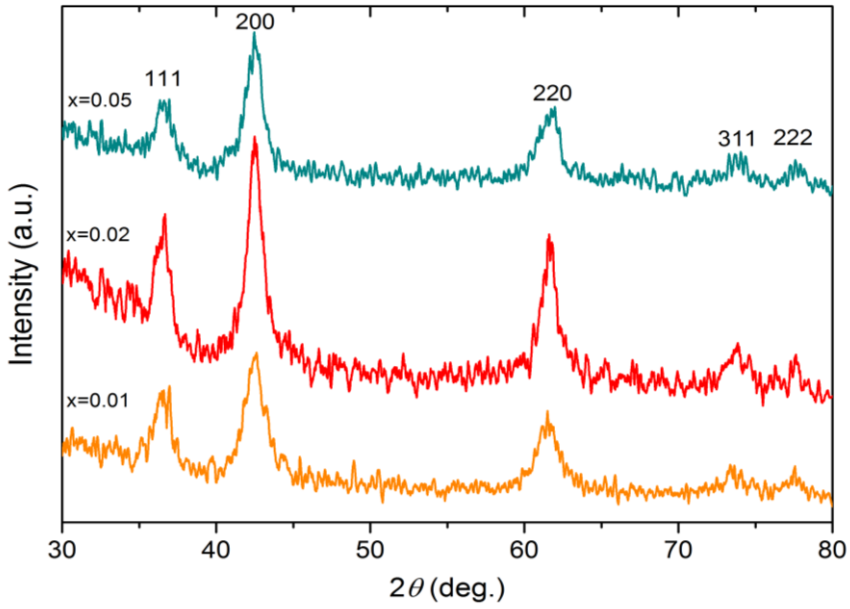

Figure 65. XRD patterns of c-$Co_{1-x}Cu_xO$ MNAs materials.

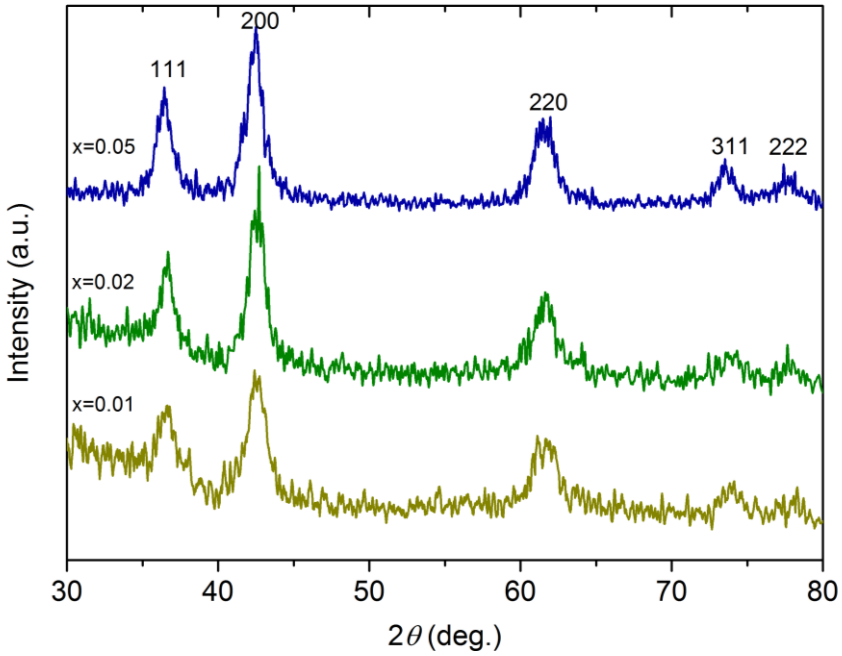

Figure 66. XRD pattern of the precursor (BF_4^--capped) c-$Co_{1-x}Ni_xO$ nanoparticles.

Figure 67 displays typical transmission electron microscopy (TEM) images for the c-$Co_{0.98}Ni_{0.02}O$ MNAs catalyst, which as it is illustrated below displays the best catalytic activity among the c-$Co_{1-x}Ni_xO$ MNAs and c-$Co_{1-x}Cu_xO$ MNAs materials. It shows a porous network of connected nanoparticles with an average diameter of 5–6 nm, which is very close to the crystallite size obtained from XRD. This implies minimal grain coarsening of the CoO nanoparticles during synthesis. Crystal structure features of c-$Co_{0.98}Ni_{0.02}O$ MNAs were also characterized by high-resolution TEM (HRTEM) and selected-area electron diffraction (SAED) analyses. The HRTEM image suggests single-crystalline particles, showing distinct lattice fringes throughout the entire particles with ~2.1 Å interlayer distances that correspond to the (200) planes of cubic CoO (Figure 68a). The SAED pattern taken from a small area of the assembled c-$Co_{0.98}Ni_{0.02}O$ structure corroborates the polycrystalline nature of the sample, showing a series of Debye-Scherrer diffraction rings (Figure 68b). In agreement with XRD results, these diffraction rings can be assigned to the cubic phase of CoO.

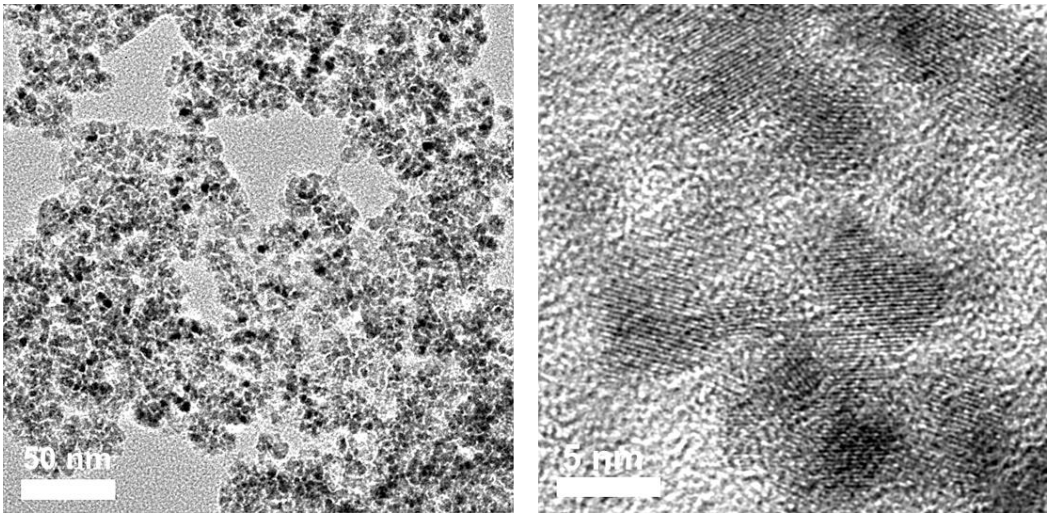

Figure 67. Typical TEM images of the $Co_{0.98}Ni_{0.02}O$ MNAs.

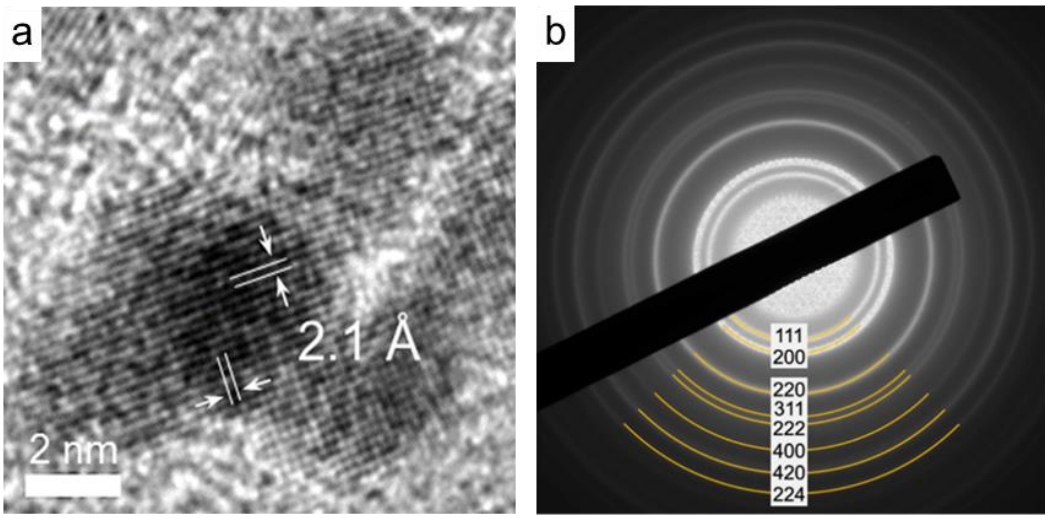

Figure 68. (a) High-Resolution TEM, showing the lattice fringes of CoO along the [001] direction and (b) SAED pattern of $Co_{0.98}Ni_{0.02}O$ MNAs.

N_2 physisorption measurements of c-$Co_{1-x}Ni_xO$ and c-$Co_{1-x}Cu_xO$ assemblies corroborate that they contain mesopores within the nanoparticles. The Brunauer-Emmett-Teller (BET) surface areas and pore volumes of the Ni-implanted samples were estimated to be 108–115 $m^2 g^{-1}$ and 0.15–0.16 $cm^3 g^{-1}$, respectively, and these of Cu-implanted samples were estimated to be 99–102 $m^2 g^{-1}$ and 0.12–0.15 $cm^3 g^{-1}$, which are similar to those of pure c-CoO MNAs (137 $m^2 g^{-1}$ and 0.15 $cm^3 g^{-1}$, respectively). All the materials showed type-IV adsorption-desorption isotherms

with a H_3 type hysteresis loop, which is characteristic of mesoporous solids with slit-like pores. Analysis of the adsorption data with the non-local density functional theory (NLDFT) method showed a quite narrow distribution of pore sizes with a pore size of 4.3–4.5 nm for c-$Co_{1-x}Ni_xO$ MNAs (Figure 69) and 4.4–4.7 nm for c-$Co_{1-x}Cu_xO$ MNAs (Figure 70). All the textural properties of the c-$Co_{1-x}Ni_xO$ MNAs and c-$Co_{1-x}Cu_xO$ MNAs catalysts are listed in Tables 1 and 2, respectively.

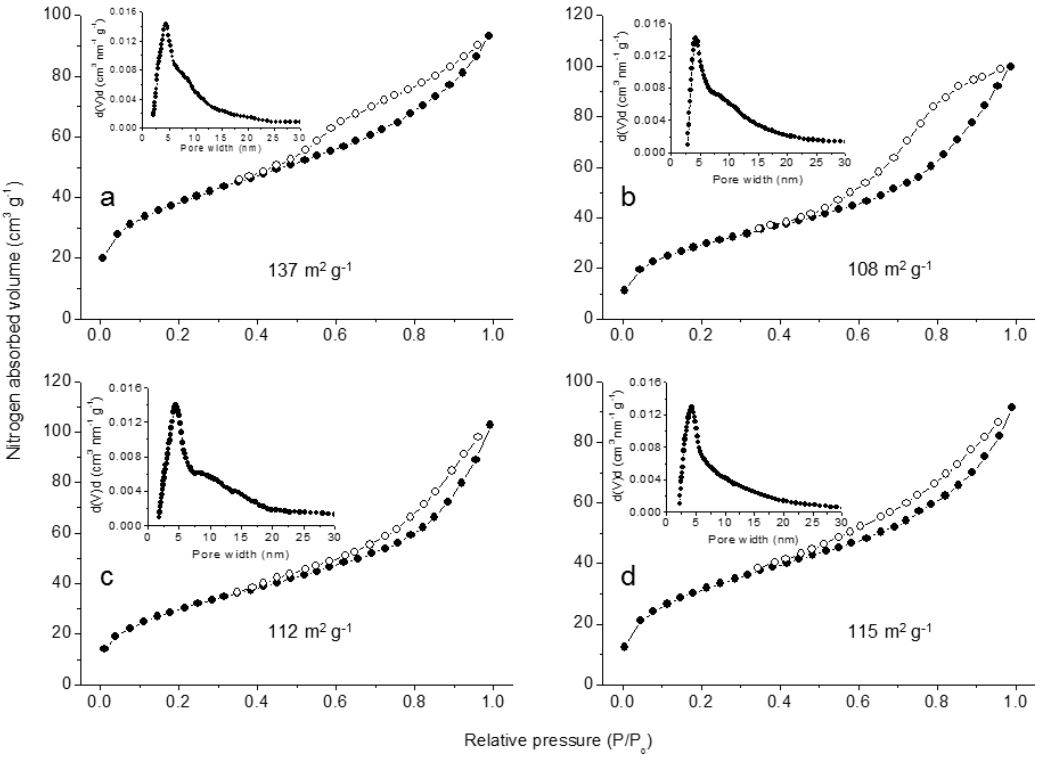

Figure 69. N_2 adsorption (filled cycles) and desorption (open cycles) isotherms at –196 °C and the corresponding NLDFT pore-size distribution plots (inset) for c-$Co_{1-x}Ni_xO$ MNAs: (a) x = 0, (b) x = 0.01, (c) x = 0.02 and (d) x = 0.05.

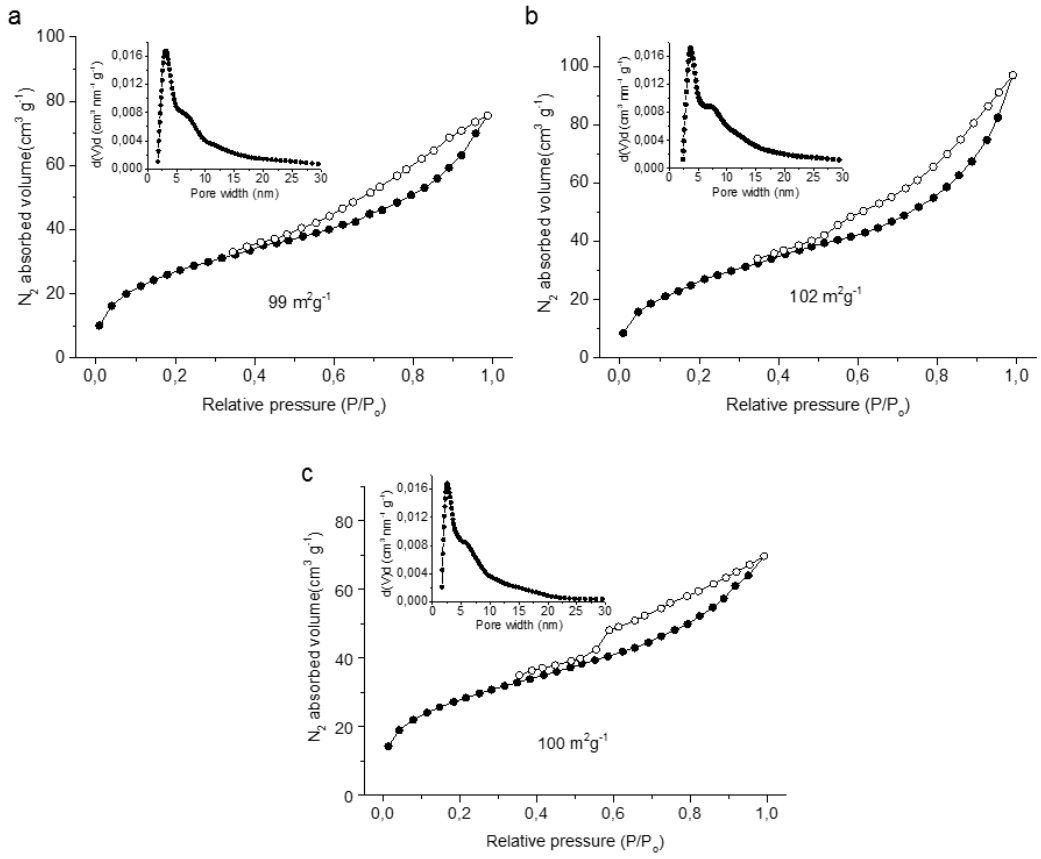

Figure 70. N_2 adsorption (filled cycles) and desorption (open cycles) isotherms at –196 ºC and the corresponding NLDFT pore-size distribution plots (inset) for c-$Co_{1-x}Cu_xO$ MNAs: (a) x = 0.01, (b) x = 0.02 and (c) x = 0.05.

Table 1. Analytical data and textural properties of mesoporous $Co_{1-x}Ni_xO$ nanoparticle assemblies (MNAs).

Sample	Ni content[a] (atomic%)		Surface area ($m^2\ g^{-1}$)	Pore volume[b] ($cm^3\ g^{-1}$)	Pore size (nm)
	EDS	ASV			
CoO MNAs			137	0.15	4.4
$Co_{0.99}Ni_{0.01}O$ MNAs	0.99	1.09 ±0.14	108	0.16	4.3
$Co_{0.98}Ni_{0.02}O$ MNAs	1.89	2.06 ±0.07	112	0.16	4.5
$Co_{0.95}Ni_{0.05}O$ MNAs	4.81	4.97 ±0.44	115	0.15	4.4

[a]Ni/(Co+Ni) atomic ratio based on EDS and anodic stripping voltammetry (ASV) analysis.
[b]Cumulative pore volume at P/P_o of 0.98.

Table 2. Analytical data and textural properties of mesoporous $Co_{1-x}Cu_xO$ nanoparticle assemblies (MNAs).

Sample	Cu content[a] (atomic%)	Surface area ($m^2\ g^{-1}$)	Pore volume[b] ($cm^3\ g^{-1}$)	Pore size (nm)
$Co_{0.99}Cu_{0.01}O$ MNAs	0.60	99	0.13	4.7
$Co_{0.98}Cu_{0.02}O$ MNAs	1.28	102	0.15	4.5
$Co_{0.95}Cu_{0.05}O$ MNAs	3.74	100	0.12	4.4

[a]Cu/(Co+Cu) atomic ratio based on EDS analysis. [b]Cumulative pore volume at P/P_o of 0.98.

The surface chemical state of pristine c-CoO and c-$Co_{0.98}Ni_{0.02}O$ MNAs are investigated with X-ray photoelectron spectroscopy (XPS). For c-CoO MNAs, the Co $2p_{3/2}$ XPS core-level peak is detected at binding energy of 781.1 eV with a shake-up satellite feature at about 786.4 eV (Figure 71a), providing convincing evidence of the existence of Co^{2+} ions [171]. The Co $2p_{3/2}$ signal is clearly observed at slightly lower binding energies (780.8 eV) for the c-$Co_{0.98}Ni_{0.02}O$ MNAs, possibly due to a partial electron transfer from Ni to Co through the bridging oxygen atoms. Specifically, the single occupied 3d t_{2g} orbital of high-spin Co^{2+} ($t_{2g}^5e_g^2$ electron configuration) can interact with the oxygen lone pairs, accepting electrons via π-donation. After Ni doping, the fully occupied 3d t_{2g} states of Ni^{2+} ($t_{2g}^6e_g^2$ electron configuration) can strengthen the partial electron transfer from oxygen to Co^{2+} due to the repulsive interactions with the occupied 2p orbitals of O^{2-} ions [172] (Figure 72). In agreement with this, the O 1s XPS spectrum of c-$Co_{0.98}Ni_{0.02}O$ MNAs (Figure 71b), which is deconvoluted into two peaks corresponding to the lattice oxygen (530.0 eV) and the hydroxyl groups (532.0 eV), was found to be slightly red-shifted with respect to c-CoO (530.3 eV and 532.2 eV). This shift is thought to be related to the incorporation of Ni. Comparatively, the O 1s line of polycrystalline NiO is deconvoluted into two peaks at around 529.4 eV and 531.2 eV. Since the Ni content in c-$Co_{0.98}Ni_{0.02}O$ MNAs is as low as 1.56 wt%, it was difficult to directly detect Ni in the XPS survey spectrum (within the 854.2–854.5 eV region).

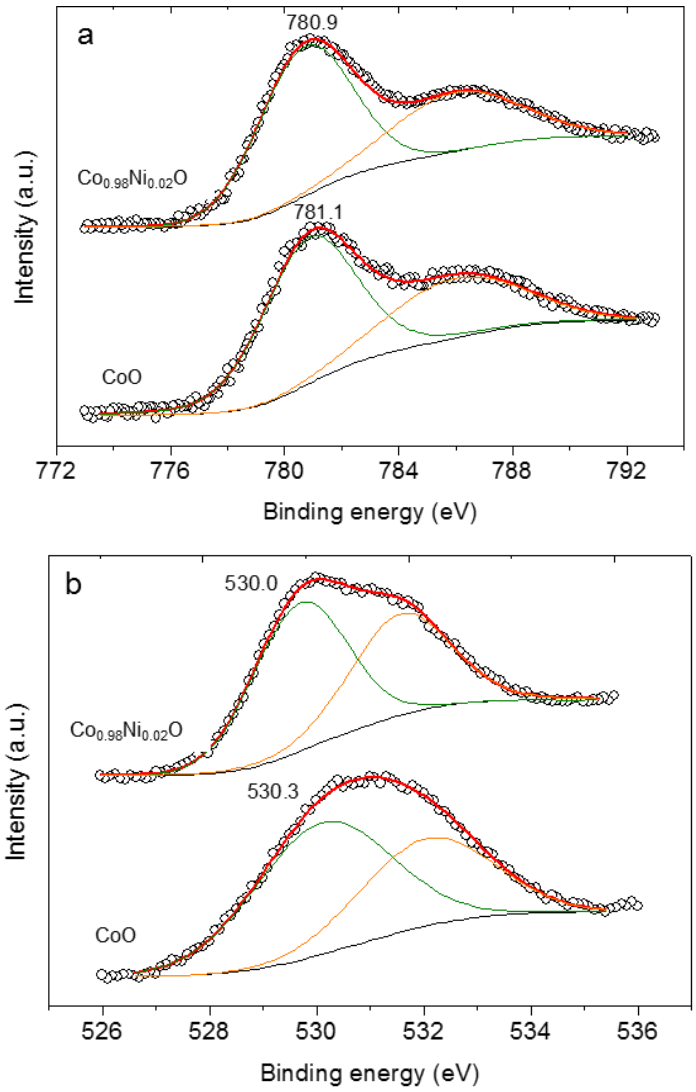

Figure 71. XPS spectrums of the (a) Co $2p_{3/2}$ and (b) O 1s core-levels of c-CoO and c-$Co_{0.98}Ni_{0.02}O$ MNAs.

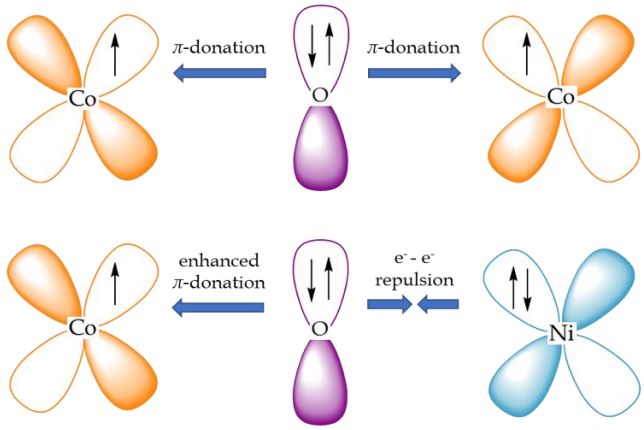

Figure 72. Schematic representation of the electronic coupling between Co, Ni and O before and after Ni doping in c-$Co_{1-x}Ni_xO$ MNAs.

In line with XPS results, in Figure 73, the valence band (VB) spectra of c-CoO and c-$Co_{0.98}Ni_{0.02}O$ MNAs provide an additional hint for the incorporation of Ni into the CoO lattice. The c-CoO MNAs shows a photoemission onset, which is defined as the energetic difference between the Fermi energy and the VB edge, at about 0.31 eV, indicating a p-type character. For the c-$Co_{0.98}Ni_{0.02}O$ MNAs, the photoemission onset is shifted to ca. 0.26 eV, revealing that Ni doping leads to a downshift of the Fermi level. Consistent with this interpretation, the photoelectron onset of polycrystalline NiO was found at 0.22 eV.

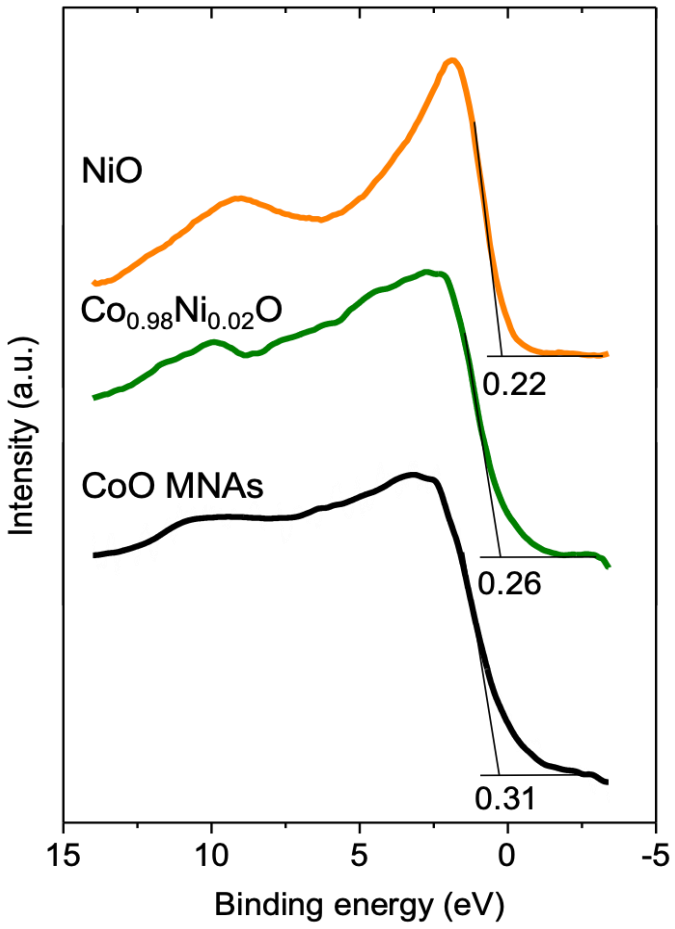

Figure 73. Valence band spectra of NiO polycrystalline and c-CoO and c-$Co_{0.98}Ni_{0.02}O$ MNAs catalysts.

3.7 Photocatalytic study of c-$Co_{1-x}Ni_xO$ and c-$Co_{1-x}Cu_xO$ MNAs

The catalytic activity of the c-$Co_{1-x}Ni_xO$ and c-$Co_{1-x}Cu_xO$ MNAs materials was investigated in photocatalytic reduction of aqueous Cr(VI) solutions under UV-visible light irradiation (λ > 360 nm). Figure 74 depicts the evolution of photocatalytic Cr(VI) reduction over c-$Co_{1-x}Ni_xO$ MNAs catalysts (at 0.3 g L^{-1} concentration) with different Ni loadings, i.e. from 0 to 5%. The comparison shows that materials doped with Ni exhibit better performance for Cr(VI) reduction than c-CoO MNAs. Especially $Co_{0.98}Ni_{0.02}O$ MNAs achieve a ~90% Cr(VI) conversion in 4 h, which is markedly higher than that of pure c-CoO MNAs (~46% conversion level at 4 h). On the other hand, under identical conditions the evolution of photocatalytic Cr(VI) reduction over c-$Co_{1-x}Cu_xO$ MNAs indicated that, although these materials exhibit higher catalytic performance than c-CoO MNAs, they show lower efficiency than c-$Co_{0.98}Ni_{0.02}O$ MNAs, affording a ~70% Cr(VI) conversion in 4 h (at c-$Co_{0.98}Cu_{0.02}O$ composition) (Figure 75).

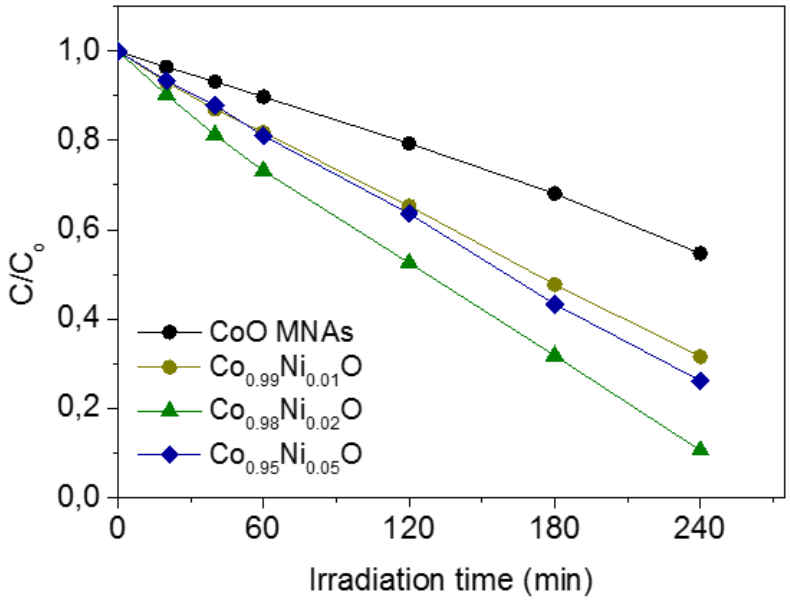

Figure 74. Photocatalytic reduction of aqueous Cr(VI) with c-$Co_{1-x}Ni_xO$ MNAs catalysts. Reaction conditions: 0.3 g L^{-1} catalyst, 50 mg L^{-1} Cr(VI) solution, 300-W Xe lamp (λ > 360 nm), pH = 2, 20 ^oC.

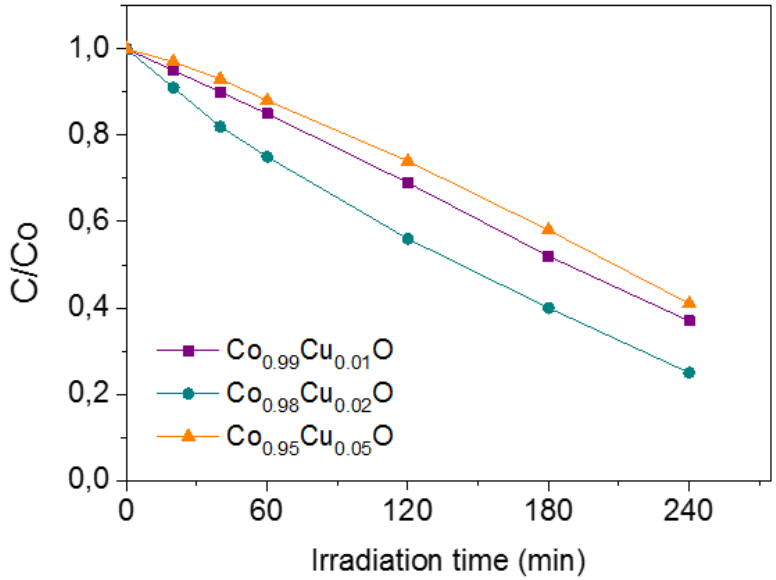

Figure 75. Photocatalytic reduction of aqueous Cr(VI) with c-$Co_{1-x}Cu_xO$ MNAs catalysts. Reaction conditions: 0.3 g L^{-1} catalyst, 50 mg L^{-1} Cr(VI) solution, 300-W Xe lamp ($\lambda >$ 360 nm), pH = 2, 20 ºC.

By performing a series of photocatalytic Cr(VI) reduction tests with the more efficient catalyst (c-$Co_{0.98}Ni_{0.02}O$ MNAs) in different loadings (from 0.2 to 0.4 g L^{-1}) (Figure 76), the optimum catalyst dosage is found to be 0.3 g L^{-1} (as for hexagonal CoO MNAs). The outstanding photocatalytic performance of $Co_{0.98}Ni_{0.02}O$ MNAs is also evident by its high apparent quantum yield (AQY) ~1.5% at 375 nm and ~0.8% at 410 nm, which is comparable or even higher to that of other highly active catalysts [155-158]. Because of the visible light absorption of c-CoO, Cr(VI) photocatalytic reduction experiments were also carried out under irradiation of $\lambda \geq$ 420 nm light using c-$Co_{0.98}Ni_{0.02}O$ MNAs and the results indicated that they can also perform photocatalytic Cr(VI) reduction with reasonable activity. As shown in Figure 77, a ~50% Cr(VI) conversion level was obtained with visible-light irradiated c-$Co_{0.98}Ni_{0.02}O$ MNAs, comparatively to ~27% conversion by c-CoO MNAs dispersions in 4 h.

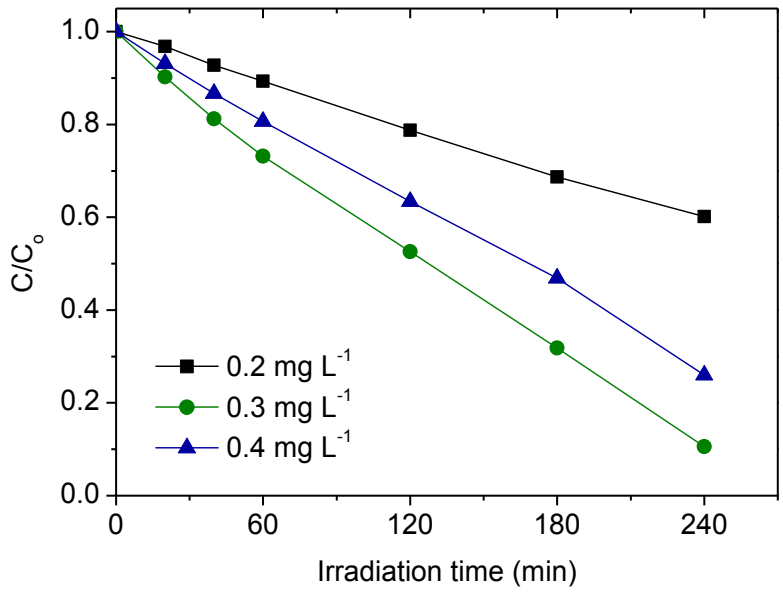

Figure 76. Concentration dependent photocatalytic Cr(VI) reduction activity of c-$Co_{0.98}Ni_{0.02}O$ MNAs. Reaction conditions: 0.2–0.4 g L^{-1} of catalyst, 50 mg L^{-1} Cr(VI) aqueous solution, pH = 2, UV-visible light (λ > 360 nm) irradiation, 20 ºC.

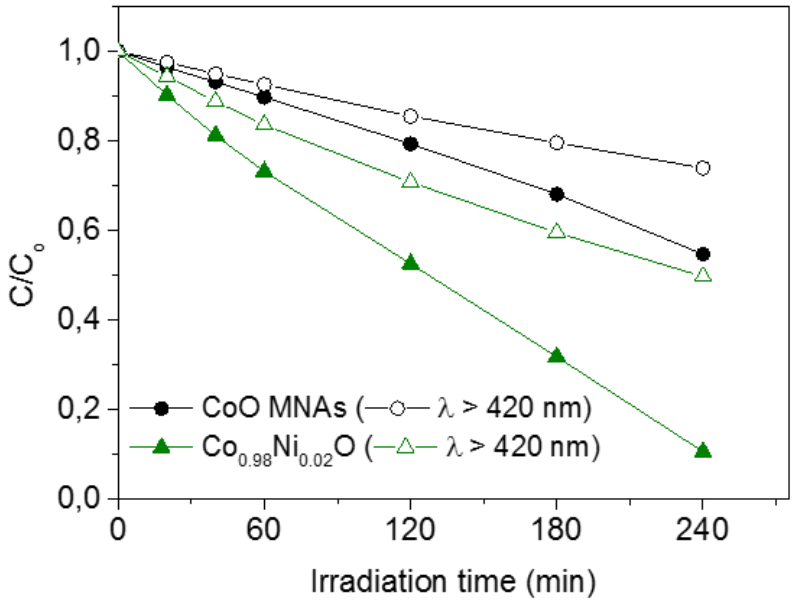

Figure 77. Photocatalytic reduction of aqueous Cr(VI) with c-CoO and c-$Co_{0.98}Ni_{0.02}O$ MNAs catalysts under λ > 360 nm and λ ≥ 420 nm light irradiation. Reaction conditions: 0.3 g L^{-1} catalyst, 50 mg L^{-1} Cr(VI) aqueous solution, 300-W Xe light radiation with a long-pass cut-off filter allowing λ > 360 nm or λ ≥ 420 nm, pH = 2, 20 ºC

The c-$Co_{0.98}Ni_{0.02}O$ MNAs catalyst also demonstrates very good stability over a period of 12 h under illumination. The reusability of the catalyst was assessed within three recycling tests, in which the catalyst was collected by centrifugation and re-dispersed in a fresh Cr(VI) aqueous solution. The results shown in Figure 78 reveal that the c-$Co_{0.98}Ni_{0.02}O$ MNAs retain more than 94% of its initial activity after recycling. Moreover, X-ray diffraction, N_2 porosimetry and X-ray photoelectron spectroscopy characterizations of the reused sample indicated that the crystal structure, porous morphology and surface chemical state are well maintained after catalysis, substantiating high durability. In the XRD pattern (Figure 79), all the diffraction peaks can be assigned to the cubic phase of CoO (JCPDS No. 43-1004). Analysis of the N_2 adsorption-desorption isotherms (Figure 80) indicate a BET surface area of 92 m^2 g^{-1} and a pore volume of 0.13 cm^3 g^{-1}, while the Co $2p_{3/2}$ XPS spectrum of the reused c-$Co_{0.98}Ni_{0.02}O$ MNAs sample shows a Co $2p_{3/2}$ peak at 780.8 eV associated with a shake-up satellite peak at 785.7 eV (Figure 81), in consistent with the results of fresh catalyst.

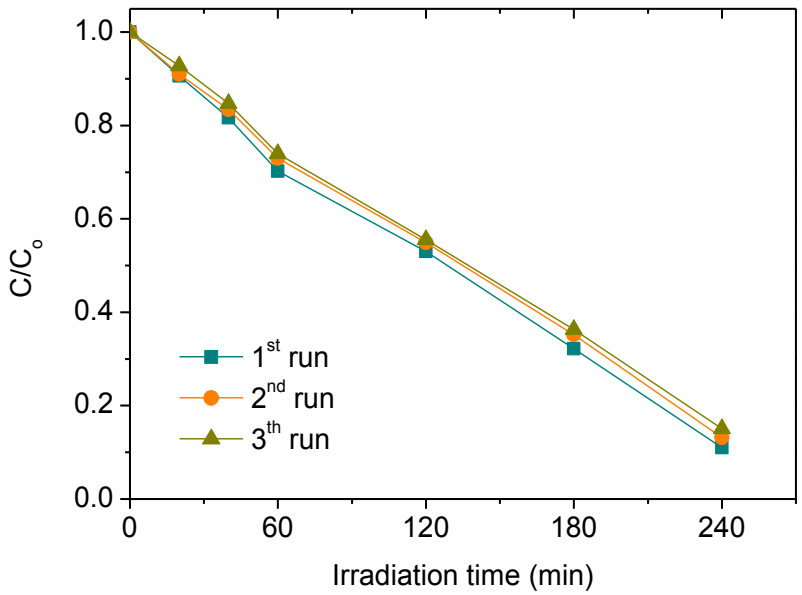

Figure 78. Recycling study of c-$Co_{0.98}Ni_{0.02}O$ MNAs catalyst. Reaction conditions: 0.3 g L^{-1} of catalyst, 50 mg L^{-1} Cr(VI) aqueous solution, pH = 2, UV-visible light (λ > 360 nm) irradiation, 20 ^oC.

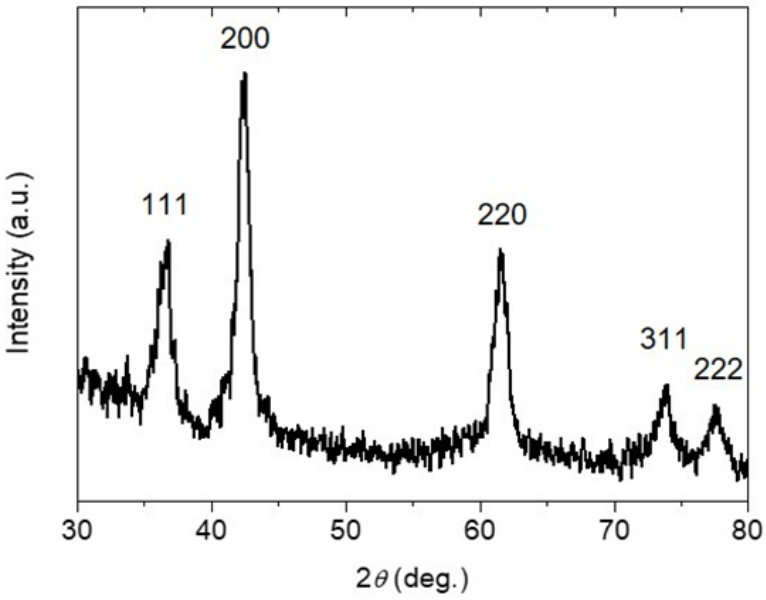

Figure 79. Powder XRD pattern of the three times reused c-$Co_{0.98}Ni_{0.02}O$ MNAs catalyst.

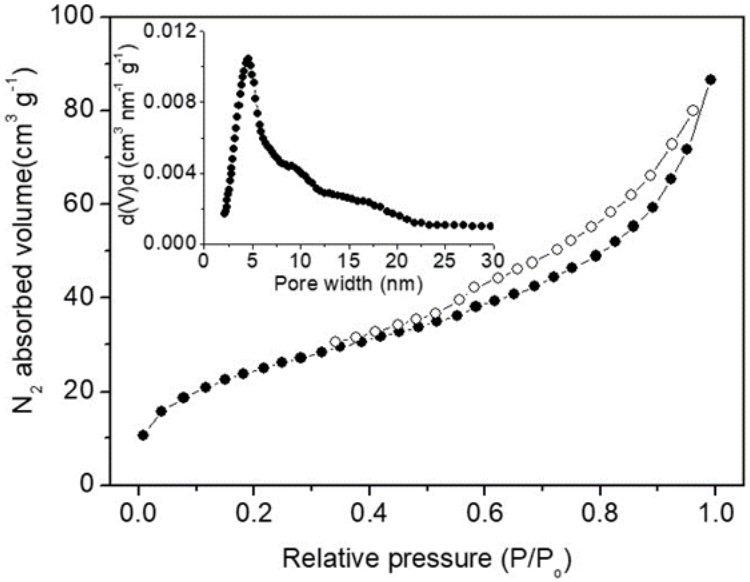

Figure 80. N_2 adsorption-desorption isotherms at –196 ºC (Inset: the corresponding NLDFT pore-size distribution, indicating an average pore size of ~4.6 nm) of the c-$Co_{0.98}Ni_{0.02}O$ MNAs catalyst retrieved after the cycling tests.

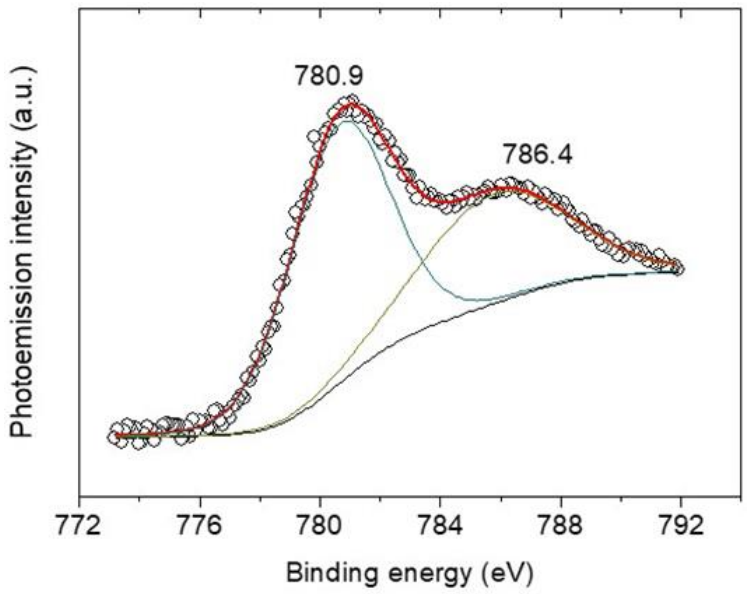

Figure 81. Co $2p_{3/2}$ XPS spectrum of the c-$Co_{0.98}Ni_{0.02}O$ MNAs catalyst obtained after catalysis.

Subsequently, in order to understand the oxidation mechanism of c-$Co_{1-x}Ni_xO$ mesoporous catalysts, photocatalytic reduction of Cr(VI) in an air-tight quartz cell was carried out and the evolved oxygen gas was analyzed by gas chromatography (Shimadzu GC-2014). Before irradiation the solution was purged with argon until oxygen was fully removed (as verified by GC analysis). The results showed that c-$Co_{0.98}Ni_{0.02}O$ MNAs is effective to oxidize water to oxygen, giving an average O_2 evolution rate of ~3.5 μmol h^{-1} after 4 h irradiation (Figure 82). Moreover, to prove that the generation of oxygen is indeed a photoinduced effect, the evolved gas was monitored with an on-line gas analyzer (Hiden HPR-20 QIC). When light on and off conditions were applied to a c-$Co_{0.98}Ni_{0.02}O$ MNAs dispersion (0.3 g L^{-1}) for photocatalytic Cr(VI) reduction, a transient O_2 evolution response was detected, suggesting that the observed photocatalytic Cr(VI) reduction proceeds simultaneously with the water oxidation reaction (Figure 83). Thus, the overall reaction can be described by the following equation:

$$2HCrO_4^- + 8H^+ \rightarrow 2Cr^{3+} + 3/2\ O_2 + 5H_2O \qquad (10)$$

It is noteworthy that the calculated oxygen evolution derived from the Eq. 10 match well with the experimental results (Figure 82). A $HCrO_4^-$ reduction rate of about 5.2 μmol h^{-1} was obtained which based on Eq. 10, consists in a ~3.9 μmol h^{-1} O_2

evolution rate. These results prove that, under UV–visible irradiation, a major fraction of surface-reaching holes is associated with the water oxidation reaction to produce O_2.

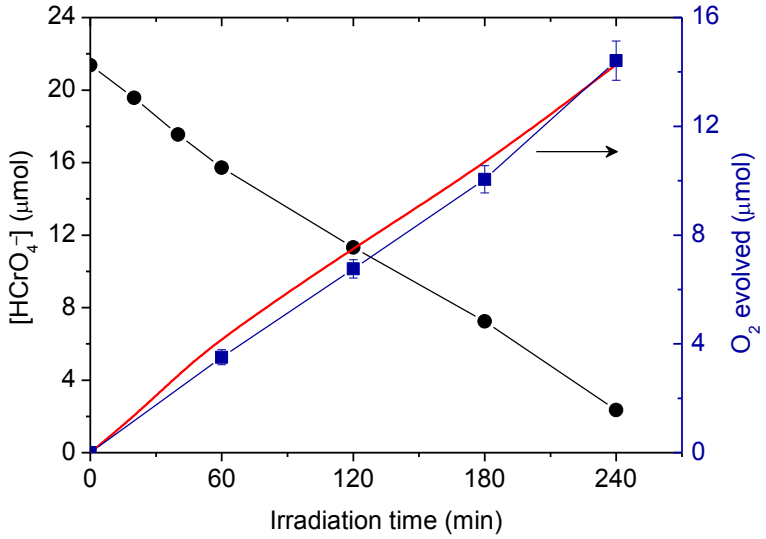

Figure 82. Comparison of photocatalytic Cr(VI) reduction (black) and oxygen evolution (experimental: blue line, calculated from Eq. (10): red line) as a function of irradiation time for c-$Co_{0.98}Ni_{0.02}O$ MNAs catalyst under $\lambda > 360$ nm light irradiation. Reaction conditions: 0.3 g L^{-1} of catalyst, 50 mg L^{-1} Cr(VI) aqueous solution, pH = 2, 20 °C.

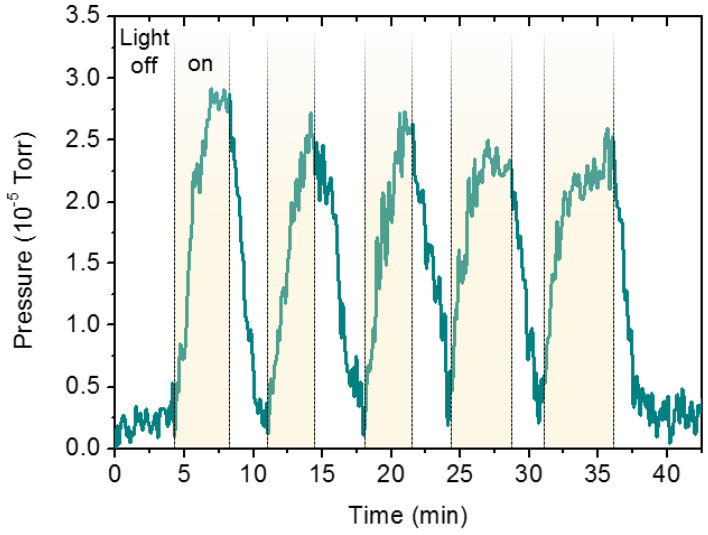

Figure 83. O_2 evolution transient with light on/off for c-$Co_{0.98}Ni_{0.02}O$ MNAs catalyst under $\lambda > 360$ nm light irradiation. Reaction conditions: 0.3 g L^{-1} of catalyst, 50 mg L^{-1} Cr(VI) aqueous solution, pH = 2, 20 °C.

Apart from the oxygen evolution, photooxidation of surface hydroxyl (–OH) groups to hydroxyl radicals (·OH) is a possible option. As it has already been demonstrated, this is a viable process for hexagonal CoO catalyst in the photocatalytic reduction of Cr(VI) [173]. In order to elucidate this possibility, a fluorescence study of the Cr(VI) photocatalytic reduction over c-CoO, c-$Co_{0.98}Ni_{0.02}O$ and c-$Co_{0.98}Cu_{0.02}O$ MNAs catalysts was carried out in the presence of coumarin. It is known that coumarin reacts readily with hydroxyl radicals to produce umbelliferone, which gives a characteristic emission peak at 455 nm upon 332 nm excitation wavelength. The time evolution of the fluorescence of umbelliferone reveals that the production rate of ·OH radicals, which is defined as the ratio of the intensity of umbelliferone to the intensity of coumarin, is comparable between these three materials (Figure 84).

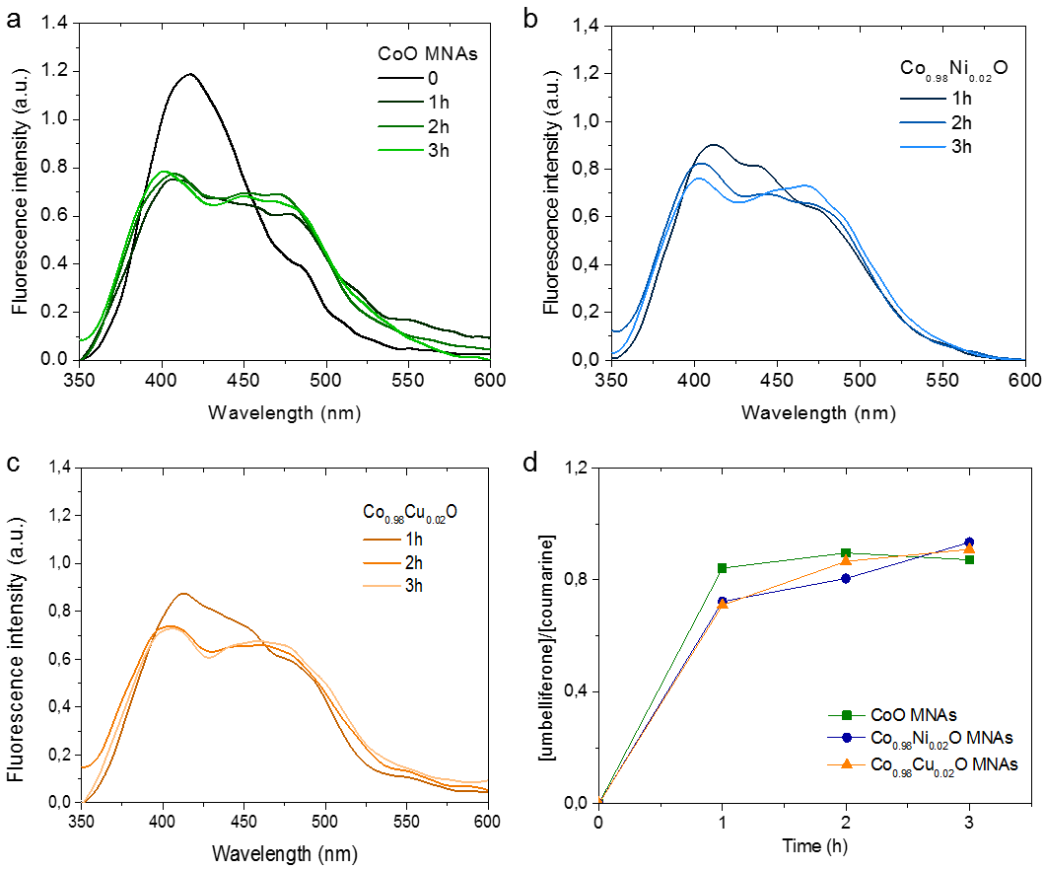

Figure 84. Fluorescence spectra of coumarin (10 mM) in water (pH 2) for (a) c-CoO, (b) c-$Co_{0.98}Ni_{0.02}O$ and (c) c-$Co_{0.98}Cu_{0.02}O$ MNAs catalysts (0.3 g L^{-1}). The emission peaks at ~398 nm and ~455 nm correspond to the coumarin and umbelliferone, respectively. (d) Time evolution of the fluorescence intensity ratio of umbelliferone to coumarine emission for c-CoO, c-$Co_{0.98}Ni_{0.02}O$ and c-$Co_{0.98}Cu_{0.02}O$ MNAs catalysts.

Additionally, the fluorescence signal of umbelliferone does not show obvious intensity increase after 1 h of illumination. Therefore, it is reasonable to conclude that the observed OH_{aq} oxidation process for pure and Ni- and Cu-doped c-CoO MNAs catalysts is minimal and, instead, the oxidation product is almost exclusively oxygen. This is consistent with the O_2 evolution results shown in Figure 82, referred to c-$Co_{0.98}Ni_{0.02}O$ MNAs catalysts.

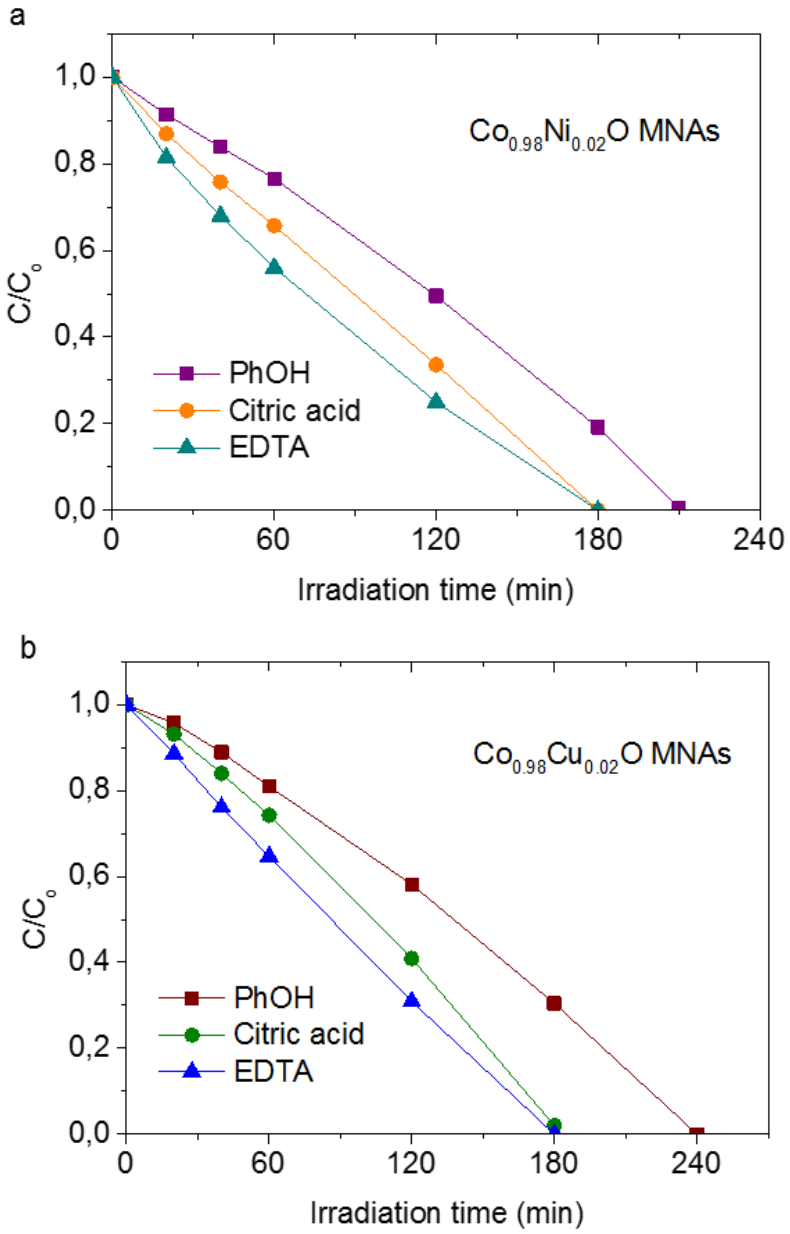

Figure 85. Photocatalytic reduction of aqueous Cr(VI) over (a) c-$Co_{0.98}Ni_{0.02}O$ MNAs and (b) c-$Co_{0.98}Cu_{0.02}O$ MNAs catalyst in the presence of 1 equiv. phenol, citric acid and EDTA. Reaction conditions: 0.3 g L^{-1} catalyst, 50 mg L^{-1} Cr(VI) solution, $\lambda > 360$ nm light, pH = 2, 20 ºC.

The above catalytic results clearly suggest that the four-electron water oxidation process ($2H_2O \rightarrow O_2 + 4H^+ + 4e^-$) at the surface of c-$Co_{1-x}Ni_xO$ and c-$Co_{1-x}Cu_xO$ catalysts dictates the overall reaction rate. As a proof of concept, the Cr(VI) reduction activity of both c-$Co_{0.98}Ni_{0.02}O$ and c-$Co_{0.98}Cu_{0.02}O$ MNAs catalysts is investigated in the presence of phenol, citric acid and EDTA as sacrificial electron donors. Since oxidation of these organic compounds is thermodynamically more favorable than oxidation of water (E_{ox} for phenol, citric acid, EDTA and water is 0.97 V, 1.2 V, 1.17 V and 0.82 V *vs* NHE at pH=7, respectively) [174,175,176], it is anticipated that this process will enhance the kinetics of the Cr(VI) reduction. As expected, the Cr(VI) degradation is significantly increased for Ni and Cu implanted samples with the addition of only 1 equiv. of sacrificial agents (Figure 85). Indeed, in the presence of phenol, a complete conversion to Cr(III) was achieved after 3.5 h and 4 h over c-$Co_{0.98}Ni_{0.02}O$ MNAs and c-$Co_{0.98}Cu_{0.02}O$ MNAs, respectively. In case of citric acid and EDTA the reaction was completed within 3 h for both catalysts.

Assuming that the reaction rate is proportional to the Cr(VI) concentration, the photocatalytic reaction can be described by the first-order kinetics of Langmuir-Hinshelwood model: $\ln(C/C_o) = -kt$, where, C_o and C is the concentration of Cr(VI) at initial time and time t, respectively, and *k* is the apparent reaction rate constant. Thus, kinetic analysis of the temporal evolution of Cr(VI) concentration reveals that the photocatalytic reduction by c-$Co_{0.98}Ni_{0.02}O$ MNAs proceeds at a rate (*k*) of 4.4×10^{-3} min^{-1}, 7.0×10^{-3} min^{-1} and 9.7×10^{-3} min^{-1} with phenol, citric acid and EDTA, respectively (Figure 86). In comparison, an about two to six times lesser reaction rate (1.7×10^{-3} min^{-1}) was observed without sacrificial regent, signifying that presence of organic contaminants to the Cr(VI)-bearing wastewater has an additive effect on improving photocatalytic activity of c-$Co_{1-x}Ni_xO$ MNAs. In case of c-$Co_{0.98}Cu_{0.02}O$ MNAs the photocatalytic reaction proceeds at a rate (*k*) of 3.2×10^{-3} min^{-1}, 4.7×10^{-3} min^{-1} and 7.0×10^{-3} min^{-1} with phenol, citric acid and EDTA, respectively (Figure 87). These results suggest that c-$Co_{0.98}Cu_{0.02}O$ MNAs catalyst achieves about two to four times greater reaction rate than pure CoO MNAs, signifying the photocatalytic enhancement of the doped catalysts.

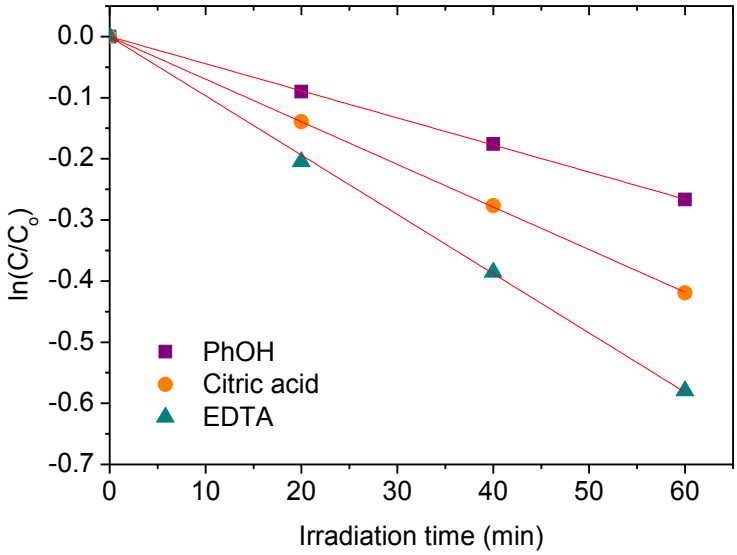

Figure 86. Kinetic profiles over c-$Co_{0.98}Ni_{0.02}O$ MNAs catalyst during photocatalytic reduction of aqueous Cr(VI) in the presence 1 equiv. of phenol, citric acid and EDTA under UV-visible (λ > 360 nm) light irradiation. The red lines are fit to the data.

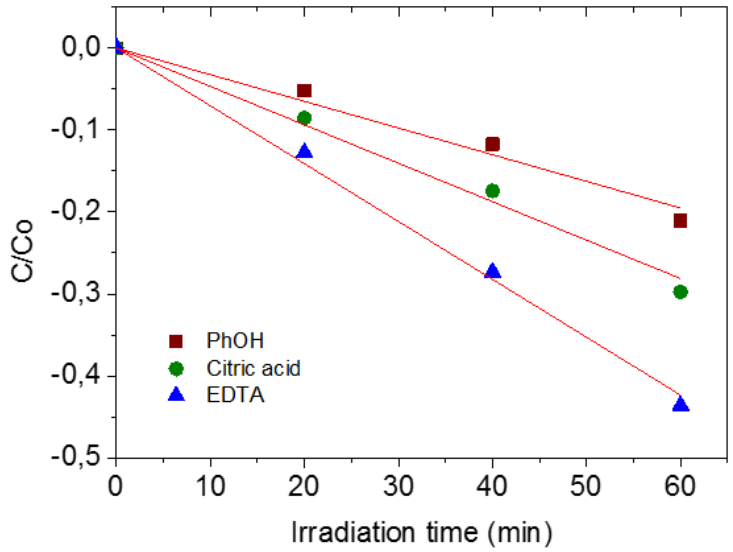

Figure 87. Kinetic profiles over c-$Co_{0.98}Cu_{0.02}O$ MNAs catalyst during photocatalytic reduction of aqueous Cr(VI) in the presence 1 equiv. of phenol, citric acid and EDTA under UV-visible (λ > 360 nm) light irradiation. The red lines are fit to the data.

In order to understand the effect of Ni dopant on the photocatalytic activity of c-CoO, the electrochemical behavior of as-prepared c-$Co_{1-x}Ni_xO$ MNAs materials was delineated with electrochemical impedance spectroscopy (EIS). The resultant

Mott-Schottky plots ($1/C_{SC}^2$ *versus* E) of c-$Co_{1-x}Ni_xO$ MNAs recorded in 0.5 M Na_2SO_4 electrolyte (pH 7) are shown in Figure 88a. Using extrapolation to $1/C_{SC}^2 = 0$, the flat-band potentials (E_{FB}s) calculated for c-$Co_{1-x}Ni_xO$ MNAs were 1.15 (x=0), 1.17 (x=0.01), 1.20 (x=0.02) and 1.22 (x=0.05) V *vs* NHE. Consistent with VB XPS results, the negative slope of the $1/C_{SC}^2$ – E curves indicates the p-type behavior of the catalysts. The anodic shift in E_{FB} for CoO upon Ni doping is due to the formation of Co–O–Ni linkages in implanted c-$Co_{1-x}Ni_xO$ samples. In fact, substitution of Co^{2+} with Ni^{2+} impurity ions can create localized Ni 3d states near the VB maximum, increasing the hole density in the c-$Co_{1-x}Ni_xO$ structure. The presence of these donor states will shift the Fermi level downward, improving the p-type conductivity of c-CoO, as suggested by the VB XPS spectra in Figure 73. This state is also supported by theoretical density functional theory (DFT) calculations shown in Figure 89. For c-CoO in the rocksalt structure (simulated by unit cells of a minimum size of four atoms) the DOS profile near the Fermi level gives an electronic band gap of 2.0 eV. In order to examine the effects of doping, Co atoms were replaced by Ni atoms in the CoO lattice. The DOS plot for c-$Co_{0.5}Ni_{0.5}O$ in Figure 89 shows a small increase of the bandgap by 0.1 eV and an increase of the states close to the band edges by mixing of the O 2p and Co/Ni 3d orbitals. These trends are also confirmed by calculations for smaller Ni concentrations with larger simulation cells (c-$Co_{0.75}Ni_{0.25}O$ and c-$Co_{0.9375}Ni_{0.0625}O$). In consistent with this, the charge density (N_A) of c-$Co_{1-x}Ni_xO$ MNAs, as calculated by the slope of the $1/C_{SC}^2$ – E plots, according to Eq. (11), increases from 3.31×10^{16} to 4.57×10^{16} cm^{-3} with a higher level of nickel doping (Table 3).

$$N_A = 2(E–E_{FB})\cdot C_{sc}^2/\varepsilon\varepsilon_o A^2 q_e \quad (11)$$

where C_{sc} is the space charge capacitance, E is the applied potential, E_{FB} is the flat-band potential, ε is the relative dielectric constant of CoO (13), ε_o is the dielectric permittivity of vacuum (8.8542×10^{-10} F cm^{-1}), A is the area of the electrode and q_e is the elementary charge (1.602×10^{-19} C)

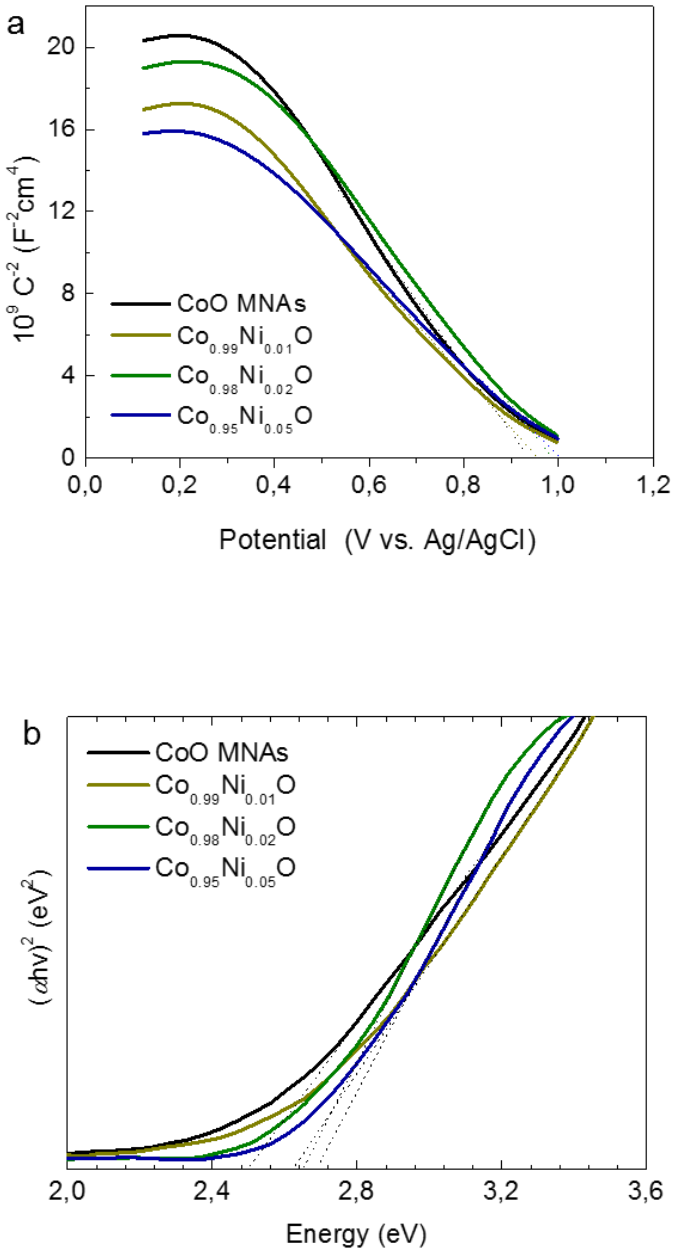

Figure 88. (a) Mott-Schottky plots and (b) Tauc's plots, $(Fhv)^2$ *versus* photon energy, where *F*, h, and v are the Kubelka-Munk function of the reflectance, Plank constant, and light frequency, respectively, of the c-CoO MNAs and c-$Co_{1-x}Ni_xO$ MNAs catalysts.

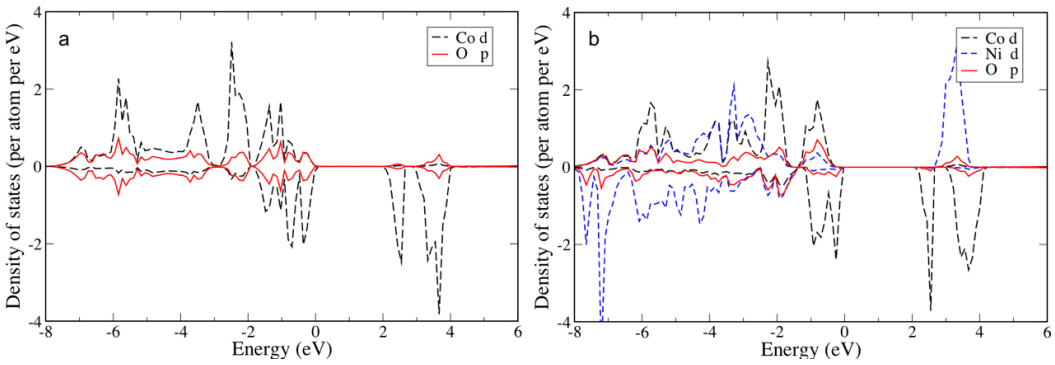

Figure 89. Projected electronic density of states (DOS) for (a) c-CoO and (b) c-$Co_{0.5}Ni_{0.5}O$ rocksalt crystal structures. The DOS profiles near the Fermi level give an energy band gap of 2.0 and 2.1 eV for c-CoO and c-$Co_{0.5}Ni_{0.5}O$ lattice, respectively. DFT+U calculations also show that the valence and conduction band edges of the c-$Co_{0.5}Ni_{0.5}O$ phase are raised by the mixing of the O 2p and Co/Ni 3d orbitals.

Table 3. Electrochemical properties of mesoporous c-$Co_{1-x}Ni_xO$ nanoparticle assemblies (MNAs).

Sample	**Energy gap (eV)**	**E_{FB} (V *vs* NHE, pH=7)**	**E_{CB} (V *vs* NHE, pH=7)**	**Carrier density (N_A, cm^{-3})**
CoO MNAs	2.50	1.15	-1.35	3.31×10^{16}
$Co_{0.99}Ni_{0.01}O$ MNAs	2.63	1.17	-1.46	3.98×10^{16}
$Co_{0.98}Ni_{0.02}O$ MNAs	2.66	1.20	-1.46	3.82×10^{16}
$Co_{0.95}Ni_{0.05}O$ MNAs	2.69	1.22	-1.47	4.57×10^{16}

UV–vis diffuse reflectance spectroscopy is used to obtain optical absorption spectra of c-$Co_{1-x}Ni_xO$ MNAs, from which the E_g was estimated to be 2.50, 2.63, 2.67 and 2.69 eV for c-CoO and Ni-doped samples containing 1%, 2% and 5% Ni, respectively (see Figure 88b and Table 3). In Figure 90, the energy band diagram for each c-$Co_{1-x}Ni_xO$ MNAs catalyst is illustrated. For heavily p-doped semiconductors such as c-CoO, it is quite reasonable to assume that the E_{FB} level lies very close to the VB edge. Thus, the position of conduction band (CB) could be obtained according to the equation of $E_{CB} = E_{FB} + E_g$, and the results are shown in Table 3. As shown in Figure 90, while a small perturbation of the CB edge is observed, the VB edge position of c-$Co_{1-x}Ni_xO$ MNAs is gradually shifted to higher potentials with increasing Ni doping, making them better electron acceptors for water oxidation, thus signifying superior photocatalytic Cr(VI) reduction kinetics.

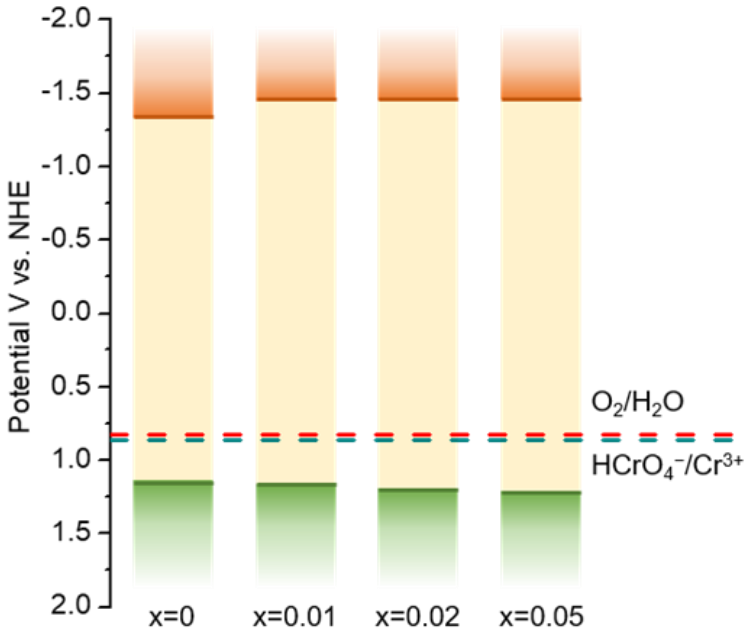

Figure 90. Energy band diagrams of the c-$Co_{1-x}Ni_xO$ MNAs (Green line: valence band maximum, orange line: conduction band minimum). The reduction potentials of water and $HCrO_4^-$ species are also given.

In addition, from EIS measurements and Nyquist Plots, it was received information about the charge-transfer resistance (R_{ct}) for each catalyst (Figure 91). The equivalent circuit model R_s (Q_f/($R_{ct}L_{ad}$)Q_2) (inset of Figure 91) was used to simulate the EIS curve of the fabricated c-$Co_{1-x}Ni_xO$ (x = 0–0.05) MNAs electrodes. R_s represent the electrolyte resistance, R_{ct} is the charge-transfer resistance, Q_f and Q_2 elements account for the defect resistance (pores, cracks and grain boundaries) of the solid film and the double layer capacitance, respectively. In addition, an inductor (L_{ad}) to the proposed circuit model, which account for the pseudo-inductive behaviour in the high frequency domain (often causing by disordered charge-carrier relaxation and disordered movement of redox species at the sur face of electrode) [177,178], was also necessary for fitting the experimental results. The results in Table 4 clearly show that the Ni-doped samples produce a lower R_{ct} than pure c-CoO MNAs does; a R_{ct} of 103.8, 100.7, 100.5 and 99.8 Ω is obtained for pure and 1%, 2% and 5% Ni implanted c-CoO MNAs. These findings affirm a better charge carrier conductivity for Ni-implanted catalysts, which

correlates well with their high Cr(VI) photocatalytic reduction activity. Hence, the higher performance of c-$Co_{0.98}N_{0.02}O$ assemblies can be attributed to the enhanced charge transfer and oxidative ability of surface-reaching holes. In line with this, the $Co_{0.98}N_{0.02}O$ MNAs sample demonstrated a higher mobility of the photogenerated carriers according to the photocurrent density (J_{ph}) measurements. In particular, the J_{ph} for $Co_{1-x}Ni_xO$ MNAs catalysts was estimated to be 9.52 (x=0), 11.01 (x=0.01), 19.89 (x=0.02) and 14.36 (x=0.05) mA cm^{-2} under 420–760 nm irradiation at 1 V applied bias, which can be interpreted as a result of the depressed recombination of photoinduced electron-hole pairs.

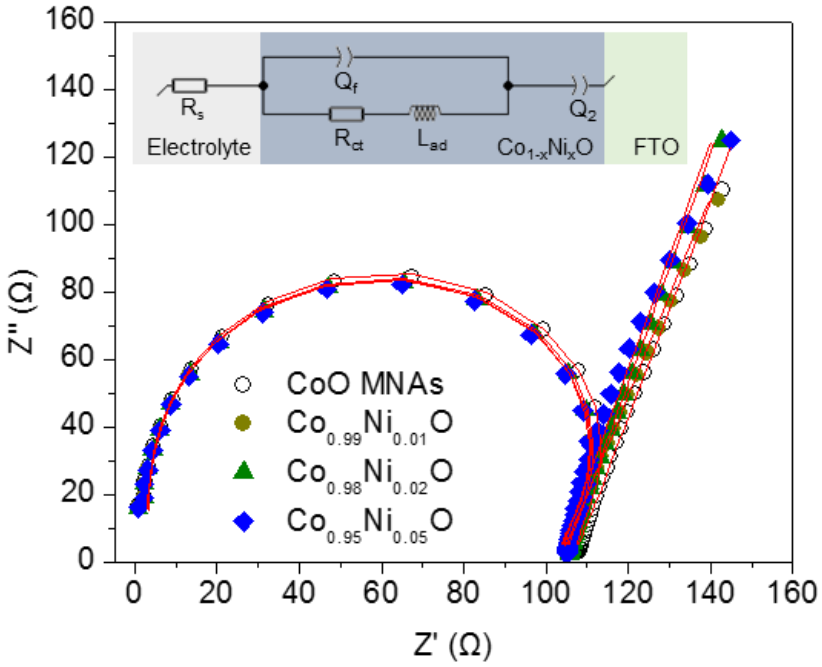

Figure 91. Nyquist plots of the c-$Co_{1-x}Ni_xO$ MNAs catalysts.

Table 4. EIS equivalent circuit fitted parameters of pure and Ni-doped c-CoO MNAs catalysts.

Sample	**R_s (Ω)**	**Q_f (F)**	**L_{ad} (H)**	**R_{ct} (Ω)**	**Q_2 (F)**	**x^2**
CoO MNAs	2.94	10.41×10^{-9}	74.04×10^{-6}	103.8	42.70×10^{-6}	1.5×10^{-3}
$Co_{0.99}Ni_{0.01}O$ MNAs	3.05	10.77×10^{-10}	73.20×10^{-7}	100.7	51.78×10^{-7}	2.3×10^{-4}
$Co_{0.92}Ni_{0.02}O$ MNAs	3.18	10.76×10^{-11}	73.55×10^{-8}	100.5	39.82×10^{-8}	3.4×10^{-5}
$Co_{0.95}Ni_{0.05}O$ MNAs	3.08	10.82×10^{-12}	73.53×10^{-9}	99.8	36.00×10^{-9}	3.6×10^{-6}

Electrochemical impedance spectroscopy measurements were also carried out for c-$Co_{1-x}Cu_xO$ MNAs catalysts, in order to evaluate their lower efficiency in photocatalytic reduction of Cr(VI) compared to Ni dopant materials. The resultant Mott-Schottky plots ($1/C_{SC}^2$ *versus* E) recorded in 0.5 M Na_2SO_4 electrolyte (pH 7) are shown in Figure 92a. Using extrapolation to $1/C_{SC}^2 = 0$, the flat-band potentials (E_{FB}s) calculated for c-$Co_{1-x}Cu_xO$ MNAs samples were 0.78 (x=0.01), 0.79 (x=0.02) and 0.82 (x=0.05) V *vs* NHE. The charge density (N_A) of these catalysts deduced from the slope of the $1/C_{SC}^2$ – E plots according to Eq. (11), range between 6.53×10^{15} and 8.89×10^{15} cm^{-3}. It should be noted that the negative slope of the $1/C_{SC}^2$–E curves indicates p-type behavior for the c-$Co_{1-x}Cu_xO$ MNAs materials.

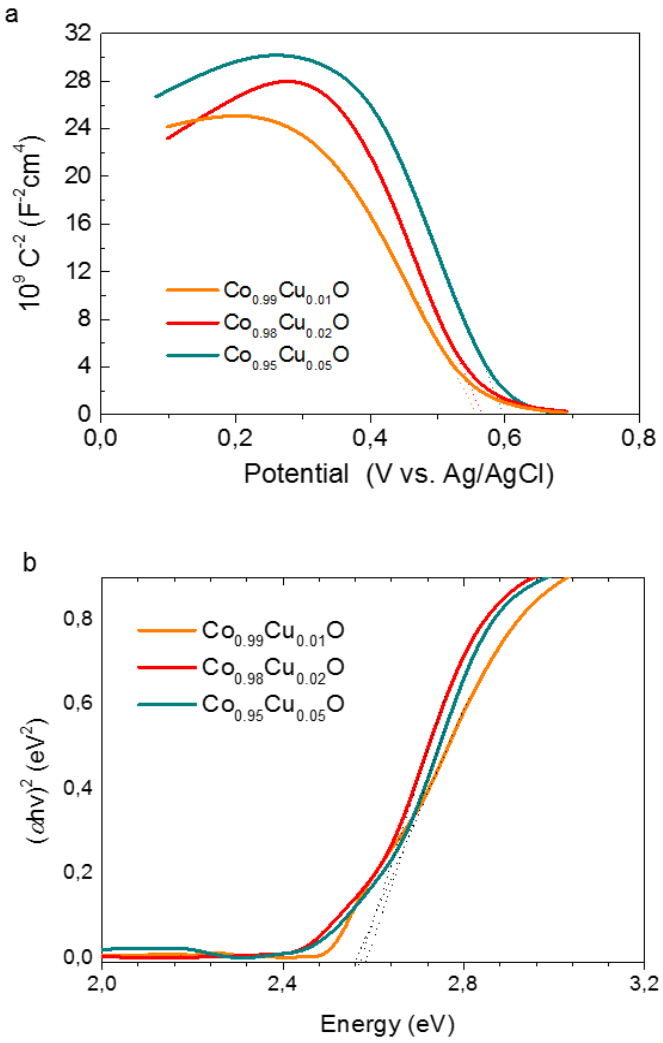

Figure 92. (a) Mott-Schottky plots and (b) Tauc's plots, $(Fhv)^2$ *versus* photon energy, where *F*, h, and v are the Kubelka-Munk function of the reflectance, Plank constant, and light frequency, respectively of the c-$Co_{1-x}Cu_xO$ MNAs catalysts.

The electronic structure of the c-$Co_{1-x}Cu_xO$ MNAs was investigated with UV–vis diffuse reflectance spectroscopy, from which the energy band gap was estimated to be 2.54, 2.55 and 2.58 eV for x = 0.01, 0.02 and 0.05 Cu-doped materials, respectively (see Figure 92b and Table 5). In Figure 93, the energy band diagram for each catalyst is illustrated, which was deduced in a similar way as for p-type c-$Co_{1-x}Ni_xO$ MNAs using the equation $E_{CB} = E_{FB} + E_g$. The results show that the CB edge position of the Cu implanted samples shifts to a more negative values, reflecting a higher ability of photoexcited electrons for Cr(VI) reduction compared to the pure c-CoO MNAs. On the other hand, the VB edges state very close to the thermodynamic O_2 evolution potential (0.81 *vs* NHE, pH = 7) and, therefore, it is possible a major portion of photogenerated holes to be lost by electrons at the surface of the catalyst. This behavior could result in lower photocatalytic activity of c-$Co_{1-x}Cu_xO$ MNAs compared to c-$Co_{1-x}Ni_xO$ MNAs catalysts, taking into consideration that oxidation process is the rate-controlled step in the Cr(VI) photocatalytic reduction by the CoO-based catalysts.

Table 5. Electrochemical properties of mesoporous c-$Co_{1-x}Cu_xO$ nanoparticle assemblies.

Sample	**Energy gap (eV)**	**E_{FB} (V *vs* NHE, pH=7)**	**E_{CB} (V *vs* NHE, pH=7)**	**Carrier density (N_A, cm^{-3})**
$Co_{0.99}Cu_{0.01}O$ MNAs	2.54	0.78	-1.76	8.89×10^{15}
$Co_{0.98}Cu_{0.02}O$ MNAs	2.55	0.79	-1.76	6.53×10^{15}
$Co_{0.95}Cu_{0.05}O$ MNAs	2.58	0.82	-1.76	7.35×10^{15}

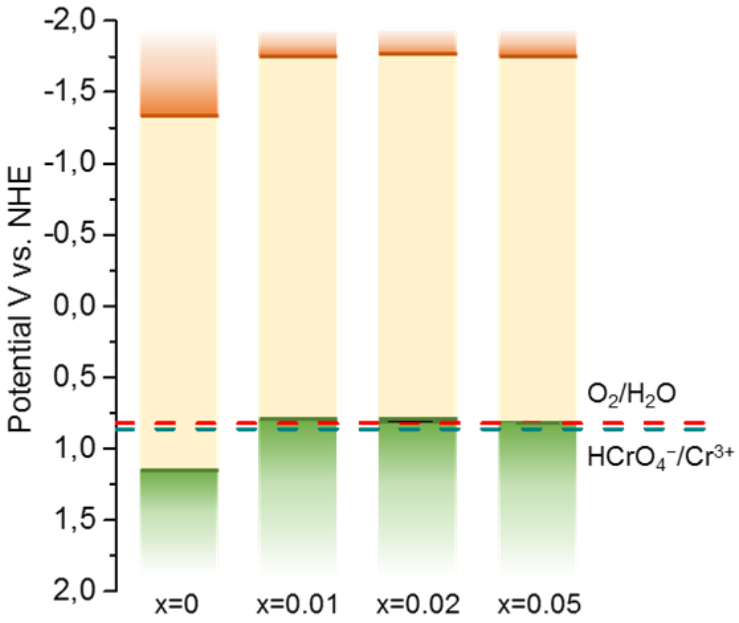

Figure 93. Energy band diagrams of the c-$Co_{1-x}Cu_xO$ MNAs (Green line: valence band maximum, orange line: conduction band minimum). The reduction potentials of water and $HCrO_4^-$ species are also given.

Also, further information about the charge-transfer resistance (R_{ct}) of c-$Co_{1-x}Cu_xO$ MNAs were received by EIS measurements and Nyquist Plots (Figure 94). An equivalent circuit model similar to that used for c-$Co_{1-x}Ni_xO$ MNAs samples was utilized to simulate the EIS data (inset of Figure 94). From Table 6, it is obvious that the c-$Co_{1-x}Cu_xO$ MNAs materials exhibit higher R_{ct} than that of Ni-doped catalysts; we calculated a R_{ct} of 102.4 Ω, 103.8 Ω and 117.9 Ω for x = 0.01, 0.02 and 0.05 Cu-doped samples. These results clearly suggest a lower charge carrier conductivity in c-$Co_{1-x}Cu_xO$ implanted structures. Therefore, taking into consideration all the above findings, our results suggest that the lower photocatalytic Cr(VI) reduction activity of c-$Co_{1-x}Cu_xO$ MNAs compared to the c-$Co_{1-x}Ni_xO$ MNAs catalysts is due to the low oxidative ability of the photogenerated holes and the high charge-transfer resistance of c-$Co_{1-x}Cu_xO$ assemblies.

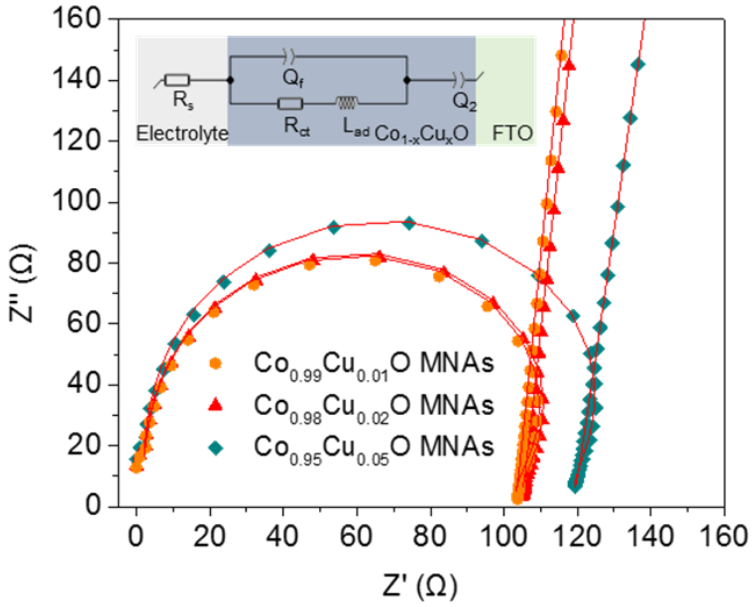

Figure 94. Nyquist plots of the c-$Co_{1-x}Cu_xO$ MNAs catalysts.

Table 6. EIS equivalent circuit fitted parameters of Cu-doped CoO MNAs catalysts.

Sample	**R_s (Ω)**	**Q_f (F)**	**L_{ad} (H)**	**R_{ct} (Ω)**	**Q_2 (F)**	**x^2**
$Co_{0.99}Cu_{0.01}O$ MNAs	1.14	16.75×10^{-9}	80.8×10^{-6}	102.4	10.0×10^{-8}	1.9×10^{-3}
$Co_{0.98}Cu_{0.02}O$ MNAs	1.16	16.0×10^{-9}	80.2×10^{-6}	103.8	7.1×10^{-6}	4.5×10^{-4}
$Co_{0.95}Cu_{0.05}O$ MNAs	1.16	13.1×10^{-9}	88.5×10^{-6}	117.9	10.6×10^{-6}	5.6×10^{-4}

4

Conclusions

To sum up, this work shows that it is feasible to create mesoporous networks of Cu nanoparticles decorated with graphite (G) layers through a polymer-assisted *in-situ* reduction and aggregating self-assembly of CuO nanoparticles. Importantly, this synthetic route seems particularly suitable to construct Cu/G assemblies with novel integrations of properties, such as tunable mesoporosity and plasmonic activity. The large surface area of the porous framework of assembled Cu/G nanoparticles (BET surface area ~ 90 m^2 g^{-1}) exposes essentially a number of plasmonic sites to incoming molecules, so that a significant SERS enhancement becomes obvious (Cu/G NPAs attain an EF of ~ 3.9×10^6 for R6G detection). Moreover, the network structure of these materials shows a similar SERS activity across different spot areas with high reproducibility, as well as sufficient chemical stability after exposure to air. These results demonstrate Cu/G assemblies as a highly efficient cost-effective and stable substrate for SERS detection. The present approach can provide a generic synthetic pathway for the rational design and fabrication of other porous networks of graphite-decorated metal nanoparticles (such as Ag, Co, and Ni). Such hybrid porous nanostructures may enable low-cost catalysts, chemical sensors and photonic devices.

Additionally, high-surface-area mesoporous networks of linked hexagonal CoO nanoparticles (h-CoO MNAs) were also successfully synthesized via a polymer-assisted co-assembly of colloidal h-CoO nanoparticles and amphiphilic block-copolymer aggregates. These newly developed materials show an open-pore structure (BET surface area ~ 96 m^2 g^{-1}) consisting of tightly bonded nanoparticles with an average diameter of 18 nm and manifest excellent photocatalytic performance for reduction of Cr(VI) in aqueous solutions. Results indicated that the unprecedented photocatalytic activity of h-CoO MNAs catalyst is presumably a result of the combined effect of accessible pore volume, appropriate band edge

positions and specific reactivity of the crystal phase. Control catalytic experiments coupled with on-line mass spectrometry and fluorescence spectroscopy confirmed that the Cr(VI) reduction reaction proceeds simultaneously with the competitive formation of molecular oxygen and hydroxyl radicals (·OH) at the h-CoO surface. Indeed, hexagonal CoO nanoparticles favor the oxidation half reaction through a localized-hole-mediated ·OH radical production mechanism, accelerating the reduction of Cr(VI). The remarkable activity and durability of the h-CoO MNAs implies the great possibility of implementing this new catalyst into a realistic Cr(VI) detoxification of contaminated water.

Finally, high-surface-area Ni-doped and Cu-doped cubic-phased CoO nanoparticle assemblies (c-$Co_{1-x}Ni_xO$ MNAs and c-$Co_{1-x}Cu_xO$ MNAs) have been successfully prepared by a polymer-assisted self-assembly method, and were used as photocatalysts for the detoxification of Cr(VI) aqueous solutions. Comparatively to the c-$Co_{1-x}Cu_xO$ MNAs, c-$Co_{1-x}Ni_xO$ MNAs with an optimal atomic ratio (2%) of Ni perform higher Cr(VI) photocatalytic reduction and water oxidation activity with a 1.5% AQY at 375 nm, while demonstrating remarkable stability, outperforming previous results. Mechanistic studies with XPS, UV–vis, fluorescence, EIS experiments and theoretical (DFT) calculations reveal that Ni doping of c-CoO effectively improves the charge-transfer process and oxidation efficiency of surface-reaching holes for water oxidation. Such Ni-implanted CoO nanoparticle assemblies manifest improved photochemical properties and demonstrate good possibilities for widespread uses in photocatalysis and environmental remediation.

References

[1] A. Taguchi, F. Schüth, *Micropor. Mesopor. Mater.*, **2005**, *77*, 1–45.

[2] S. M. Zhu, H. S. Zhou, T. Miyoshi, M. Hibino, I. Honma and M. Ichihara, *Adv. Mater*., **2004**, *16*, 2012–2017.

[3] A. Y. Khodakov, A. Griboval-Constant, R. Bechara ,V. L. Zholobenko, *J. Catal.*, **2002**, *206*, 230–241.

[4] Y. J. Han, G. D. Stucky and A. Butler, *J. Am. Chem. Soc.*, **1999**, *121*, 9897–9898.

[5] K.S.W. Sing, D.H. Everett, R.A.W. Haul, L. Moscou, R.A. Pierotti, J. Rouquerol, T. Siemieniewska, *Pure Appl. Chem.*, **1985**, *57*, 603–619.

[6] L. Zhao, H. Qin, R. Wu, H. Zou, *Journal of Chromatography A*, **2012**, *1228*, 193–204.

[7] C.T. Kresge, M. E. Leonowicz, W. J. Roth, J. C. Vartuli, J. S. Beck, *Nature*, **1992**, *359*, 710–712.

[8] N. Pal, A. Bhaumik, *Adv. Coll. Inter. Sci*, **2013**, *189–190*, 21–41.

[9] J. S. Beck, J. C. Vartuli, W. J. Roth, M. E. Leonowicz, C. T. Kresge, K. D. Schmitt, C. T. W. Chu, D. H. Olson, E. W. Sheppard, *J. Am. Chem. Soc*., **1992**, *114*, 10834–10843.

[10] M. Janicke, D. Kumar, G.D. Stucky, B.F. Chmelka, *Stud. Surf. Sci. Catal.* **1994**, *84*, 243.

[11] P. Van der Voort, M. Baltes, E.F. Vansant, *Catal. Today*, **2001**, *68*, 119–128.

[12] A. Corma, M.T. Navarro, J. Perez-Pariente, *J. Chem. Soc. Chem. Commun*., **1994**, 147–148.

[13] M. Hartmann, S. Racouchot, C. Biscof, *Micropor. Mesopor. Mater.*, **1999**, *27*, 309–320.

[14] J.F. Diaz, K.J. Balkus, F. Bedioui, V. Kurshev, L. Kevan, *Chem. Mater.* **1997**, *9*, 61–67.

[15] S. Koner, K. Chaudhari, T.K. Das, S. Sivasanker, *J. Mol. Catal. A: Chemical*, **1999**, *150*, 295–297.

[16] D. Grosso, C. Boissière, B. Smarsly, T. Brezesinski, N. Pinna, P. A. Albouy, H. Amenitsch, M. Antonietti, C. Sanchez, *Nature Mater*., **2004**, *3*, 787–792.

[17] P. Yang, D. Zhao, D.I. Margolese, B.F. Chmelka, G.D. Stucky, *Chem. Mater.*, **1999**, *11*, 2813–2826.

[18] F. Schüth, W. Schmidt, *Adv. Engin. Mater*., **2002**, *4*, 269–279.

[19] C. Garcia, Y.M. Zhang, F. DiSalvo, U. Wiesner, *Angew. Chem. Int. Ed*. **2003**, *42*, 1526–1530.

[20] P. Yang, D. Zhao, D.I. Margolese, B.F. Chmelka, G.D. Stucky. *Nature*, **1998**, *396*, 152–155.

[21] J.C. Colmenares, R. Luque, *Chemical Society Reviews*, **2014**, *43*, 765–778.

[22] S. N. Ahmed, W. Haider, *Nanotechnology*, **2018**, *29*, 34.

[23] L.Yuan, Y.J. Xu, *Applied Surface* Science, **2015**, *342*, 154–167.

[24] C.Wang, D. Astruc, *Chemical Society Reviews*, **2014**, *43*, 7188–7216.

[25] A. M. Smith, S. Nie, *Acc. Chem. Res.*, **2010**, *43*, 190–200.

[26] G. Rothenberger, J. Moser, M. Graetzel, N. Serpone, D. K. Sharma, *J. Am. Chem. Soc.*, **1985**, *107*, 8054–8059.

[27] X. Zhang, Y. L. Chen, R.-S. Liu, D. P. Tsai, *Rep. Prog. Phys.*, **2013**, *76*, 046401.

[28] S. Ghosh, Chapter in *Visible-Light-Active Photocatalysis: Nanostructured Catalyst Design, Mechanisms, and Applications*., **2018**, John Wiley & Sons.

[29] O. Ola, M.M. Maroto-Valer, *Journal of Photochemistry and Photobiology C: Photochemistry Reviews*, **2015**, *24*, 16–42.

[30] J. Highfield, *Molecules*, **2015**, *20*, 6739–6793.

[31] A.W. Bott, *Current Separations*, **1998**, *17:3*, 87–92.

[32] D. Chen, A.K. Ray, *Chem Eng Sci*, **2001**, *56*, 1561–1570

[33] M. Trojanowicz, Main concepts of chemical sensing. Chapter, in: R. Potyrailo, V. Mirsky (Eds.), Combinatorial methods for chemical and biological sensors, Springer (2009), pp. 25-60.

[34] J. Liu, K. Huang, K. Xie, Y. Yang, H. Liu, *Water Research*, **2016**, *93*, 187–194

[35] L.B. Khalil, W.E. Mourad, M.W. Rophael, *Appl. Catal. B*, **1998**, *17*, 267–273

[36] A.D. Bokare, W. Choi, *J Environ. Sci. Technol*., **2010**, 44, 7232–7237.

[37] L. Levankumar, V. Muthukumaran and M. B. Gobinath, J. Hazard. Mater. 161 (2009) 709–713.

[38] G. Gollavelli, C.-C. Chang, Y.-C. Ling, *ACS Sustainable Chem. Eng.*, **2013**, *1*, 462–472.

[39] S.A. Katz, H.J. Salem, *Appl. Toxicol*., **1993**, *13*, 217–224.

[40] S. Peyrav, R. Zahiri, K.M. Hersini, *J. Chem. Health Risks*, **2011**, 1, 11–18.

[41] United States Environmental Protection Agency (U.S. EPA), **2010**. IRIS Toxicological Review of Hexavalent Chromium (External Review Draft). U.S. Environmental Protection Agency, Washington, DC, EPA/635/R-10/004A.

[42] C.E. Barrera-Diaz, V. Lugo-Lugo, B. Bilyeu, *J. Hazard. Mater.*, **2012**, *223–224*, 1–12.

[43] Y. Tian, L. Huang, X. Zhou, C. Wu, J. Hazard. Mater., **2012**, *225−226,* 15−20.

[44] A. Lu, S. Zhong, J. Chen, J. Shi, J. Tang, X. Lu, *Environ. Sci. Technol.*, **2006**, *40*, 3064−3069.

[45] C.E. Barrera-Díaz, V. Lugo-Lugo, B. Bilyeu, *J Hazard Mater*., **2012, (***223-224)*, 1–12.

[46] S. W. Hu, L. W. Yang, Y. Tian, X. L. Wei, J. W. Ding, J. X. Zhong, P.K. Chu, *Appl. Catal. B: Environ.*,**2015**, *163*, 611–622.

[47] S. Cao, J. Low, J. Yu, M. Jaroniec, *Adv. Mater*. , **2015**, *27*, 2150–2176.

[48] Q. Wang, X. Shi, E.Liu, J. C.Crittenden, X.Ma, Y.Zhang, Y. Cong, *J. Hazard. Mater*, **2016**, *317*, 8–16.

[49] B. Sun, E.P. Reddy, P. G. Smirniotis, *Environ. Sci. Technol*. **2005**, *39*, 6251–6259.

[50] Y. Li, W. Cui, L. Liu, R. Zong, W. Yao, Y. Liang, Y. Zhu, *Appl. Catal. B: Environ*. 2016, *199*, 412–423.

[51] J. Shang, W. Hao, X. Lv, T. Wang, X. Wang, Y. Du, S. Dou, T. Xie, D. Wang, J. Wang, *ACS Catal.*, **2014**, *4*, 954−961.

[52] Q. Cheng, C. Wang, K. Doudrick, C.K. Chan, *Appl. Catal. B: Environ*., **2015**, *740*, 176–177.

[53] Y.C. Zhang, J. Li, M. Zhang, D.D. Dionysiou, *Environ. Sci. Technol.*, **2011**, *45*, 9324–9331.

[54] W. Yang, L. Zhang, Y. Hu, Y. Zhong, H. B. Wu, X. W. Lou, *Angew. Chem. Int.* **2012**, *51*, 11501–11504.

[55] X. Liu, L. Pan, T. Lv, G. Zhu, Z. Suna, C. Sun, *Chem. Commun*. **2011**, *47*, 11984–11986.

[56] H. Abdullah, D.-H. Kuo, ACS *Appl. Mater. Interfaces*, **2015**, *7*, 26941−26951.

[57] G. Dong, L. Zhang, *J. Phys. Chem. C*, **2013**, *117*, 4062–4068.

[58] G. Chen, M. Sun, Q. Wei, Z. Ma, B. Du, *Appl. Catal. B: Environ*., **2012**, *125*, 282–287.

[59] R. Nakamura, T. Okamura, N. Ohashi, A. Imanishi, Y. Nakato, *J. Am. Chem. Soc.*, **2005**, *127*, 12975–12983.

[60] J. F. Liu, S. Yin, H. P. Wu, Y. W. Zeng, X. R. Hu, Y. W. Wang, G. L. Lv, J. Z. Jiang, *J Phys Chem B*, **2006**, *110*, 21588–21592.

[61] H. Jiang, R.I. Gomez-Abal, P. Rinke, M. Scheffler, Phys. Rev. B: Condens. *Matter Mater. Phys*. **2010**, *82*, 045108.

[62] W.-Y. Li, L.-N. Xu, J. Chen, *Adv. Funct. Mater*. **2005**, *15*, 851–857.

63 P. Poizot, S. Laruelle, S. Grugeon, L. Dupont, J.-M. Tarascon, *Nature*, **2000**, *407*, 496–499.

64 X. He, W. Zhong, S. Yan, C. Liu, H. Shi, C.-T. Au, Y. Du, *J. Phys. Chem. C.* **2014**, *118*, 13898–13903.

[65] K.M. Nam, Y.C. Choi, S.C. Jung, Y.-I. Kim, M. R. Jo, S. H. Park, Y.-M. Kang, Y.-K. Han, J.T. Park, *Nanoscale*, **2012**, 4, 473–477.

[66] Chen, C.-C., Herhold, A. B., Johnson, C. S., Alivisatos, A. P. *Science*, **1997**, *276*, 398–401.

[67] Dinega, D. P., Bawendi, M. G. *Angew. Chem. Int. Ed*. **1999**, *38*, 1788–1791.

[68] Sakurai, S., Namai, A., Hashimoto, K., Ohkoshi, S.-I. *J. Am. Chem. Soc*., **2009**, *131*, 18299–18303.

[69] Sun, Y., Mayers,B., Xia, Y., *Adv.Mater*., **2003**, *15*, 641–646.

[70] K. M. Nam, W. S. Seo, H. Song, J. T. Park, *NPG Asia Materials*, **2017**, *9*, 364.

[71] G. Margaris, K. N. Trohidou, J. Nogués, *Adv. Mater.*, **2012**, *24*, 4331–4336.

[72] L. Liao, Q. Zhang, Z. Su, Z. Zhao, Y. Wang, Y. Li, X. Lu, D. Wei, G. Feng, Q. Yu, X. Cai, J. Zhao, Z. Ren, H. Fang, F. Robles-Hernandez, S. Baldelli, J. Bao, *Nat. Nanotechnology*, **2014**, *9*, 69–73.

[73] S. Nie, S. R. Emory, *Science* **1997**, *275*, 1102–1106.

[74] K. Kim, H. S. Han, I. Choi, C. Lee, S. Hong, S. Suh, L. P. Lee, T. Kang, *Nat. Commun*. **2012**, *4*, 2182.

[75] Y. Wang, B. Yan, L. Chen, *Chem. Rev.* **2013**, *113*, 1391–1428.

[76] D. Lin, T. Qin, Y. Wang, X. Sun, L. Chen, *ACS Appl. Mater. Interfaces* **2014**, ***6***, 1320–1329

[77] N. C. Bigall, M. Reitzig, W. Naumann, P. Simon, K.-H. Van Pée, A. Eychmüller, *Angew. Chem. Int. Ed.* **2008**, *47*, 7876–7879.

[78] M. B. Gawande, A. Goswami, F.-X. Felpin, T. Asefa, X. Huang, R. Silva, X. Zou, R. Zboril, R. S. Varma, *Chem. Rev.* **2016**, *116*, 3722–3811.

[79] S. E. Allen, R. R. Walvoord, R. Padilla-Salinas, M. C. Kozlowski, *Chem. Rev.* **2013**, *113*, 6234–6458.

[80] G. H. Chan, J. Zhao, E. M. Hicks, G. C. Schatz, R. P. V. Duyne, *Nano Lett.* **2007**, *7*, 1947–1952.

[81] J. Rickerby, J. H. G. Steinke, *Chem. Rev.* **2002**, *102*, 1525–1550.

[82] J. L. Cuya Huaman, K. Sato, S. Kurita, T. Matsumotoc, B. Jeyadevan, *J. Mater. Chem.*, **2011**, *21*, 7062

[83] C. Barrière, K. Piettre, V. Latour, O. Margeat, C.-O. Turrin, B. Chaudret, P. Fau, *J. Mater. Chem*., **2012**, *22*, 2279.

[84] K. P. Rice, E. J. Walker, M. P. Stoykovich, A. E. Saunders, *J. Phys. Chem. C* **2011**, *115*, 1793–1799.

[85] R. J. White, R. Luque, V. L. Budarin, J. H. Clark, D. J. Macquarrie, *Chem. Soc. Rev.* **2009**, *38*, 481–494.

[86] Z. J. Wang, S. X. Wu, J. Zhang, P. Chen, G. C. Yang, X. Z. Zhou, Q. Zhang, Q. Yan, H. Zhang, *Nanoscale Res. Lett.* **2012**, *7*, 161–167.

[87] Z. Y. Yin, Q. Y. He, X. Huang, J. Zhang, S. X. Wu, P. Chen, G. Lu, P. Chen, Q. Zhang, Q. Y. Yan, H. Zhang, *Nanoscale* **2012**, *4*, 293–297.

[88] X. Guo, C. Hao, G. Jin, H. Y. Zhu, X. Y. Guo. *Angew. Chem. Int. Ed.* **2014**, *53*, 1973–1977.

[89] P. Mondal, A. Sinha, N. Salam, A. S. Roy, N. R. Jana, S. M. Islam, *RSC Adv.* **2013**, *3*, 5615–5623.

[90] X. Zhang, C. Shi, E. Liu, J. Li, N. Zhao, C. He, *Nanoscale* **2015**, *7*, 17079–17087.

[91] C. Gonzalez-Arellano, A. M. Balu, R. Luque, D. J. Macquarrie, *Green Chem*. **2010**, *12*, 1995–2002.

[92] M. B. Thathagar, J. Beckers, G. Rothenberg, *J. Am. Chem. Soc*. **2002**, *124*, 11858–11859.

[93] A. Honraedt, F. L. Callonnec, E. L. Grognec, V. Fernandez, F.-X. Felpin, *J. Org. Chem*. **2013**, *78*, 4604–4609.

[94] P. Mondal, A. Sinha, N. Salam, A. S. Roy, N. R. Jana, S. M. Islam, *RSC Adv*. **2013**, *3*, 5615–5623.

[95] S. Frindy, A. E. Kadib, M. Lahcini, A. Primo, *ACS Catal*. **2016**, *6*, 3863–3869.

[96] A. Dhakshinamoorthy, S. Navalon, D. Sempere, M. Alvaro, H. Garcia, *ChemCatChem* **2013**, *5*, 241–246.

[97] O. Benson, *Nature* **2011**, *480*, 193–199.

[98] W. Xu, X. Ling, J. Xiao, M. S. Dresselhaus, J. Kong, H. Xu, Z. Liu, J. Zhang, *PNAS*, **2012**, *109*, 9281–9286.

[99] L. Jensen, C. M. Aikens, G. C. Schatzc, *Chem. Soc. Rev*, **2008**, *37*, 1061–1073.

[100] X. Zhang, C. Shi, E. Liu, J. Li, N. Zhao, C. He, *Nanoscale*, **2015**, *7*, 17079–17087.

[101] X. Yu, H. Cai, W. Zhang, X. Li, N. Pan, Y. Luo, X. Wang, J. G. Hou, *ACS Nano* **2011**, *5*, 952–958.

[102] S. Zeng, K. V. Sreekanth, J. Shang, T. Yu, C. K. Chen, F. Yin, D. Baillargeat, P. Coquet, H. P. Ho, A. V. Kabashin, K. T. Yong, *Adv. Mater.* **2015**, *27*, 6163–6169.

[103] J. Li, Y. Huang, Y. Ding, Z. Yang, S. Li, X. Zhou, F. Fan, W. Zhang, Z. Zhou, D. Wu, B. Ren, Z. Wang, Z. Tian, *Nature* **2010**, *464*, 392–395.

[104] Y. Tan, J. Gu, L. Xu, X. Zang, D. Liu, W. Zhang, Q. Liu, S. Zhu, H. Su, C. Feng, G. Fan. D. Zhang, *Adv. Funct. Mater*. **2012**, *22*, 1578–1585.

[105] W. Chen, J. Chen, Y.-B. Feng, L. Hong, Q.-Y. Chen, L.-F. Wu, X.-H. Lin, X.-H. Xia, *Analyst* **2012**, *137*, 1706–1712.

[106] P. Chokratanasombat, E. Nisaratanaporn, *Eng. J.* **2012**, *16*, 39–46.

[107] W.S. Seo, J.H. Shim, S.J. Oh, E.K. Lee, N.H. Hur, J.T. Park, *J. Am. Chem. Soc.* **2005**, *127*, 6188–6189.

[108] W.S. Seo, J.H. Shim, S.J. Oh, E.K. Lee, N.H. Hur and J.T. Park, *J. Am. Chem. Soc.*, **2005**, *127*, 6188–6189.

[109] A. Dong, X. Ye, J. Chen, Y. Kang, T. Gordon, J.M. Kikkawa, C.B. Murray, *J. Am. Chem. Soc.* **2011**, *133*, 998–1006.

[110] S. Brunauer, L. S. Deming, W. E. Deming, E. Teller, *J. Am. Chem. Soc.* **1940**, *62*, 1723–1732.

[111] P. I. Ravikovitch, D. Wei, W. T. Chueh, G. L. Haller, A. V. Neimark, *J. Phys. Chem. B* **1997**, *101*, 3671–3679

[112] P. Kubelka, *J. Opt. Soc. Am.* **1948**, *38*, 448–457.

[113] J. Bisquert, H. Randriamahazaka and G. Garcia-Belmonte, *Electrochim. Acta*, **2005**, *51*, 627.

[114] L.M. Da Silva, K.C. Fernandes, L.A. De Faria and J.F. Boodts, *Electrochim. Acta*, **2004**, *49*, 4893.

[115] a) G. Kresse, J. Hafner, *Phys. Rev. B* **1993**, *47*, 558; b) G. Kresse, J. Furthmüller, *Comput. Mater. Sci.* **1996**, *6*, 15; c) G. Kresse, J. Furthmüller, *Phys. Rev. B* **1996**, *54*, 11169.

[116] a) P. E. Blöchl, *Phys. Rev. B* **1994**, *50*, 17953; b) P. E. Blöchl, O. Jepsen, O. K. Andersen, *Phys. Rev. B* **1994**, *49*, 16223; c) G. Kresse, D. Joubert, *Phys. Rev. B* **1999**, *59*, 1758.

[117] J.P. Perdew, A. Zunger, *Phys. Rev. B* **1981**, *23*, 5048.

[118] J.P. Perdew, K. Burke, M. Ernzerhof, *Phys. Rev. Lett.* **1996**, *77*, 3865.

[119] N. Alidoust, M. Lessio, E.A. Carter, *J. Appl. Phys*. **2016**, *119*, 025102.

[120] S. L. Dudarev, G. A. Botton, S. Y. Savrasov, C. J. Humphreys, A. P. Sutton, *Phys. Rev. B* **1998**, *57*, 1505.

[121] G. Velegraki, J. Xie, Q. Zhang, G. S. Armatas, *ChemPlusChem* **2017**, *82*, 1290-1297.

[122] I. T. Papadas, I. Vamvasakis, I. Tamiolakis, G. S. Armatas, *Chem. Mater.* **2016**, *28*, 2886–2896.

[123] T. Shimanouchi, Tables of Molecular Vibrational Frequencies Consolidated Volume I, National Bureau of Standards, Washington, D.C., **1972**.

[124] S. Ikeda, K. Akamatsu, H. Nawafune, T. Nishino, S. Deki, *J. Phys. Chem. B* **2004**, *108*, 15599–15607.

[125] Y. Wang, D. C. Alsmeyer, R. L. McCreery, *Chem. Mater.* **1990**, *2*, 557–563

[126] A. C. Ferrari, J. C. Meyer, V. Scardaci, C. Casiraghi, M. Lazzeri, F. Mauri, S. Piscanec, D. Jiang, K. S. Novoselov, S. Roth, A. K. Geim, *Phys. Rev. Lett.* **2006**, *97*, 187401–187404.

[127] T. Wu, M. Chen, L. Zhang, X. Xu, Y. Liu, J. Yan, W. Wang, J. Gao, *J. Mater. Chem. A* **2013**, *1*, 7612–7621.

[128] L. G. Cançado, A. Jorio, E. H. Martins Ferreira, F. Stavale, C. A. Achete, R. B. Capaz, M. V. O. Moutinho, A. Lombardo, T. S. Kulmala, A. C. Ferrari, *Nano Lett.* **2011**, *11*, 3190–3196.

[129] L. M. Malard, M. A. Pimenta, G. Dresselhaus, M. S. Dresselhaus, *Phys. Rep.* **2009**, *473*, 51–87.

[130] R. Hawaldar, P. Merino, M. R. Correia, I. Bdikin, J. Grácio, J. Méndez, J. A. Martín-Gago, M. K. Singh, *Sci. Rep*. **2012**, *2*, 682.

[131] V. K. Abhinav V. K. Rao, P. S. Karthik, S. P. Singh, *RSC Adv.* **2015**, *5*, 63985–64030.

[132] X. Zhu, L. Shi, M. S. Schmidt, A. Boisen, O. Hansen, J. Zi, S. Xiao, N. A. Mortensen, *Nano Lett*. **2013**, *13*, 4690–4696.

[133] M. Alba, N. Pazos-Perez, B. Vaz, P. Formentin, M. Tebbe, M. A. Correa-Duarte, P. Granero, J. Ferre-Borrull, R. Alvarez, J. Pallares, A. Fery, A. R. de Lera, L. F. Marsal, R. A. Alvarez-Puebla, *Angew. Chem. Int. Ed*. **2013**, *52*, 6459–6463.

[134] Y. Zhao, Z. He, Z. Yan, *Analyst* **2013**, *138*, 559–568.

[135] P. Fakhri, B. Jaleh, M. Nasrollahzadeh, *J. Mol. Catal. A: Chem*. **2014**, *383*, 17–22.

[136] X. Zhang, C. Shi, E. Liu, J. Li, N. Zhao, C. He, *Nanoscale* **2015**, *7*, 17079–17087.

[137] S. Nie, S. R. Emory, *Science* **1997**, *275*, 1102–1106.

[138] K. Kim, H. S. Han, I. Choi, C. Lee, S. Hong, S. Suh, L. P. Lee, T. Kang, *Nat. Commun*. **2012**, *4*, 2182.

[139] Y. Wang, B. Yan, L. Chen, *Chem. Rev.* **2013**, *113*, 1391–1428.

[140] D. Lin, T. Qin, Y. Wang, X. Sun, L. Chen, *ACS Appl. Mater. Interfaces* **2014**, ***6***, 1320–1329.

[141] S. Zeng, K. V. Sreekanth, J. Shang, T. Yu, C.-K. Chen, F. Yin, D. Baillargeat, P. Coquet, H.-P. Ho, A. V. Kabashin, K.-T. Yong, *Adv. Mater*. **2015**, *27*, 6163–6169.

[142] L. Tian, S. Tadepalli, M. Fei, J. J. Morrissey, E. D. Kharasch, S. Singamaneni, *Chem. Mater*. **2015**, *27*, 5678–5270.

[143] J. Jana, M. Ganguly, T. Pal, *RSC Adv.* **2016**, *6*, 86174–86211.

[144] W.-H. Park, M. Jung, *J. Phys. Chem. C* **2016**, *120*, 24354–24359.

[145] J. L. Cuya, K. Sato, S. Kurita, T. Matsumoto, B. Jeyadevan, *J. Mater. Chem.* **2011**, *21*, 7062–7069.

[146] F.E. Osterloh, *Top Curr. Chem.*, **2016**, *371*, 105–142.

[147] P. Mohapatra, S.K. Samantaray, K. Parida, *J. Photochem. Photobiol. A: Chem*., **2005**, *170*, 189–194.

[148] A. Idris, N. Hassan, R. Rashid, A.-F. Ngomsik, *J. Hazard. Mater.*, **2011**, *186*, 629–635.

[149] A. Idris, N. Hassan, N.S.M. Ismail, E. Misran, N.M. Yusof, A.-F. Ngomsik, A. Bee, *Water Res.*, **2010**, *44*, 1683–1688.

[150] R.M. Cespón-Romero, M.C. Yebra-Biurrun, M.P. Bermejo-Barrera, *Anal. Chim. Acta*, **1996**, *327*, 37–45.

[151] A.D. Bokare, W. Choi, *Environ. Sci. Technol*., **2010**, *44*, 7232–7237.

[152] M. Kosmulski, *J. Colloid Inter. Sci*., **2014**, *426*, 209–212.

[153] G. Grancini, M. Maiuri, D. Fazzi, A. Petrozza, H.J. Egelhaaf, D. Brida, G. Cerullo, G. Lanzani, *Nat. Mater.*, **2013**, *12*, 29−33.

[154] S.D. Dimitrov, A.A. Bakulin, C.B. Nielsen, B.C. Schroeder, J.P. Du, H. Bronstein, I. McCulloch, R.H. Friend, J.R. Durrant, *J. Am. Chem. Soc*.**,** **2012**, *134*, 18189−18192.

[155] W.A. Tisdale, K.J. Williams, B.A. Timp, D.J. Norris, E.S. Aydil, X.Y. Zhu, *Science*, **2010**, *328*, 1543−1547.

[156] A. Tanaka, K. Nakanishi, R. Hamada, K. Hashimoto, H. Kominami, *ACS Catal.*, **2013**, *3*, 1886–1891.

[157] N. Nasrallah, M. Kebir, Z. Koudri, M. Trari, *J. Hazard. Mater.*, **2011**, *185*, 1398–1404.

[158] S. Omeiri, N. Allalou, R. Gharib, Y. Gabès, Y. Bessekhouad, M. Trari, *Theor. Exp. Chem.*, **2013**, *49*, 298–303.

[159] R. Gherbia, N. Nasrallaha, A. Amraneb, R. Maachia, M. Trari, *J. Hazard. Mater.*, **2011**, *186*, 1124–1130.

[160] C. Li, M.Z. Hoffman, *J. Phys. Chem. B*, **1999**, *103*, 6653–6656.

[161] L. Shen, W. Wu, R. Liang, R. Lin, L. Wu, *Nanoscale*, **2013**, *5*, 9374–9382.

[162] C. Mu, Y. Zhang, W. Cui, Y. Liang, Y. Zhu, *Appl. Catal. B: Environ.*, **2017**, *212*, 41–49.

[163] Y. Liang, S. Lin, L. Liu, J. Hu, W. Cui, *Appl. Catal. B: Environ.*, **2015**, *164*, 192–203.

[164] M. C. Biesinger, B. P. Payne, A. P. Grosvenor, L. W. M. Lau, A. R. Gerson, R. S. C. Smart, *Appl. Surf. Sci.*, **2011**, *257*, 2717–2730.

[165] Y. Nakabayashi, Y. Nosaka, *J. Phys. Chem. C*, **2013**, *117*,23832–23839.

[166] J. Wang, K. Ashley, D. Marlow, E. C. England, G. Carlton, *Anal. Chem.*, **1999**, *71*, 1027–1032.

[167] S. Kim, W. Choi, *Environ. Sci. Technol.*, **2002**, *36*, 2019–2025.

[168] A. Fujishima, X.T. Zhang, C. R. *Chimie*, **2006**, *9*, 750–760.

[169] K.Y. Jang, G. Park, K.H. Oh, J.H. Seo, K.M. Nam, *Chem. Commun.*, **2017**, *53*, 4120–4123.

[170] A.P. Salvador, C. Gutiérrez, *J. Phys. Chem.*, **1984**, *88*, 3696–3698.

[171] S. Wang, M. Chen, Y. Xie, Y. Fan, D. Wang, J. J. Jiang, Y. Li, H. Grutzmacher and C. Y. Su, *Small*, 2016, **12**, 2365.

[172] S. Zhao, Y. Wang, J. Dong, C.-T. He, H. Yin, P. An, K. Zhao, X. Zhang, C. Gao, L. Zhang, J. Lv, J. Wang, J. Zhang, A.M. Khattak, N.A. Khan, Z. Wei, J. Zhang, S. Liu, H. Zhao and Z. Tang, *Nat. Energy*, **2016**, *1*, 16184.

[173] G. Velegraki, J. Miao, C. Drivas, B. Liu, S. Kennou and G.S. Armatas, *Appl. Catal. B: Environ.*, **2018**, *221*, 635–644.

[174] Z.B. Alfassi, R.E. Huie, S. Marguet, E. Natarajan and P. Neta, *Int. J. Chem. Kinet.*, **1995**, *27*, 181–188.

[175] J. Colucci, V. Montalvo, R. Hernandez and C. Poullet, *Electrochim. Acta*, **1999**, *44*, 2507–2514.

[176] A.-M. Manke, K. Geisel, A. Fetzer and P. Kurz, *Phys. Chem. Chem. Phys.*, **2014**, *16*, 12029–12042.

[177] J. Bisquert, H. Randriamahazaka and G. Garcia-Belmonte, *Electrochim. Acta*, **2005**, *51*, 627–640.

[178] L.M. Da Silva, K.C. Fernandes, L.A. De Faria and J.F. Boodts, *Electrochim. Acta*, **2004**, *49*, 4893–4906.